QUILL

Quarterly Reports

February – April 2019

Contents

QUILL Quarterly Report

February – April 2019

Name:	**Marian Borucki**		
Supervisor(s):	Prof Peter Nockemann, Dr Stephen Glover and Dr Małgorzata Swadźba-Kwaśny		
Position:	PGR Student		
Start date:	01.2018	Anticipated end date:	
Funding body:	Bryden Centre, Horiba Mira		

Lithium ion batteries degradation study using spectroscopy techniques

Background

Lithium ion batteries (LIB) are secondary (rechargeable) batteries that are currently the main energy storage device. LIB are applied in various applications as in portable devices, grid energy storage, grid current regulation as well as in hybrid- and electric vehicles. Energy harvested by the renewable energies is often environmentally dependent, what results in discontinuous energy supply. In order to store energy that has been over generated during less energy consuming times of a day, energy storage stations based on LIB are used. The other, yet not less important, application is one where LIB are replacing the fossil fuel by storing the energy for transport sector, namely in hybrid (HEV) and electric vehicles (EV). The trend of replacing the fossil fuels both in energy sector by supplementing them with renewable energy power plants as well as by supporting the market of HEV, EV and fuel-cell vehicles (FCEV) is growing. New policies of EV30@30 and New Policy Scenario are the programmes that are aimed in expanding the market of HEV, EV and FCEV, thus the supply for lithium ion batteries will grow. Yet, for the market to growth the research, ones that solve current issues, are needed. Automotive Council UK in their roadmap report for the lithium ion batteries have gathered up the issues that need to be addressed if the automotive of EV, HEV and FCEV is to grow. Such issues are based on the need of improving the safety of battery usage, lowering the costs of the batteries, researching new materials for the batteries that will allow to store more energy and provide more power, thus be fast chargeable, issues concerning the battery pack and modules combination, one that will allow to minimalise the losses related to cell joining, as well as their thermal management, increasing the lifespan of the batteries as well as increase their recyclability, eventually the research on the next gen batteries is needed.

In order to meet all the requirements a full study of the current batteries as well as the development of a new chemistries is needed. Lifespan as well as the safety of the battery is nowadays one of the most important factors when it comes to the battery application in the transportation market. Battery life is limited by the degradation mechanisms, that occur inside the cell. Currently there are a known number of such mechanism occurring, even though the proper investigating technique allowing *in operando* study have not been developed yet. Moreover, the degradation is highly chemistry dependent so whenever the new chemistry is tested for the battery the new degradation mechanism could occur. On the other hand the safety of the battery is limited by the usage of the organic based electrolyte, which is highly flammable and might lead to battery explosion. Proper

electrolyte, non-toxic, environmental friendly, non-flammable as well as of high performance should be developed. With developing the new electrolyte, often the development of the electrodes is needed as the electrolyte stability as well as the energy density of the battery highly depends on them.

Objective of this work

The aim of the PhD programme is focused on investigating the lithium ion battery (LIB) degradation processes occurring inside the cell during its operation. In order to achieve the goal a development of an experimental method based on the spectroscopy analysis techniques will be needed. A proper method would allow to observe and measure the changes that occur *in operando* inside the lithium ion battery. During the PhD programme an analytical data of LIB degradation will be acquired, using various analytical techniques including electrode surface examination, electrolyte composition. Acquired spectroscopy data will be linked with the rest of the data gathered in order to develop the sensing method. Eventually, batteries of different cell chemistries will be investigated.

Progress to date

Firstly, I would like to summarise previous report progress description, as the following progress to date will be referring to what was done before this report. Also, I have found it important in order to maintain the continuously of the research progression.

The subject of study has not changed since the previous report. Lithium ion cells made out of graphite anode, $LiNi_{8/10}Mn_{1/10}Co_{1/10}O_2$ (NMC811) as a cathode material, which are coated on the thin foil of copper and alumina current collators, respectively. The electrolyte used is $LiPF_6$ in ethylene carbonate (EC): ethylene methylene carbonate (EMC) as 1:1 molar ratio solution. Additionally, polyolefin separators are used as a physical barrier between two electrodes. The assembly of Li-ion cells are undertaken in glovebox, with inert atmosphere (Ar based) and low concentration of water and oxygen (less than 0.1 ppm) due to the use of an organic electrolyte. The lithium-ion cell scheme both as a technical inscription and graphitic representation can be observed in Figure 1.

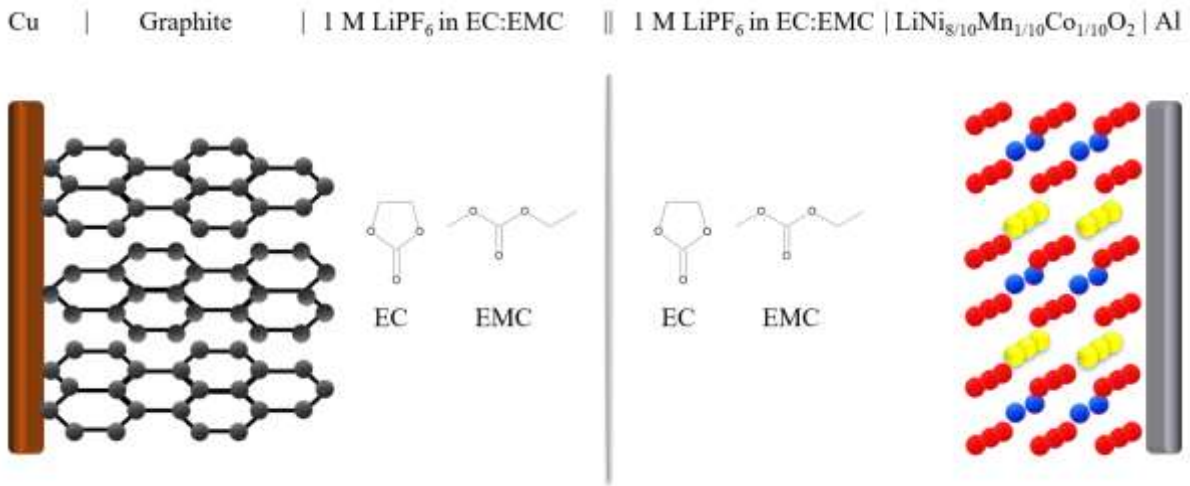

Figure 1- Lithium-ion cell inscription and scheme.

In the above figure, individual parts of the studied cell could be distinguished, from the left to the right: a copper current collector, graphite anode, electrolyte separated by the polyolefin film, NMC811 as cathode material and alumina current collector. All of these cell components are arranged in the same pattern inside the studied samples.

Further of assembling lithium-ion cells, their quality control and testing is implemented. There can be four procedures distinguished, each with different purpose. These procedures are:

a) Three charge-discharge cycles at theoretical 0.1 C current rate
b) Four series of three cycles with varying current rates
c) Single discharge with varying current
d) Dynamic stress testing cycles

In order to carry out the experiments a theoretical calculation was made according to the equations:

$$C_t = \frac{zF}{M}\ [mAh\ g^{-1}] \quad (1)$$

Where C_t is a theoretical specific columbic capacitance, z is the number of electrons transferred during the reaction, F being the Faraday's constant and M the molar mass of the structure from which or to which the charge is detached/attached, respectively. The theoretical specific coulombic capacitances of materials used have been calculated and summarised in Table 1.

Table 1 - Theoretical specific columbic capacities of used active materials.

Material	Molecular weight [g mol^{-1}]	Theoretical specific capacity [mAh g-1]
NMC 811	97.27	275.50
Graphite	72.06	372.24

Taking into consideration the mass of the substances that have been used in a single sample, as well as the specific coulombic capacities of materials, a theoretical coulombic capacities for lithium ion cells has been calculated. Having, at least a theoretical knowledge about the properties that the sample should exhibit, a previously mentioned quality control and testing procedure was implemented. The first procedure a) of three charge-discharge cycles is ought to activate the studies sample by using low charging and discharging currents. After the sample is activated and basic information about actual performance of the sample is gathered, further testing is implemented, yet using the actual properties not the theoretical ones. The second b) procedure is to check how the sample is reacting to changing current rates, thus if sample is stable enough. This procedure, as the further ones are conducted according to industrial partner knowledge and requirement, based on USABC battery testing criteria. If the sample capacity changes during the second procedure and is not varying more than 2%, the sample is considered to be stable and the third procedure of single discharge with varying current, namely peak power test is implemented. The purpose of this procedure is to use the obtained data from single battery discharge during which a current is changes drastically, to a calculation of peak power of battery system. The peak power is needed as the dynamic stress testing, the fourth procedure, is completely dependent on varying power during the battery cycling. The last procedure is made up of cycles, during which battery is stressed with varying power of charge and discharge, which represents the actual usage of the battery.

The electrochemical characterisation of commercial electrolytes has been undertaken in order to obtain information about its stability in both anodic and cathodic potential ranges. The cyclic voltammetry (CV) experiments in two half cells was prepared. Working electrode (WE) in anodic half-cell was made out of graphite coated on a copper foil set against Lithium electrode, which served as a counter (CE) and reference (RE) electrode. The studied potential range of anodic half-

cell was between 0 – 3 V, and the scan rate used was 0.5 mV s^{-1}, which is considered to be low one, yet in order to observe proper (de)intercalation, such slow scan rates are needed. On the other hand, the cathodic half-cell was combined out of the NMC811 cathode coated on an aluminium foil as a WE, and pure Lithium as a CE and RE both. The potential range of the cathodic half-cell was in the range of 2.0 – 4.8 V. Also, in order to observe the lithium (de)intercalation as well as its plating the scan rates of 0.1 mV s^{-1} was implemented. Cyclic voltammograms obtained from the both half-cells are presented in Figure 2. On an anodic voltammogram, A) of Figure 2, one could observe an anodic peak at range of $0\ \mathrm{V} - 0.2\ \mathrm{V}$, which is attributed to the lithium ion stripping from the pure lithium electrode and their further intercalation into and graphite structure. On the cathodic sweep, there are two peaks visible, the bigger one at $0.5\ \mathrm{V}$ is attributed to the reverse process of lithium ion deintercalation and further their plating on the pure lithium electrode. The smaller peak at about $1.4\ \mathrm{V}$ is originated from possible electrode or electrolyte impurities. Generally stripping/platting or intercalation peaks are much less visible than redox peaks on cyclic voltammograms, meaning that the observed redox peak from impurities is even less profound, thus the impurities itself are marginal, at least for the scope of this research.

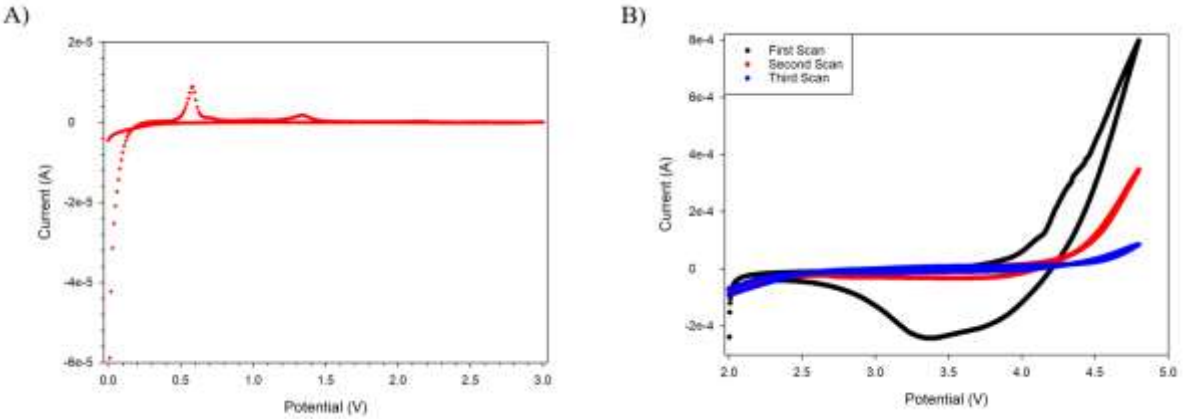

Figure 2- Cyclic voltammograms (CV) of a half-cells undertaken at A) anodic potential range of 0.1 – 3.0 V and B) cathodic potential range of 2.0 – 3.8 V with a scan rate of 0.5 mV s^{-1} and 0.1 mV s^{-1}, respectively. Pure lithium served both as CE and RE.

On the cathodic half-cell cyclic voltammograms, B) park of Figure 2, one could observe an order of magnitude grater response for redox reactions ongoing in the system. Especially interesting is the first scan (black), where oxidation reactions started to take place already at potentials as low as $2.5\ \mathrm{V}$ and continued up to the final set potential of $4.8\ \mathrm{V}$. The high response of the half-cell, especially during the first scan indicates that the irreversible reactions have taken place, as the second and third scan are much more horizontal in appearance. The irreversible reaction of oxidation can be attributed to the formation of a protective layer on the aluminium current collector used as a current collector in the positive half-cell of a battery.

After obtaining the data regarding electrolyte performance in both of the half-cells a solid electrolyte interphase (SEI) formation was observed and the properties as well as its effects on the battery performance have been studied. The first study has taken into account an electrochemical stability of the full cell, yet comparing the activated and non-activated sample. In order to activate the sample a first testing procedure was implemented, as it was described in the previous section. The inactivated sample was simply the freshly assembled lithium ion cell. In order to study their stability a linear sweep voltammetry (LSV) study up to high potential was performed. The results of such study can be seen in Figure 3.

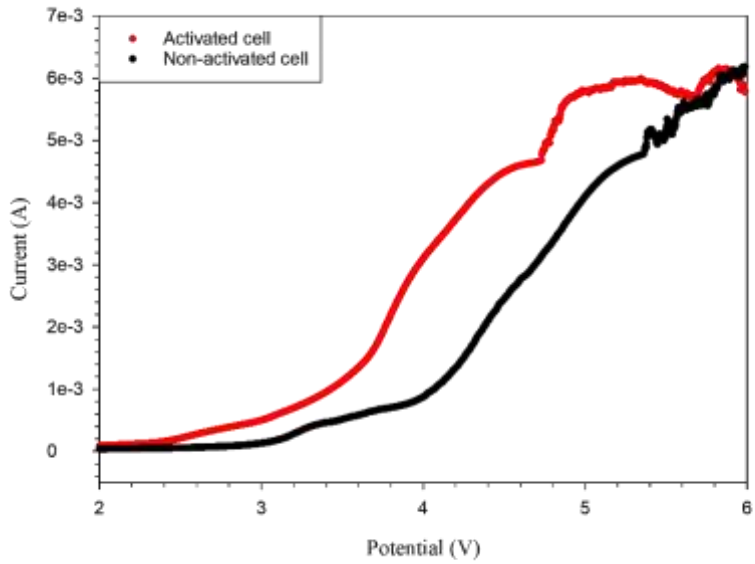

Figure 3 - Linear sweep voltammetry (LSV) at 0 – 6 V potential range and scan rate of 1 mV s^{-1} performed on the CR2032 coin cell sample in inactivated (black) and activated (red) state.

From the Figure 3 it can be easily distinguished that the potential to current response for the both samples is different, though the only thing that has changed was the activation itself so three charge-discharge cycles at low current rates. The activated sample response seems to be shifted with higher current response at lower potentials, thus indicating that the activated sample is less stable at the same currents. Such results clearly suggest that something in the cell properties have changed. Knowing that the current response to the potential is depending upon the system resistance, the electrochemical impedance spectroscopy (EIS) studies are ongoing in order to observe the change that have occurred inside the system.

Conclusions and future work

Ageing tests of the manufactured batteries will be undertaken for the duration of up to 11 months in order of determining the degradation mechanism occurring. During the ageing study part of the cycled batteries will be disassembled depending on the charge-discharge cycles number. *Ex situ* microscopic, crystallographic as well as spectroscopic studies will be performed in favour of obtaining the information about the severity of each degradation mechanisms. Both degradation mechanisms of losses in lithium inventory (LLI) as well as losses in active material (LAM) will be investigated. Meanwhile the methodology of *in situ* spectroscopic study of the cell will be developed. Data gathered through *ex situ* studies will be used to determine the level of degradation for the lithium ion cells monitored through *in situ in operando* technique.

Moreover, the electrochemical systems of different electrolytes and electrodes setups will be assembled and further studied according to the previous mentioned methodology. The planed studied setup includes carbon, silica and carbon-silica based anodes as well as the pure and semi-solid ionic liquid electrolytes. The studies of their stability as well as overall performance will be undertaken.

QUILL Quarterly Report

February – April 2019

Name:	**Robert Boyd**		
Supervisor(s):	Prof Peter Nockemann and Prof Martin Atkins		
Position:	PhD Student		
Start date:	October 2016	Anticipated end date:	October 2019
Funding body:	DEL		

Non-Aqueous Electrolytes for Flow Batteries

Background

Cheap, safe and efficient energy storage is essential in developing practical and sustainable energy strategies necessary for maintaining a balanced, efficient and reliable electric grid system based on both conventional electricity generation industries and the integration of intermittent renewable energy sources.

Batteries for large-scale grid storage must satisfy a different set of variables compared to many conventional rechargeable batteries. Such batteries must be; durable, maintain efficiency over a large number of charge/discharge cycles, have high round-trip efficiency, able to respond instantly to changes in load or input, and have reasonable capital costs[1]. Redox flow batteries are able to meet much of this criterion hence there has been significant interest in the optimisation of redox flow batteries for large-scale energy storage over the last few decades.

The all vanadium RFB was and remains the 'flagship' for redox flow batteries. It has a higher energy efficiency, longer operational lifetime and lower cost compared with other redox batteries (zinc bromide, sodium sulfur and lead acid)[2]. It remains the only RFB to have been sold in significant numbers due in part to being the only RFB to make use of the same metal species in both half-cells, avoiding cross-contamination issues.

Flow batteries incorporating organic molecules as the charge carriers are experiencing significant interest for large scale energy storage. Engineering the structure of organic molecules can deliver low cost redox active molecules with favourable potentials, increased solubility and greater stability. Both quinones and N-heterocycles are currently experiencing extensive investigation for application in flow batteries.

Objective of this work

Improve upon the commercial all-vanadium flow battery by reducing costs, increasing energy density and increasing cell voltage.

Progress to date

Ionic Liquid Solvent

Manganese (II) acetylacetonate was dissolved in 1-butyl-1-methylpyrrolidinium ($[C_4C_1pyr][NTf_2]$), 1-butyl-3-methylimidazolium ($[C_4mim][NTf_2]$) and 1-butyl-1-methylazepanium bis(trifluoromethylsulfonyl)imide ($[C_4C_1azp][NTf_2]$) to form a redox active electrolyte.

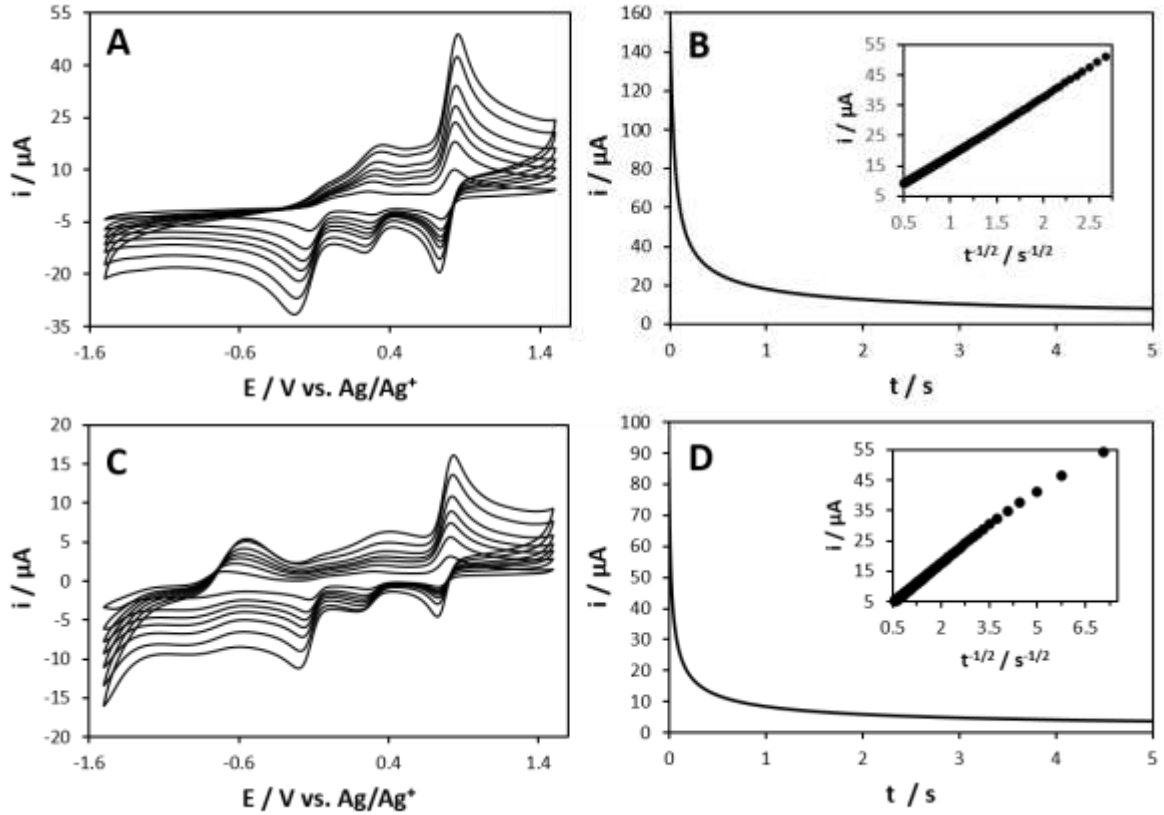

Figure 1 - (A) CVs recorded at a 5 mm diameter GC electrode in 0.01 M $Mn(acac)_3$ in $[C_4C_1pyr][NTf_2]$ at (from top to bottom) 0.2 V s^{-1}, 0.15 V s^{-1}, 0.1 V s^{-1}, 0.07 V s^{-1}, 0.05 V s^{-1}, 0.03 V s^{-1} and 0.01 V s^{-1}. (B) Chronoamperogram recorded using a 5 mm diameter GC electrode in 0.01 M $Mn(acac)_3$ in $[C_4C_1pyr][NTf_2]$. The potential was stepped from 0.5 V to 1.1 V and held for 1 s. The inset shows the plot of I vs. $t^{-1/2}$. (C) CVs recorded at a 3 mm diameter Pt electrode in 0.01 M $Mn(acac)_3$ in $[C_4C_1pyr][NTf_2]$ at (from top to bottom) 0.2 V s^{-1}, 0.15 V s^{-1}, 0.1 V s^{-1}, 0.07 V s^{-1}, 0.05 V s^{-1}, 0.03 V s^{-1} and 0.01 V s^{-1}. (D) Chronoamperogram recorded using recorded at a 3 mm diameter Pt electrode in 0.01 M $Mn(acac)_3$ in $[C_4C_1pyr][NTf_2]$. The potential was stepped from 0.6 V to 1 V and held for 1 s.

Electrolyte	Potential (V)		Cell Potential (V)
	Mn^{2+}/Mn^{3+}	Mn^{3+}/Mn^{4+}	
$[C_4C_1pyr][NTf_2]$	0.04	0.79	0.75
$[C_4C_1im][NTf_2]$	0.27	1.32	1.05
$[C_4C_1azp][NTf_2]$	0.06	0.80	0.74

Table 1 - Redox potentials associated with $Mn(acac)_3$ dissolved in ionic liquid

Cyclic voltammetry data displays two redox peaks attributed to Mn^{2+}/Mn^{3+} (0.04 V) and Mn^{3+}/Mn^{4+} (0.79 V) on using $[C_1C_4pyr][NTf_2]$ as the solvent, producing a theoretical cell voltage of 0.75 V. The imidazolium ionic liquid delivered a larger theoretical voltage, 1.05 V, however the stability of imidazolium based ionic liquids remains a concern due to the reactivity associated with the unsaturated ring.

Organic Redox Active Compounds

Anthraquinone

Anthraquinone undergoes two reversible, single electron reductions resulting in the formation of radical anion,[3] stabilised by its resonance forms, and di-anion. Solubility of these compounds remains challenging due to the long-range order from significant intermolecular interaction between quinones.

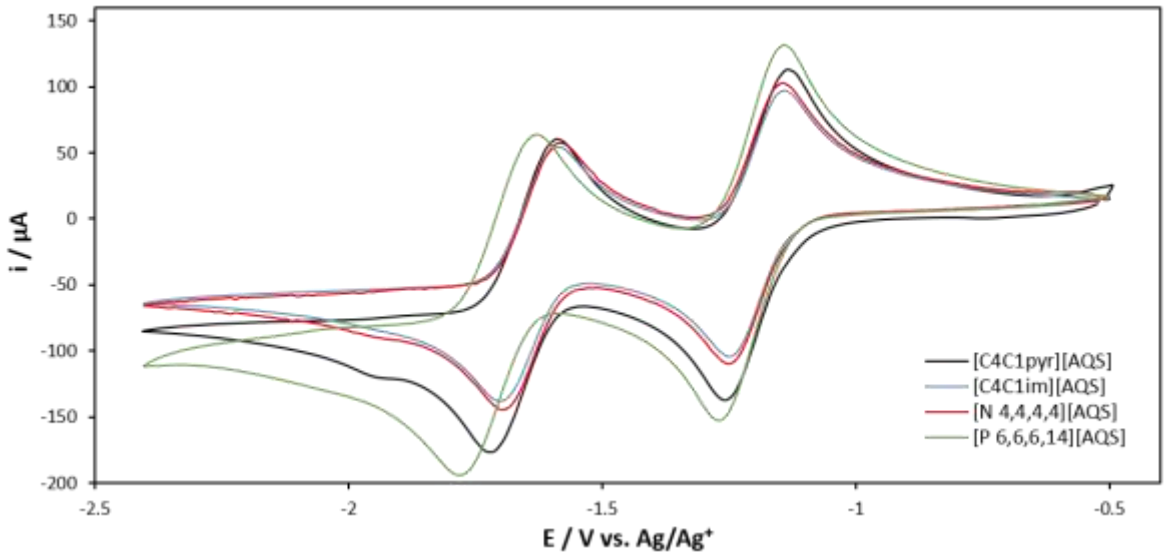

Figure 2 - CVs of multiple ionic compounds featuring the anthraquinonesulfonate anion.

Changing the cation resulted in little change to the position of the oxidation and reduction peaks meaning the cation can be modified to accommodate other electrolyte properties such as high solubility without compromising on cell voltage.

The phosphonium derivative was further studied via TGA analysis to probe thermal stability, shown in Figure 3.

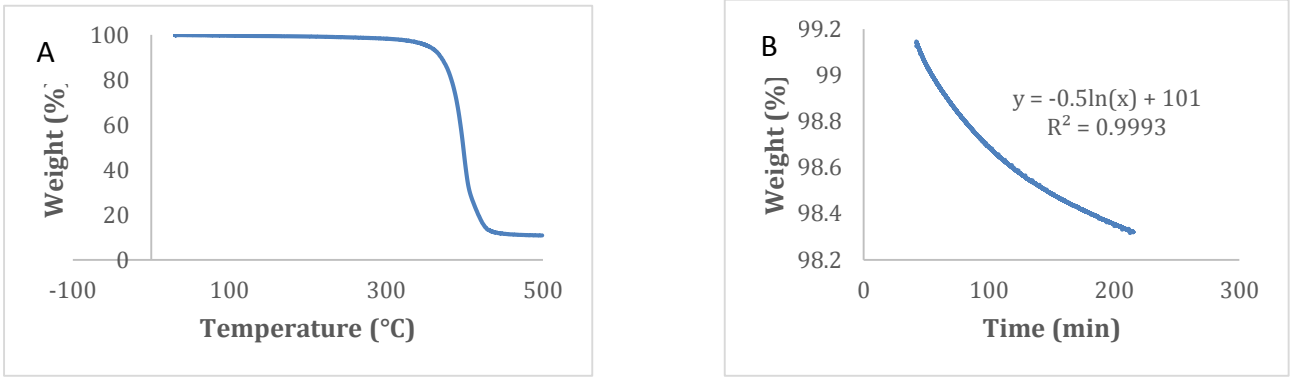

Figure 3 - (A) TGA analysis of [P_{66614}][AQS], heated at 10 °C/min, and (B), isotherm of [P_{66614}][AQS], holding the sample at 200 °C.

[P_{66614}][AQS] displayed excellent thermal stability, showing little to no signs of degradation up to 250 °C. Holding the sample at 200 °C enabled 10 % thermal degradation to be calculated to occur after 5000 years, more than sufficient for the lifetime of a flow battery.

Anthraquinone was incorporated into the cation to investigate the effect on electrochemistry and solubility. An ammonium cation featuring large alkyl groups was used as the cation and formed a yellow solid when the anthraquinone structure was linked to the nitrogen.

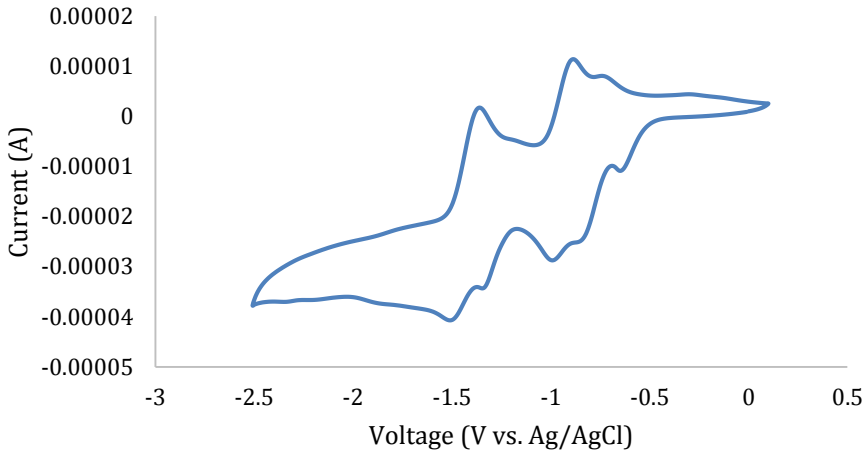

Figure 4 - CV of [$N_{10101AQN}$][NTf_2] in acetonitrile with supporting electrolyte.

As with the previous anthraquinone anions, the CV shows four peaks derived from two consecutive single electron transfer steps during oxidation and reduction.

Adding the energy storage unit to the cation enables the synthesis of an organic molecule capable of storing four electrons per molecule, simply by exchanging the anion with anthraquinone sulfonate shown previously. A complete cell using this molecule may be able to benefit from its large, bulky sterics by using a cheaper cellulose dialysis membrane instead of expensive fluorinated membranes such as Nafion.

Hydroquinone

The redox potential off hydroquinone occupies the positive side of the electropotential scale making it an ideal candidate to form a complete cell with anthraquinone.

Hydroquinonesulfonic acid was incorporated into several ionic liquids and investigated as a potential redox active molecule for use in the positive half-cell.

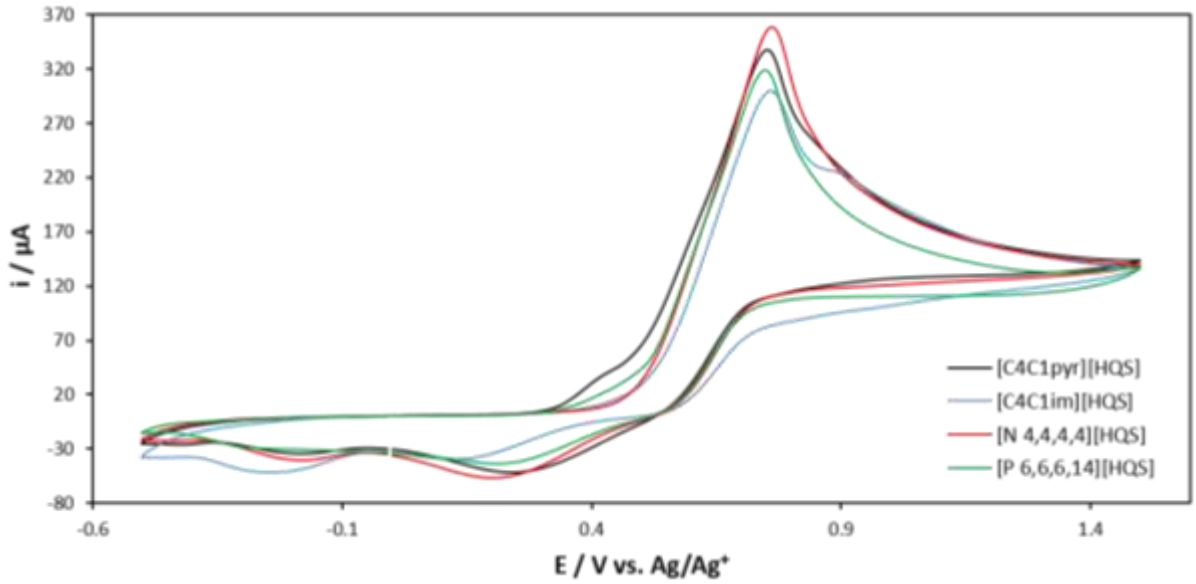

Figure 5 - CVs of 4 hydroquinonesulfonic acid compounds (0.01 M) in acetonitrile with TEATFB (0.1 M) supporting electrolyte.

A large oxidation peak was observed and a shallow reduction peak indicating an electrochemically irreversible reaction which may be due to the reduced electron delocalisation around one unsaturated ring compared to the three rings of anthraquinone.

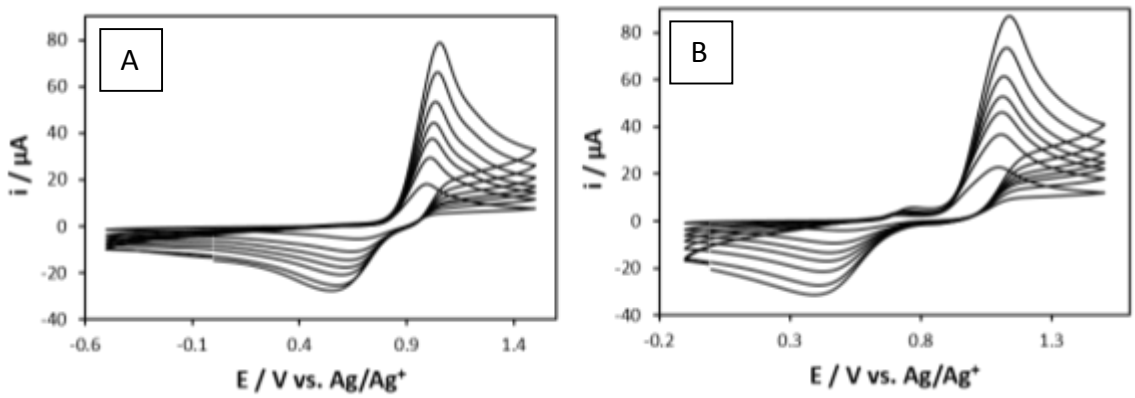

Figure 6 - [C_4C_1pyr][HQS] (0.01 M) dissolved in [C_4C_1pyr][NTf_2], A, glassy carbon electrode (3 mm) and, B, platinum electrode (3 mm).

[C_4C_1pyr][HQS] was dissolved in [C_4C_1pyr][NTf_2] displaying a smoother spectra with a slightly increased reversibility. This may be due to the less reactive ionic liquid stabilising the hydroquinone as it is oxidised and reduced.

Conclusions and future work

Manganese acetylacetonate in [C_1C_4pyr][NTf_2] formed an electrolyte with a theoretical cell voltage of 0.75 V. Despite showing a smaller voltage than the all vanadium flow battery, manganese is significantly cheaper than vanadium and the electrolyte would be stable over a wider temperature range compared to an aqueous electrolyte, desirable for operation in hot and cold climates.

However, the cost of ionic liquid is substantially higher than using water and so research to find a cheaper alternative. Other metal salts also need to be investigated in order to extend the cell voltage to at least 1.4 V matching that of the vanadium flow battery.

Organic molecules incorporating quinones have displayed excellent reversibility and solubility in organic solvent. Their tunability enables them to be modified for the specific system they are to be implemented in producing higher cell voltage and increased energy density. To determine the value of these compounds they must be studied in a complete cell to measure their ability to be charged and discharged over numerous cycles without degradation and self-discharge.

A membrane-free flow battery may be possible using the immiscible $[C_2mim][NTf_2]$ and $[P_{66614}][NTf_2]$. Dissolving quinones with the same cation into these ionic liquid solvents may keep both redox active molecules from mixing without needing a membrane. This would contribute to lower resistance and reduce the cost.

References

1. A. Z. Weber, M. M. Mench, J. P. Meyers, P. N. Ross, J. T. Gostick and Q. Liu, *J. Appl. Electrochem.*, 2011, **41**, 1137–1164.
2. K.-L. Huang, X. Li, S. Liu, N. Tan and L. Chen, *Renew. Energy*, 2008, **33**, 186–192.
3. P. S. Guin, S. Das and P. C. Mandal, *Int. J. Electrochem.*, 2011, **2011**, 1–22.

QUILL Quarterly Report

January - May 2019

Name:	**Emily Byrne**		
Supervisor(s):	Dr Małgorzata Swadźba-Kwaśny and Prof John Holbrey		
Position:	PhD student		
Start date:	October 2017	Anticipated end date:	October 2020
Funding body:	DfE (Department for the Economy)		

Physical characterisation of functional liquids

Background

It is proposed that deep eutectic solvents 'DES' are a chemical component mixture composed of hydrogen bond donors and acceptors which have intermolecular interactions that result in a freezing point which is lower than that of the isolated individual components of the system with no interactions between each other.[1] They are asymmetric species which, due to their orbitals' inability to overlap well and thus, pack into a regular lattice arrangement, have low lattice energy and so do not require a large amount of energy in order to exist as a liquid and as a result tend to have low melting points.

The most common and well renowned DES are those prepared with the combination of organic salts such as choline chloride, which act as a hydrogen bond acceptor and carboxylic acids or alcohols with a hydrogen bond donating role.[2–5] However, these solvents are generally miscible with water and so their application is quite limited. Therefore, work was undertaken by van Osch *et al.* which led to the publication of the first hydrophobic deep eutectic solvent using a carboxylic acid hydrogen bond donor and a long chain quaternary ammonium salt in 2015.[6] In addition to this, DES have since been formed using alcohols and fatty acid hydrogen bond donors in combination with organic salts to form deep eutectic solvents which can be used for extraction of metals[7] and natural products[8,9]. In addition to this, in an attempt to reduce the viscosity associated with these charged DES species, Ribeiro *et al.* developed DES systems using D-menthol and carboxylic acid hydrogen bond donors where the individual components used are non-ionic species.[10] More recently, DES made with the combination of trioctylphosphine oxide (TOPO) and phenol have been published and its use as a uranyl extractant shown.[11]

TOPO has a number of uses such as capping agents[12–16] in nanoparticle synthesis, metals[17,18], organic acids[19–22] and phenolics[23–26] extraction and so a number of DES will be prepared using a range of hydrogen bond donors most suited to the potential application.

Objective of this work

In this work, leaching studies for a TOPO:malonic acid extracting phase have been carried out and levulinic acid has been combined with TOPO to form a deep eutectic solvent. TOPO:levulinic acid have been combined across the whole compositional range in increments of 0.1 from χ_{TOPO} = 0.1-1.0 and mixtures at χ_{TOPO} = 0.33 and 0.67 have also been included. The physical properties of the mixtures have been characterised and they will be applied to an industrial application.

Progress to date

Following on from previous reports where I showed a TOPO:Malonic acid eutectic in a 2:1 ratio was used to extract gallium from an acidic chloride source with a $LogD_{Ga}$ approximately 3 times greater than that of the literature benchmark[17] when conditions were replicated. Physical characterisation of the eutectic extractant was also previously carried out. Therefore, interesting results lead to leaching studies being carried out to determine whether or not malonic acid leached out of the organic phase into the aqueous phase during precontact and extraction as shown in this work. Physical characterisation of TOPO:levulinic acid mixtures will also be shown; interesting due to the potential for extraction of TOPO:levulinic acid from fermentation broths via the formation of an in situ TOPO:levulinic acid deep eutectic solvent.

To begin this section of work, Leaching studies were performed due to concern about the leaching of malonic acid out of the extractant phase and into the aqueous phase upon pre-contact and extraction and thus the suitability of the TOPO:malonic acid as an extractant. These studies were performed using 2 different χ_{TOPO} liquids at either equivolume (1:1) or 1:5 organic:aqueous volume ratio in both 0 M and 6 M HCl. The resulting aqueous phase was analysed with infra-red and total organic carbon content analysis and the results for 0 M and 6 M HCl aqueous phases shown in Table 1 and Table 2 respectively below.

Mole ratio TOPO	Org:Aq	[Malonic acid] / gL^{-1}	
		ATR-IR	TOC
0.67	1:1	15	14
0.67	1:5	28	31
0.55	1:1	59	56
0.55	1:5	86	73

Table 1 - [Malonic acid] in the aqueous phase after shaking TOPO:malonic acid liquid with an aqueous phase. Shaking time 20 mins, 0 M HCl

Mole ratio TOPO	Org:Aq	[Malonic acid] / gL^{-1} (TOC)
0.67	1:1	50
0.67	1:5	66
0.55	1:1	92
0.55	1:5	110

Table 2 - [Malonic acid] in the aqueous phase after shaking TOPO:malonic acid liquid with an aqueous phase. Shaking time 20 mins, 6 M HCl

These results show that numerous factors affect the extent of malonic acid leaching occurring. In both 0 M and 6 M HCl, the mole ratio of the TOPO liquid plays a large part in the extent of malonic acid leaching from the extractant phase as moving from χ_{TOPO} = 0.67 to χ_{TOPO} = 0.55 increases the [malonic acid] in the aqueous phase by 42 gL^{-1}. The organic:aqueous volume ratio also plays a role in the extent of leaching occurring as in all cases, changing the organic:aqueous volume ratio from 1:1 to 1:5 increases the aqueous [malonic acid] by 17-18 gL^{-1} when all other factors are kept constant. Finally, a greater extent of malonic acid leaching occurs when switching from a 0 M to a 6 M HCl aqueous phase, with a 35-37 gL^{-1} increase in aqueous malonic acid content.

Under typical extraction conditions where a χ_{TOPO} = 0.67 TOPO:malonic acid eutectic is used over a range of HCl concentrations in an equivolume organic:aqueous ratio, malonic acid leaching would likely be between 14-50 gL^{-1}. This is a relatively low extent of leaching occurring given that the solubility of malonic acid in water is 763 gL^{-1}. This indicates that the majority of malonic acid has the tendency to be held within the eutectic layer during extraction. With investigation into the time taken for extraction to be completed and the potential for the shaking time related to pre-contact and extraction reduced, it is hoped that this leaching could be further reduced.

Physical characterisation of TOPO:levulinic acid samples were then performed with samples made across the whole compositional range χ_{TOPO} = 0.1-1.0 including χ_{TOPO} = 0.33 and 0.67. Thermal decomposition of the samples was first of interest and so TGA pans were prepared for each of the samples to ensure that DSC samples were not run above their thermal limits.

Each χ_{TOPO} sample was then prepared for DSC and solid liquid cell (SLC) apparatus to understand the phase behaviour of the samples at varying χ_{TOPO} values and the temperature recorded for a thermal event. The results were reported as the end-point of the melt on the DSC. The results are shown in Figure 1 below.

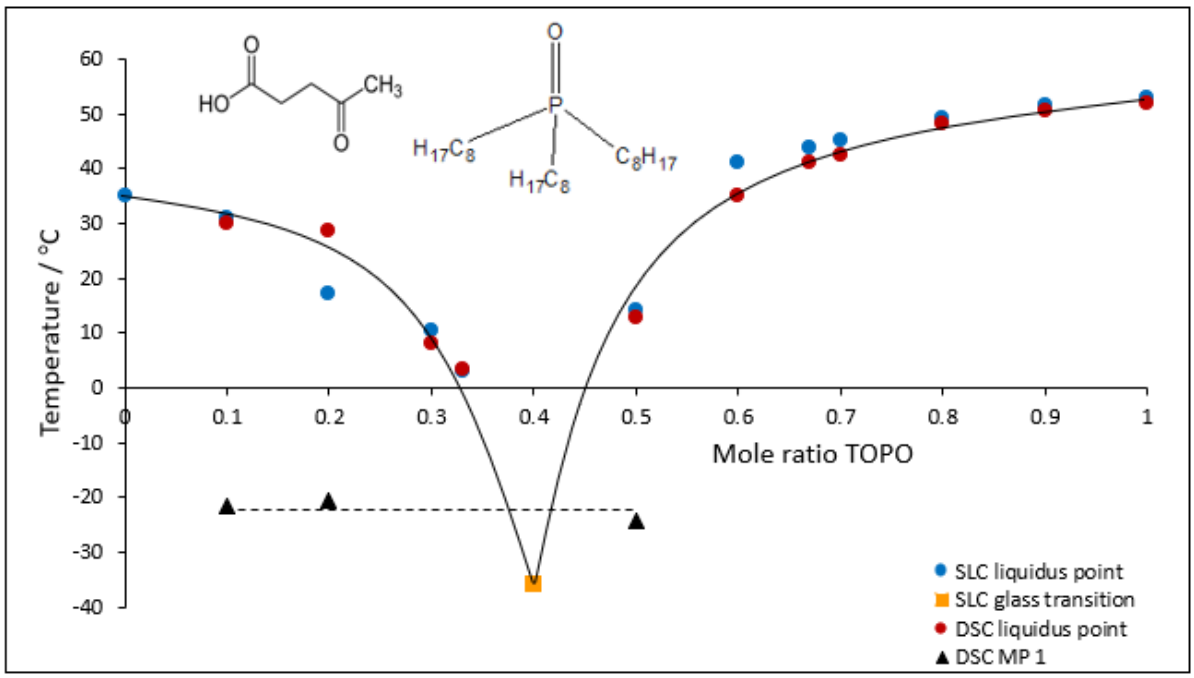

Figure 1 - Phase behaviour of TOPO:levulinic acid mixtures at varying χ_{TOPO} values as a function of temperature and χ_{TOPO}

Figure 1 above highlights two regions of interest, that of onset melting corresponding to the formation of the eutectic component of the mixtures as shown by the horizontal line in the diagram at χ_{TOPO} = 0.1, 0.2 and 0.5 and the liquidus point of the sample at each χ_{TOPO} value.

Tracing the liquidus point line shows that with increasing χ_{TOPO} values from 0.0 (i.e. pure levulinic acid), there is a depression melting point from +35 °C to -36 °C at its minimum at χ_{TOPO} = 0.4. This point at χ_{TOPO} = 0.4, however, appears to exhibit supercooling as it is below the horizonal line produced by the other samples which corresponds to a eutectic component in these mixtures and is a glassy species at χ_{TOPO} = 0.4 and so only the onset of stirrer bar movement could be recorded. With further increase in χ_{TOPO}, there is an increase in liquidus point of the samples until χ_{TOPO} = 1.0 (i.e. pure TOPO).

The lowest melting point within this phase diagram is χ_{TOPO} = 0.4 and not χ_{TOPO} = 0.33 as co-crystal formation would suggest due to the formation of 2 hydrogen bonding interactions between phosphorus and the hydrogen bond donor.[70] This suggests that there is a dynamic switching in TOPO co-ordination in the liquid phase between χ_{TOPO} = 0.33 and χ_{TOPO} = 0.5 where the number of hydrogen bonds associated with each phosphorus entity changes between 2 and 1 respectively. This increase the extent of disruption when considering the packing of species into a lattice and further destabilises the system; allowing a greater ease of liquid formation at χ_{TOPO} = 0.4.

NMR studies were then performed on the 4 liquid samples χ_{TOPO} = 0.3-0.5 in order to track how addition of levulinic acid effects the acidity of the phosphorus environment on TOPO. The results of this is shown in Figure 2 below.

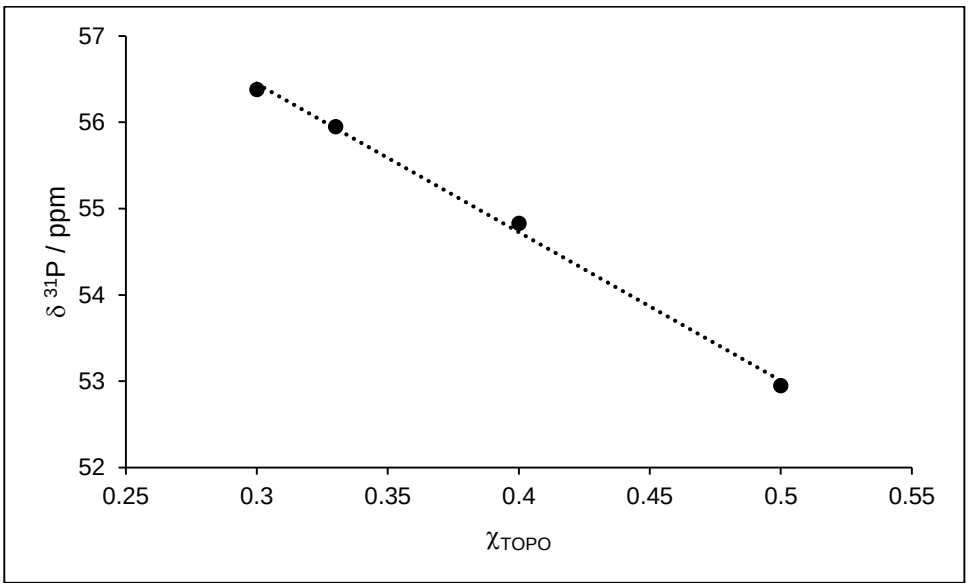

Figure 2 - ^{31}P NMR comparison between TOPO:levulinic acid mixtures

The δ^{31}P shifts of the TOPO component of the mixtures are as follows: χ_{TOPO} = 0.30 (δ ^{31}P = 56.38 ppm), χ_{TOPO} = 0.33 (δ ^{31}P = 55.95 ppm), χ_{TOPO} = 0.40 (δ ^{31}P = 54.83 ppm) and χ_{TOPO} = 0.50 (δ ^{31}P = 52.95 ppm) as shown in Table 3.

χ_{TOPO}	δ ^{31}P / ppm
0.5	52.95
0.4	54.83
0.33	55.95
0.3	56.38

Table 3 - δ ^{31}P Shifts associated with χ_{TOPO} mixtures

With a decreasing TOPO component in the mixture, ^{31}P signals shift downfield as the proportion of malonic acid present increases. This suggests, that the acidity surrounding the phosphorus environment of the TOPO molecule is increasing as the concentration of malonic acid increases. Similar to work conducted by Gilmore et al.[11] studying a TOPO:phenol system, the $\Delta\delta$ ^{31}P remains constant at approximately constant with $\Delta\delta$ = 1.55 - 2 ppm between each subsequent χ_{TOPO} = 0.1 increment in χ_{TOPO} mixture with a linear trend, suggesting that it is the levulinic acid concentration is directly affecting the acidity surrounding the phosphorus environment.

Finally, density was also measured for each of the liquid samples formed and the results shown in Figure3 below.

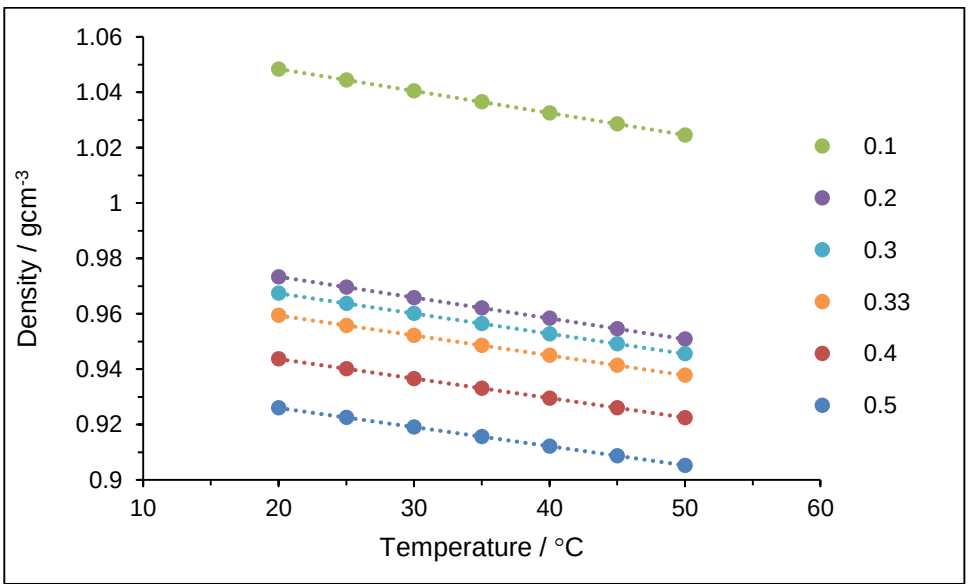

Figure 3 - Comparison of density with changing χ_{TOPO} as a function of temperature

Results from this study show that density decreases with an increasing χ_{TOPO} mole ratio as expected due to TOPO being less dense than malonic acid (0.861 gcm^{-3} and 1.14 gcm^{-3} respectively) and also that density of each liquid sample decreases with increasing temperature as expected.

Conclusions and future work

To conclude, leaching studies have highlighted that under typical extraction conditions, approximately 14-50 gL^{-1} of malonic acid will leach out of the eutectic extractant phase and into the aqueous phase during pre-contact and extraction (0 M and 6 M HCl aqueous phases respectively)

and that under optimal HCl concentrations to extract gallium from aqueous chloride sources (i.e. 6 M HCl), 50 gL^{-1} malonic acid will be lost from the extractant phase. This is, however, promising as malonic leaching to the aqueous phase occurs to a much lesser extent than initially anticipated as the solubility of malonic acid in water is 763 gL^{-1}. This leads to the extent of leaching occurring 713 gL^{-1} lower than if pure malonic acid came into contact with water, indicating that malonic acid is preferentially held within the eutectic extracting phase.

TOPO:levulinic acid mixtures were prepared across the whole compositional range from χ_{TOPO} = 0.1-1.0 with thermal gravimetric analysis to determine thermal stability performed and a phase diagram produced using both differential scanning calorimetry and solid liquid cell observational analysis. Thermal stability increased with increasing mole ratio of TOPO in the mixtures. The phase diagrams show that the eutectic point occurs at χ_{TOPO} = 0.4 for TOPO:levulinic acid mixtures and thus indicates that there is a competitive equilibrium between TOPO's phosphorus bound to 1 hydrogen bond and 2 hydrogen bonds which destabilises the lattice in these systems; increasing the ease with which a liquid can form at these eutectic points. The ability of TOPO to form room temperature liquids with levulinic acid as indicated by the phase diagram completed also highlights the potential for the in situ formation of a deep eutectic solvent which could be used to extract levulinic acid from fermentation broths.

NMR studies of the liquid samples were performed and highlighted that levulinic acid contributes directly to the acidity surrounding the phosphorus environment experienced by the phosphorus on TOPO. These studies also highlighted that the TOPO:levulinic acid eutectic point shown by the phase diagram at χ_{TOPO} = 0.4 have chemical shifts of a comparable value to that of the eutectic point of the recently published work on TOPO:phenol mixtures.[11] Therefore, perhaps a δ ^{31}P = 54.83 ppm (i.e. that of χ_{TOPO} = 0.4 for TOPO:levulinic acid) is indicative of the eutectic point for TOPO mixtures with a range of carboxylic acids and alcohols.

Density of TOPO:levulinic acid mixtures decrease with increasing temperature and the density of these mixtures decreases with increasing TOPO component at 20 °C.

Future work on the extraction of gallium using a TOPO:malonic acid deep eutectic solvent system will focus on extraction of gallium in the presence of competing metals such as zinc, copper and iron from acidic chloride sources and how these metals interfere with the ability of 2:1 TOPO:malonic to extract gallium or if extraction is selective to gallium. The next step in this process will be to remove gallium from the extractant phase and if metal co-extraction has occurred, to isolate gallium from these metals. It is thought that this purification will be achieved with electrodeposition using cyclic voltammetry to first strip gallium by recording the potential past the point of the gallium species reduction overnight and to subsequently SEM the plate to analyse with EDX whether or not there are gallium, iron, copper or zinc present. In addition to this, speciation of gallium in the extracted phase will be studied in order to complete this section of work. This will be pursued with the formation of a Jobs plot by diluting the extractant in a diluent. Further speciation work will also be studied using Raman spectroscopy to better understand the binding modes involved in this extraction of gallium (i.e. Ga-O and Ga-Cl) and will complement infra-red studies performed last year [ν(P=O) and ν(C=O)]. Crystal growth of a TOPO:malonic acid / gallium chloride species will also be pursued to obtain single crystal results.

Future work on TOPO:levulinic acid systems will focus on extraction of levulinic acid from model fermentation broth bio-refinery systems with the addition of neat TOPO to these feeds in order to

form an in situ TOPO:levulinic acid DES. The subsequent isolation of levulinic acid will also be pursued and any co-extraction of sulfuric acid or organics such as furfural or formic acid ideally suppressed.

References

1. A. P. Abbott, G. Capper, D. L. Davies, H. L. Munro, R. K. Rasheed and V. Tambyrajah, *Chem. Commun.*, 2001, 2010–2011.
2. Q. Zhang, K. De Oliveira Vigier, S. Royer and F. Jérôme, *Chem. Soc. Rev.*, 2012, **41**, 7108.
3. M. C. Kroon, M. Francisco, A. Van Den Bruinhorst and M. C. Kroon, 2013, **2012**, 3074–3085.
4. E. L. Smith, A. P. Abbott and K. S. Ryder, *Chem. Rev.*, 2014, **114**, 11060–11082.
5. A. P. Abbott, D. Boothby, G. Capper, D. L. Davies and R. K. Rasheed, *J. Am. Chem. Soc.*, 2004, **126**, 9142–9147.
6. D. J. G. P. van Osch, L. F. Zubeir, A. van den Bruinhorst, M. A. A. Rocha and M. C. Kroon, *Green Chem.*, 2015, **17**, 4518–4521.
7. D. J. G. P. van Osch, D. Parmentier, C. H. J. T. Dietz, A. van den Bruinhorst, R. Tuinier and M. C. Kroon, *Chem. Commun.*, 2016, **52**, 11987−11990.
8. J. Cao, M. Yang, F. Cao, J. Wang and E. Su, *ACS Sustain. Chem. Eng.*, 2017, **5**, 3270–3278.
9. J. . Cao, L. . Chen, M. . Li, F. . Cao, L. . Zhao and E. Su, *Green Chem.*, 2018, **20**, 1879−1886.
10. B. D. Ribeiro, C. Florindo, L. C. Iff, M. A. Z. Coelho and I. M. Marrucho, *ACS Sustain. Chem. Eng.*, 2015, **3**, 2469–2477.
11. M. Gilmore, E. N. Mccourt, F. Connolly, P. Nockemann and J. D. Holbrey, *ACS Sustain. Chem. Eng*, 2018, **6**, 17323–17332.
12. I. Mekis, D. V Talapin, A. Kornowski, M. Haase and H. Weller, *J. Phys. Chem.*, 2003, **107**, 7454–7462.
13. F. V Mikulec, M. Kuno, M. Bennati, D. A. Hall, R. G. Griffin and M. G. Bawendi, *J. Am. Chem. Soc*, 2000, **122**, 2532–2540.
14. T. Cassagneau, T. E. Mallouk and J. H. Fendler, *J. Am. Chem. Soc*, 1998, **120**, 7848–7859.
15. T. Trindade and P. O. Brien, *Chem Mater*, 1997, **9**, 523–530.
16. A. A. Guzelian, J. E. B. Katari, A. V Kadavanich, U. Banin, K. Hamad, E. Juban, A. P. Alivisatos, R. H. Wolters, C. C. Arnold and J. R. Heath, *J. Phys. Chem.*, 1996, **100**, 7212–7219.
17. T. Sato, T. Nakamura and S. Ishikawa, *Solvent Extr. Ion Exch.*, 1984, **2**, 201–212.
18. E. K. Watson and W. A. Rickelton, *Solvent Extr. Ion Exch.*, 1992, **10**, 879–889.
19. P. O. . Saboe, L. P. . Manker, W. E. . Michener, D. J. . Peterson, D. G. . Brandner, S. P. . Deutch, M. . Kumar, R. M. . Cywar, B. G. T.; and E. M. Karp, *Green Chem.*, 2018, **20**, 1791–1804.
20. T. Brouwer, M. Blahusiak, K. Babic and B. Schuur, *Sep. Purif. Technol.*, 2017, **185**, 186–195.
21. G. Kim, S. Park and B. Um, *Ind. Crop. Prod.*, 2016, **89**, 34–44.
22. S. Uenoyama, T. Hano, M. Hirata and S. Miura, *J. Chem. Technol. Biotechnol.*, 1996, **67**, 260–264.
23. P. Praveen and K. C. Loh, *Chem. Eng. J.*, 2014, **255**, 641–649.
24. P. Praveen and K. Loh, *Chemosphere*, 2016, **153**, 405–413.
25. P. Praveen and K. Loh, *J. Memb. Sci.*, 2013, **437**, 1–6.
26. P. Taylor, E. K. Watson, W. A. Rickelton, A. J. Robertson and T. J. Brown, *Solvent Extr. Ion Exch.*, 1988, **6**, 207–220.
27. E. Y. Tupikina, M. Bodensteiner, P. M. Tolstoy, G. S. Denisov and I. G. Shenderovich, *J. Phys. Chem. C*, 2018, **122**, 1711–1720.

QUILL Quarterly Report

February – April 2019

Name:	**Dr Martyn Earle**		
Supervisor(s):			
Position:	Senior Research Fellow		
Start date:	01-09-2018	Anticipated end date:	31-12-2019
Funding body:	BBSRC		

Green Lanthanide Separations using Countercurrent Chromatography and Ionic Liquids

Background

The separation of lanthanide elements often involves the use of acids, acidic reagents, buffers and complexing agents based on phosphorous, oxygen and nitrogen containing ligands. In this work we have developed a methodology capable of performing the separation of rare earth (lanthanide) metals, which does not require the use of acidic, corrosive, toxic or polluting reagents and expensive complexing agents, used in lanthanide production and recycling industries. A series of green (acid free) approaches to lanthanide separations using hydrophobic chloride ionic liquid stationary phases and pH neutral aqueous mobile phases are presented for a model separation of praseodymium(III) nitrate from erbium(III) nitrate.

Objective of this work

The objectives of the work are to develop a clean method for separating lanthanide elements, using ionic liquids as stationary phase and water as a mobile phase in countercurrent chromatography.

Progress to date

The work has developed a model separation of Erbium Nitrate from Praseodymium nitrate. The separation works on 85-93% separation on 4.0 g samples of the mixed metals in under 25 minutes. This is to be sent to Green Chemistry for Publication.

Conclusions and future work

The complete elimination of corrosive chemicals from lanthanide separations would dramatically improve the safety and reduce the environmental footprint of this notorious class of industrial separations. Water / hydrophobic $[P_{6\,6\,6\,14}]Cl$ + organic solvent - solvent systems allow lanthanide separations without the need for acids, pH buffers or expensive complexing agents. Additionally, the mobile phase, being water (saturated with a hydrophobic organic solvent) makes these separations clean, safe and very inexpensive to run and operate.

The future is to increase the scale of the separation and use the CPC instrument for automated separations.

Green Lanthanide Separations using Countercurrent Chromatography and Ionic Liquids

Lanthanide nitrate distribution ratios

The following solvent systems: A1, A2, A3 and A4 were prepared using the solvents and ionic liquids in Table 1. The values for D_R in parentheses refers to the distribution ratio in the

presence of the metal in parentheses, such that Pr(Er) refers to the D_R value of Praseodymium(III) in the presents of Erbium(III).

Table 1 - The compositions and absorbances of the solvent system phases used in the lanthanide nitrate separations measured at 50 °C.

Solvent System	Component	Quantity	Density in g cm^{-3} at 50 °C			**Dr = $[Ln^{3+}]_{SP}$ / $[Ln^{3+}]_{MP}$**
			SP	MP	MP-SP	
A1	Water	800 cm^3	0.890	0.972	0.082	Pr 0.116
	Ethyl Ethanoate	200 cm^3				Pr(Er) 0.019
	$[P_{6\,6\,6\,14}]Cl$	200 cm^3				Er 0.503
	TBPO	0.0 g				Er(Pr)0.16
A2	Water	800 cm^3	0.894	0.974	0.080	Pr 0.135
	Ethyl Ethanoate	200 cm^3				Pr (Er) 0.062
	$[P_{6\,6\,6\,14}]Cl$	200 cm^3				Er 0.730
	TBPO	20.0 g				Er(Pr) 0.262
A3	Water	40 cm^3	---	---	---	Pr 0.178
	Ethyl Ethanoate	10 cm^3				Pr(Er) 0.136
	$[P_{6\,6\,6\,14}]Cl$	10 cm^3				Er 0.920
	TBPO	2.0 g				Er(Pr) 0.676
A4	Water	40 cm^3	---	---	---	Pr 0.232
	Ethyl Ethanoate	10 cm^3				Pr(Er) 0.336
	$[P_{6\,6\,6\,14}]Cl$	10 cm^3				Er 1.29
	TBPO	3.0 g				Er(Pr) 1.85

$[P_{6\,6\,6\,14}]Cl$ = trihexyltetradecylphosphonium chloride, TBPO = tributylphosphine oxide

For each solvent system A1 – A4, $Ln(NO_3)_3.(H_2O)_n$ (n=6 for Pr, n=5 for Er) salts (0.30 g) were dissolved in ca. 0.7 cm^3 of MP (lower aqueous phase) + 0.7 cm^3 of SP (ionic / organic upper phase) at 50 °C. Both phases were made up to a volume of 1.00 ml each (total = 2.00 cm^3) in a volumetric flask and left to equilibrate for 1 hour. The UV-Vis absorbances at 445nm for ($Pr(NO_3)_3$) (ε = 0.983 (Figure 2)), and 523nm ($Er(NO_3)_3$) (ε = 0.461 (Figure 3)) or 652 nm (ε = 0.207(Figure 4)) were measured (in a 1mm path length quartz UV-Vis curvette) for each phase. The distribution ratios were calculates and are shown in Figure 1 and Table 1. Also, a mixture of $Pr(NO_3)_3.6(H_2O)$ and $Er(NO_3)_3.5(H_2O)$ (1.000 : 1.000 ratio by weight {or 1.019 : 1.000 molar ratio}) was prepared and dissolved in the solvent systems A1-A4 in order to determine how the metals affect each-others distribution ratio. This data is also shown in Table 1 and Figure 1. Assuming that the extinction coefficients of absorption peaks of the lanthanide salts were not affected by the compositional variation of the solvent system (which only applies to f-block elements), the distribution ratios were calculated using the formula $Dr_{(Ln)} = [Ln^{3+}]_{SP}/[Ln^{3+}]_{MP}$ = Abs. (Ln^{3+}) in SP/Abs. (Ln^{3+}) in MP. The UV-Vis spectra of 0.30 g of Pr(III), Nd(III) and Er(III) nitrate salts (0.30g) in water (1.00 cm^3) are shown in Figure 5.

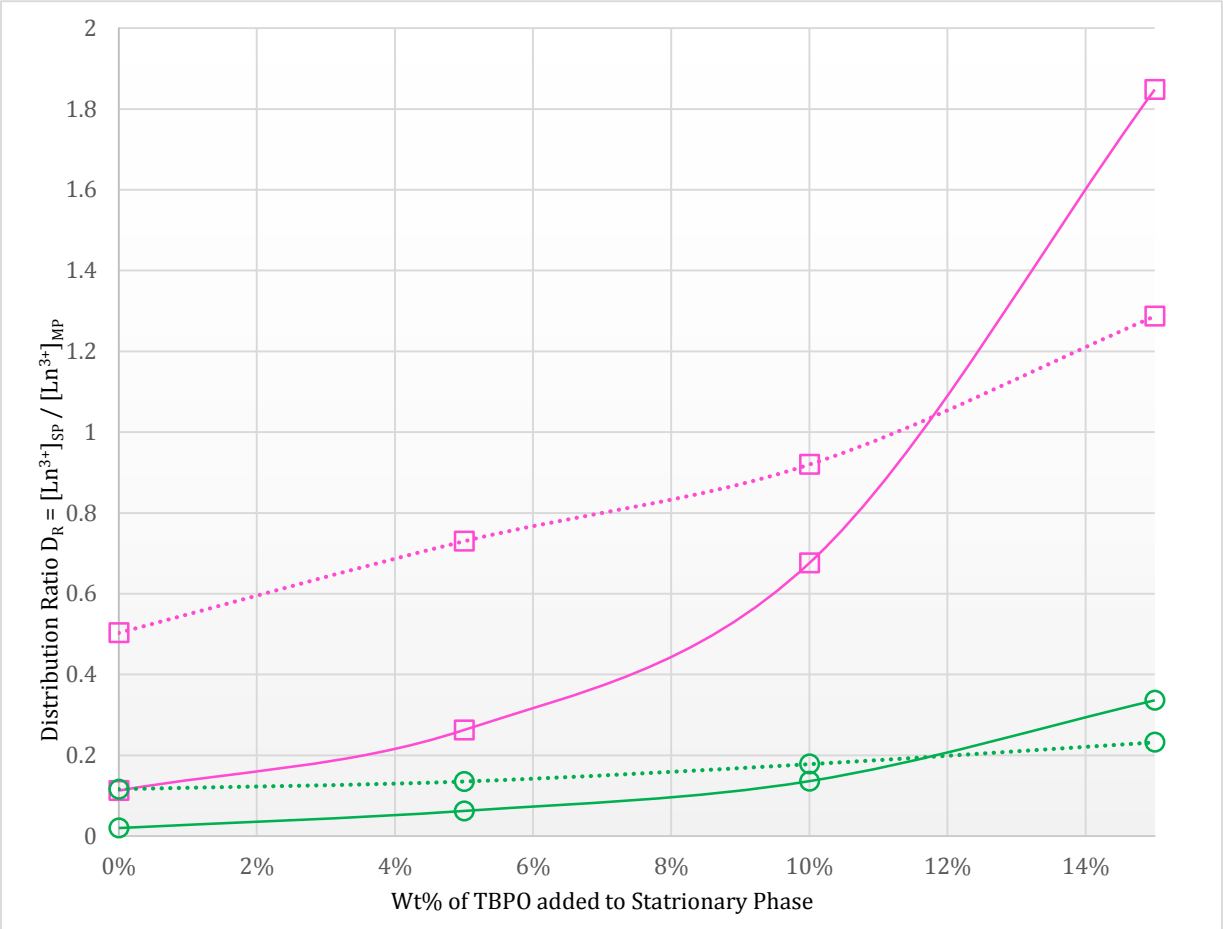

Figure 1, The variation of distribution ratio ($Dr_{(Ln)} = [Ln^{3+}]_{SP} / [Ln^{3+}]_{MP}$ of $Ln(NO_3)_3.n(H_2O)$ (Ln = Pr, n = 6; Ln = Er, n = 5) (0.30 g) dissolved in 2.00 cm^3 of the solvent systems A1, A2, A3 and A4 (Table 1) (consisting of 1.00 cm^3 of MP + 1.00 cm^3 of SP) at 50 °C. The dotted lines show the Ln^{3+} (**Green** = Pr^{3+} and **Magenta** = Er^{3+}) distribution ratio for the individual metals (0.30g) in the solvent systems A1-A4, and the solid lines show the distribution ratios for a 1:1 mixture of Pr^{3+} (0.15g) and Er^{3+}(0.15g). Error in the distribution ratio data points = ±0.04.

Extinction Coefficient Calculations for $Ln(NO_3)_3$ salts in water.

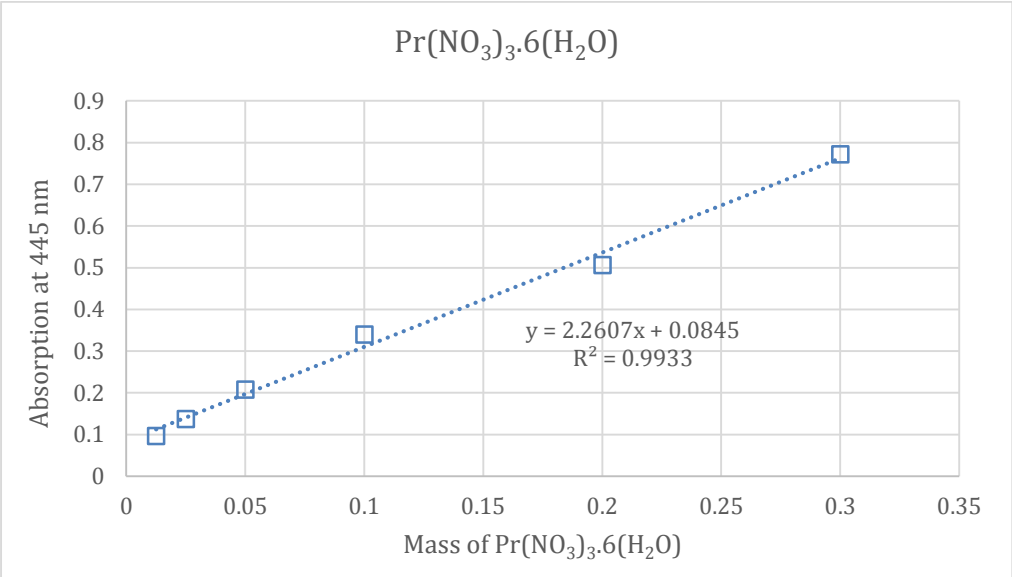

Figure 2 - The absorbance of $Pr(NO_3)_3.6(H_2O)$ at 445nm by UV-Vis spectroscopy for different masses dissolved in 1.00 cm^3 of water.

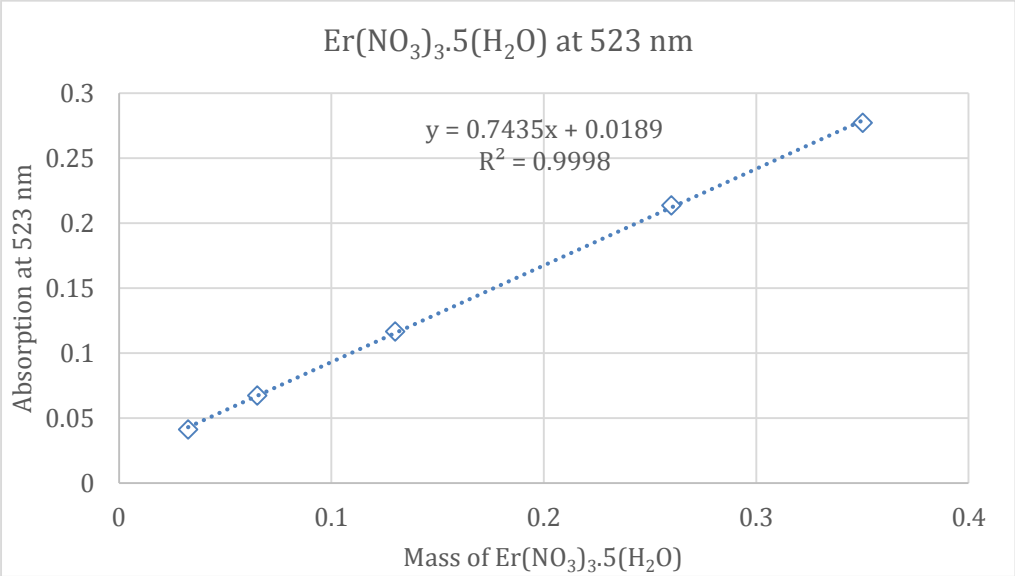

Figure 3- The absorbance of $Er(NO_3)_3.5(H_2O)$ at 523nm by UV-Vis spectroscopy for different masses dissolved in 1.00 cm^3 of water.

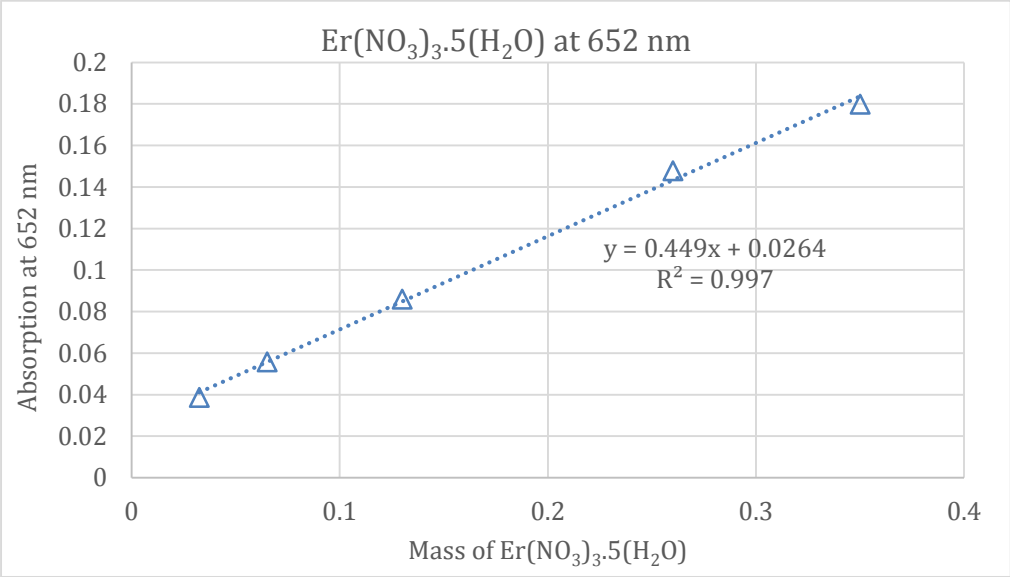

Figure 4 - The absorbance of $Er(NO_3)_3.5(H_2O)$ at 652nm by UV-Vis spectroscopy for different masses dissolved in 1.00 cm^3 of water.

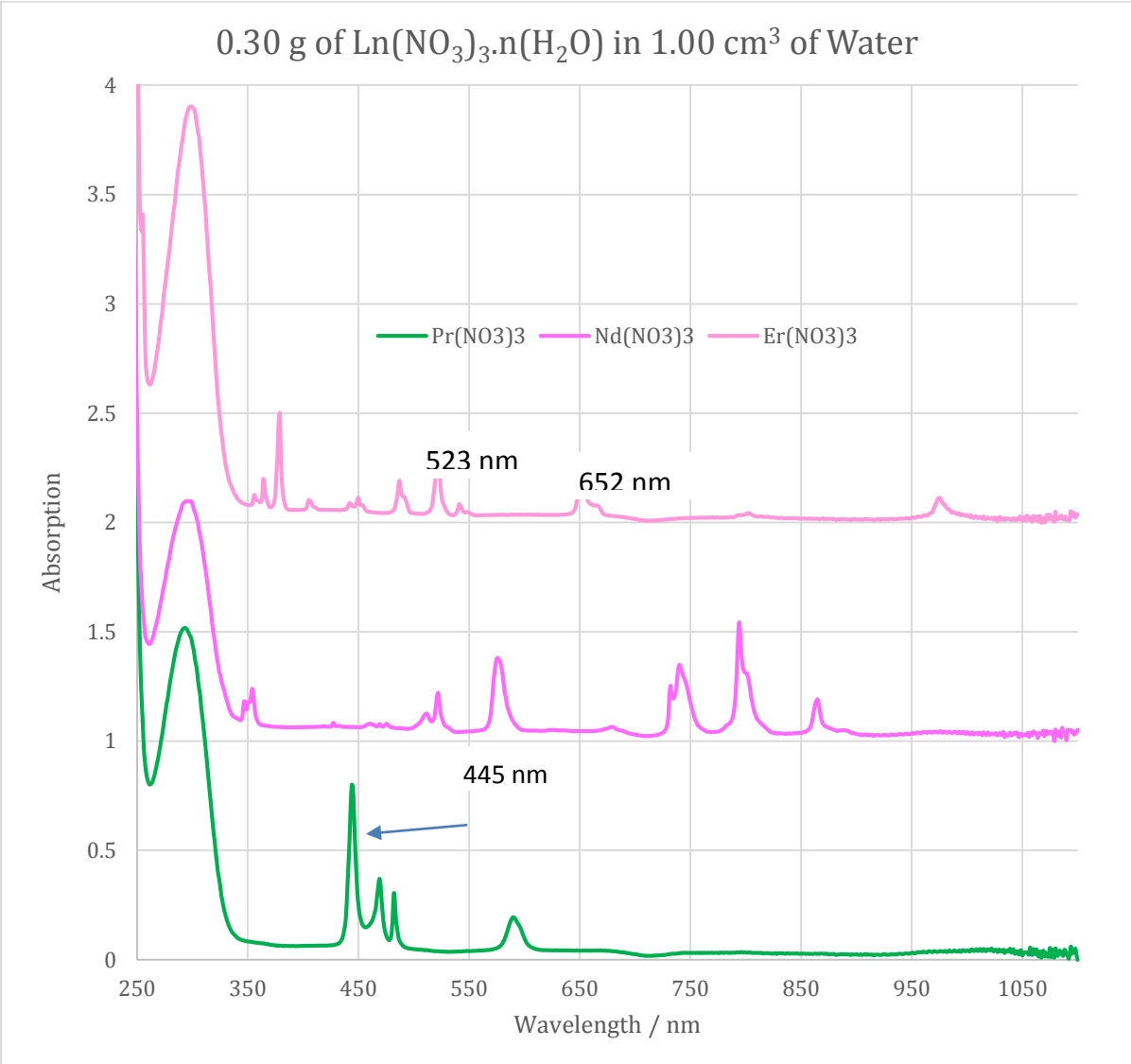

Figure 5 - The UV-Vis spectra of Pr(III), Nd(III) and Er(III) nitrate hydrate salts (0.30g) in water (1.0 cm^3).

Lanthanide Separation Procedure

Stationary Phase Retention Curves

The IL-Prep™ ionic liquid-liquid chromatography (ILLC) machine consists of a J-type centrifuge with four stainless steel (SS) coils, with two coils on each bobbin. Using the apparatus shown in Figure 6, in recirculation mode, the stationary phase retention curves (Figure 7) for six solvent systems (Table 1) used in the lanthanide separations were determined for Coil 2 (133 cm^3, 2.1 mm internal diameter, 39.6 m length) at 50 °C and 890 r.p.m., using the methodology described in the literature.

The solvent systems with the highest density contrast between the MP and SP (Table 1) have higher stationary phase retentions, and the addition of 5 wt% TBPO to the SP slightly increases the stationary phase retention values. Generally, high stationary phase retention values improve separation performance and reduce the amount of mobile phase required for the separation.

Previous research on metal separations used ethyl ethanoate as a co-solvent to reduce the viscosity of the $[P_{6\,6\,6\,14}]Cl$ containing phase,[16] but it was found that separations using 3-pentanone as a co-solvent (Table 1, B1 and B2) gave better separation performance and lower solvent system turbidity. The hexane containing solvent systems C1 and C2, have an increased density contrast between the MP and the SP (Table 1) leading to higher SP retention values, which generally improve the overall separations performance.

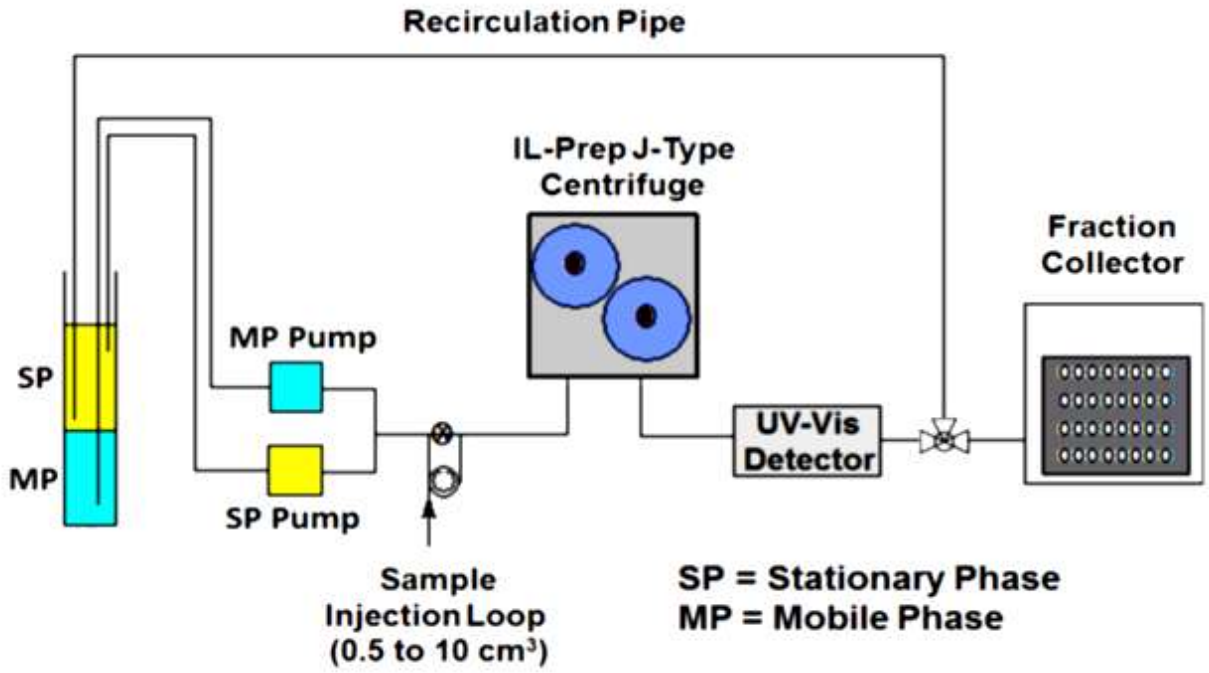

Figure 6 - A schematic of the IL-Prep™ CCC instrument, used in the lanthanide separations.

Figure 7 - The IL-Prep™ CCC instrument, pumps, detector, fraction collector, used in the lanthanide separations.

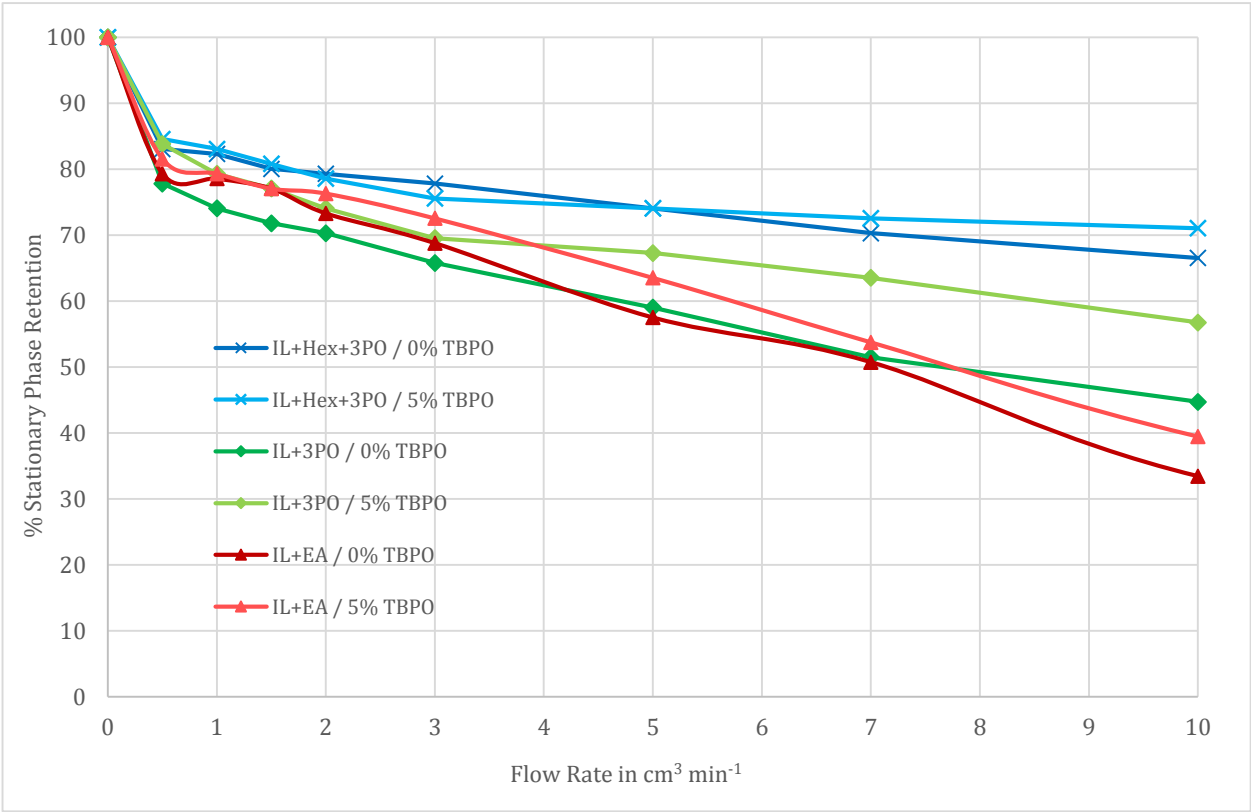

Figure 8 - The stationary phase retention curves for six solvent systems used in the lanthanide separations (Table 1, A1, A2, B1, B2, C1 and C2) using Coil 2 at 50 °C and 890 r.p.m.[17] The solvent systems are Dark Red (A1): water (800 cm^3) / [$P_{6\,6\,6\,14}$]Cl (200 cm^3) + ethyl ethanoate (200 cm^3);[17] Light Red (A2): water (800 cm^3) / [$P_{6\,6\,6\,14}$]Cl (200 cm^3) + ethyl ethanoate (200 cm^3) + 5 wt% TBPO in the SP; Dark Blue (C1): water (1000 cm^3) / [$P_{6\,6\,6\,14}$]Cl (200 cm^3) + hexane (270 cm^3) + 3-pentanone (30 cm^3); Light Blue (C2): water (1000 cm^3) / [$P_{6\,6\,6\,14}$]Cl (200 cm^3) + hexane (270 cm^3) + 3-pentanone (30 cm^3) + 5 wt% TBPO dissolved in the SP; and Dark Green (B1): water (800 cm^3) / [$P_{6\,6\,6\,14}$]Cl (200 cm^3) + 3-pentanone (200 cm^3); Light Green (B2): water (800 cm^3) / [$P_{6\,6\,6\,14}$]Cl (200 cm^3) 3-pentanone (200 cm^3) + 5 wt% TBPO dissolved in the SP. Error in data points = ± 3.0% stationary phase retention.

Solvent Systems

The lanthanide separation chosen for detailed study was the separation of $Pr(NO_3)_3.6H_2O$ from $Er(NO_3)_3.5H_2O$. These two lanthanide nitrate salts have non-overlapping UV-Vis absorption peaks in the visible part of the electromagnetic spectrum, making observation with the online UV-Vis detector (an ECOM Flash 14 DAD 800 Detector) straightforward and easy to visualise. In half of the separations, tributylphosphine oxide (TBPO) was added to the stationary phase at 5 wt% concentrations, to investigate its effects on separation performance. In all the experiments, the mobile phase was water (saturated with organic solvents). The SP was not consumed in the separations, and was reused for multiple separations (typically 5-10 times over 1-2 days of experimentation). The SP could be recovered and stored for future use by reverse pumping (in the tail to head direction) it from the ILLC coil using the MP. ^{1}H, ^{13}C, and ^{31}P NMR analysis of the stationary phase show that it was unchanged after use in 10 consecutive separations.

Lanthanide Separations Procedures

The typical procedure for the separations was as follows: the lanthanide(III) nitrate hexahydrate or pentahydrate salts (0.35 g to 2.0 g of each metal) were dissolved in mobile phase (4.0 cm^3) and loaded into the 5.0 cm^3 sample injection loop using a syringe. Coil 2 of the IL-Prep machine (at 50 °C, 890 r.p.m.) was first filled with stationary phase (tail to head direction), then the mobile phase was pumped into the coil (head to tail direction) at 1.0 cm^3 min^{-1} faster than the flow rate used in the separation under investigation. The separation was started by switching the sample injection valve to pass through the sample loop (Figure 6), starting the fraction collector (typically 3.2 cm^3 samples) and setting the computer to record the chromatogram, using ECOMAC chromatographic software (Version 1.7.3.0). The absorption peaks measured were 445 nm for praseodymium, and 652 or 523 nm for erbium, and the baseline measurements for the peaks were recorded at 422 (for $Pr(NO_3)_3$) and 620 nm (for $Er(NO_3)_3$). The baseline signal was subtracted from the lanthanide metal signals to obtain the peak heights and improve the signal to noise ratio of the peak measurements. A typical chromatogram is shown in Figure 8, and was obtained in two different ways. (A) Directly measurement of the metal absorption peaks and baseline signals in the effluent from the coil (Figure 6) without using a lanthanide selective dye.[27] The direct measurement simplifies product isolation from the aqueous mobile phase, but can produce noisy chromatograms due to variable turbidity of the mobile phase eluting from the coils, and bubbles of stationary phase passing through the detector cell. The data obtained from the in-line detector was processed using a computer spreadsheet (MS Excel), by subtracting the baseline signal (422 or 620 nm) from the raw lanthanide signal data (445nm for Pr(III) and 523 or 652nm for Er(III)), smoothing the data using a 10 to 30 second moving average, then applying a linear baseline correction. The spectra were integrated and normalised to give either $Er(NO_3)_3$ = 100% signal or $Pr(NO_3)_3$ = 100%, and the areas of the Ln(III) peaks were scaled to have an area difference of 1.019 : 1.000 (Pr(III) : Er(III)) dur to the molar ratio of $Ln(NO_3)_3$ salts were injected into the ILLC instrument (Pr = 435.01 g mol^{-1} and Er = 443.35 g mol^{-1}). Alternatively, the chromatograms could be constructed by measuring the UV-Vis absorption spectra of the samples in the fraction collector in a standard UV-Vis spectrophotometer using a 0.1 x 1.0 cm quartz cell. Figure 8 shows typical chromatograms for a $Pr(NO_3)_3$ / $Er(NO_3)_3$ separation (using 0.80 g of each metal) using the C2 solvent system: water (1000 cm^3) / $[P_{6\,6\,6\,14}]Cl$ (200 cm^3) + hexane (270 cm^3) + 3-pentanone (30 cm^3) solvent system, containing 5 wt% TBPO dissolved in the stationary phase. The solid lines (Figure 8)

represent the chromatograms obtained using the in-line detector measured at 445 nm for Pr and 523 nm for Er. The dashed lines show the chromatogram obtained from the samples collected in the fraction collector. Of the two methods, the in-line detector data in Figure 8 should is preferred, due to its better temporal resolution (*ie* the fraction collector chromatogram has a temporal resolution of ±3.2 minutes *vs* a temporal resolution of 10-30 seconds for the in-line detector).

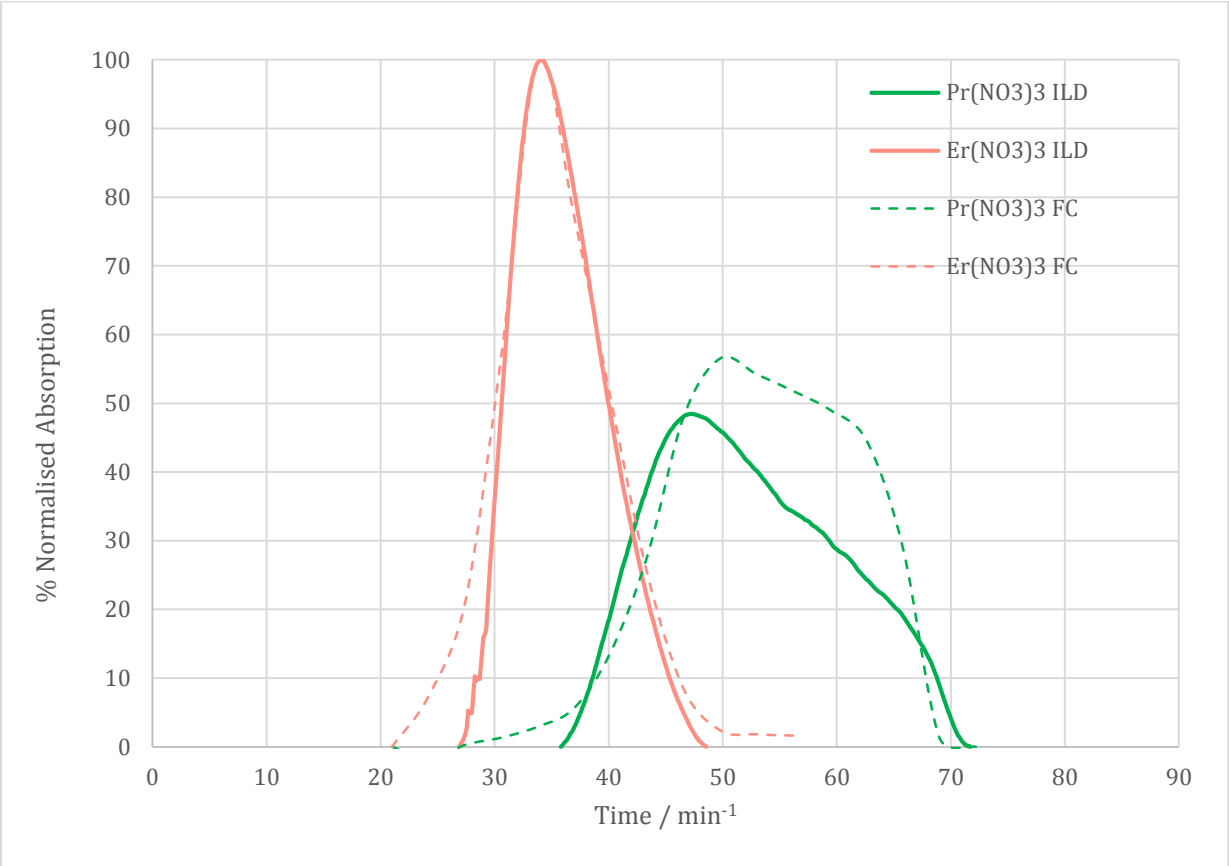

Figure 9 - The chromatograms obtained for the separation of aqueous $Pr(NO_3)_3.6(H_2O)$ (0.80 g, green lines) from $Er(NO_3)_3.5(H_2O)$ (0.80 g, pink line) using a water (1000 cm^3) / $[P_{6\,6\,6\,14}]Cl$ (200 cm^3) + hexane (270 cm^3) + 3-pentanone (30 cm^3) solvent system containing 5 wt% TBPO dissolved in the stationary phase. This was carried out using Coil 2 at 890 r.p.m., at 1.00 cm^3 min^{-1} flow rate, and 50 °C. The solid lines are from the online spectrometer measurements (Figure 6) (Error = ± 5.0%) and the dashed lines are based on the offline measurement of the absorption values of the samples collected in the fraction collector (3.2 cm^3 samples per tube) and ± 10% error.

Table 2. The % of $Pr(NO_3)_3.6(H_2O)$ completely separated from $Er(NO_3)_3.5(H_2O)$ as determined by integration of the non-overlapping $Ln(NO_3)_3$ peaks in ILLC separations at 50 °C, 890 r.p.m. on coil 2 at various flow rates and sample loadings. The numbers in bold show the best separation obtained for the solvent system employed. Error = ± 5.0% in integration values.

Entry	Solvent System	Mass of each $Ln(NO_3)_3.$ $n(H_2O)$ n = 5 or 6	Flow Rate in cm^3 min^{-1}	% Integration of completely separated salts			
				$Er(NO_3)_3$ Eluted in a Pure Form	Volume of MP Pumped for the $Er(NO_3)_3$ Peak / cm^3	$Pr(NO_3)_3$ Eluted in a Pure Form	Volume of MP Pumped for the $Pr(NO_3)_3$ Peak / cm^3
01	**A1**	**0.80**	**0.5**	**0**	**38.2**	**32**	**42.1**
02	A1	0.80	1.0	0	36.8	15	42.7
03	A2	0.80	1.5	0	45.5	7	47.0
04	**A2**	**0.80**	**2.0**	**0**	**48.5**	**10**	**51.2**
05	**B1**	**0.80**	**0.5**	**0**	**34.7**	**72**	**49.0**
06	B1	0.80	1.0	0	34.0	70	45.9
07	B1	0.80	2.0	0	36.9	39	44.7
08	B1	0.80	3.0	0	36.5	47	46.6
09	B1	0.80	4.0	0	37.5	51	49.4
10	B1	0.80	5.0	0	40.1	53	53.2
11	B2	0.80	1.0	9	48.9	78	59.7
12	B2	0.80	2.0	12	42.6	54	49.2
13	**B2**	**0.80**	**3.0**	**41**	**54.8**	**88**	**70.7**
14	B2	0.80	4.0	50	70.7	48	102.5
15	C1	0.80	0.5	0.1	33.7	2	37.9
16	C1	0.80	1.0	0.01	32.2	4	34.3
17	C1	0.80	2.0	0	35.8	44	45.1
18	C1	0.80	3.0	3	37.2	45	48.1
19	C1	0.80	4.0	55	38.9	61	54.4
20	C1	0.35	2.0	0	30.1	41	40.1
21	C1	0.50	2.0	0	32.1	41	47.4
22	C1	1.40	2.0	0	40.1	78	57.7
23	**C1**	**2.00**	**2.0**	**68**	**44.0**	**84**	**61.1**
24	C2	0.35	1.5	58	37.5	52	48.0
25	C2	0.50	1.5	74	33.5	61	40.0
26	C2	0.80	1.5	77	38.8	52	54.1
27	C2	1.40	1.5	78	43.6	81	68.5
28	**C2**	**2.00**	**1.5**	**85**	**61.2**	**93**	**86.2**
29	C2	0.80	0.5	0.4	36.8	61	48.0
30	C2	0.80	1.0	53	51.1	68	71.0
31	C2	0.80	2.0	86	49.3	89	88.4
32	C2	0.80	3.0	73	46.8	85	71.0
33	C2	0.80	4.0	84	40.3	92	104
34	C2	0.80	5.0	56	45.5	82	80.5

A1 Chromatograms

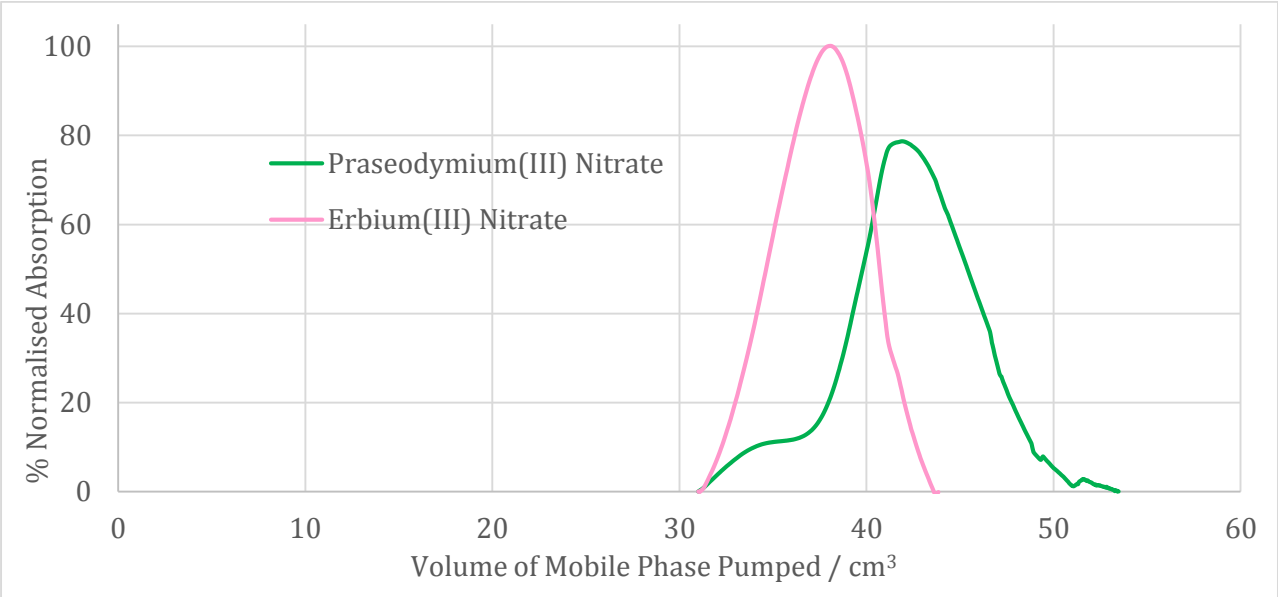

Figure A1 - Entry 01, Solvent System = A1, 0.50 cm^3 min^{-1}, 0.80g ($Pr(NO_3)_3.6(H2O)$ + 0.80g $Er(NO_3)_3.5(H_2O)$.

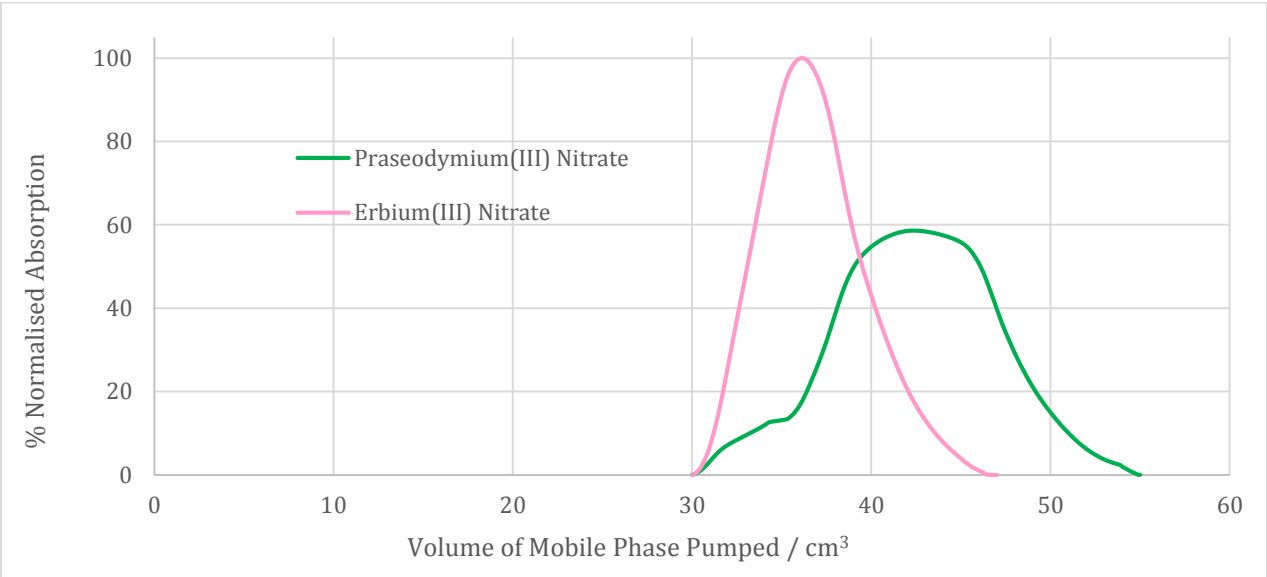

Figure A1 - Entry 02, Solvent System = A1, 1.00 cm^3 min^{-1}, 0.80g ($Pr(NO_3)_3.6(H2O)$ + 0.80g $Er(NO_3)_3.5(H_2O)$.

A2 Chromatograms

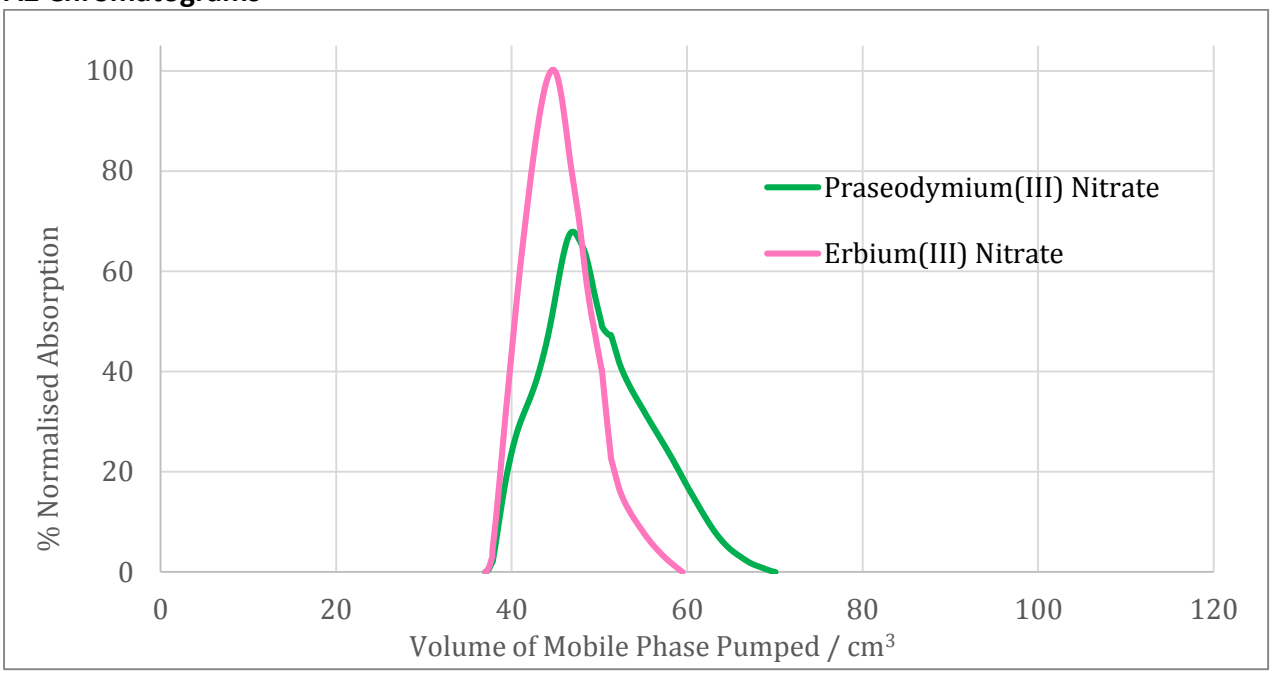

Figure A2 - Entry 03, Solvent System = A2, 1.50 cm^3 min^{-1}, 0.80g ($Pr(NO_3)_3.6(H2O)$ + 0.80g $Er(NO_3)_3.5(H_2O)$.

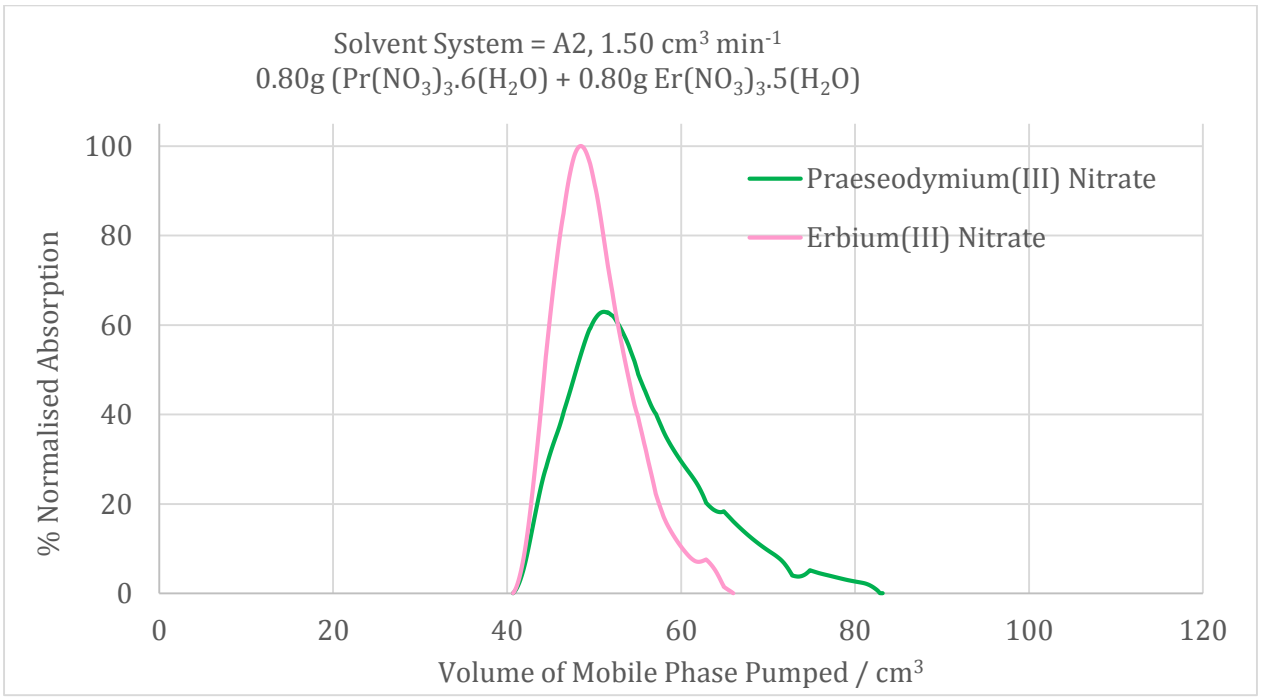

Figure A2 - Entry 04, Solvent System = A2, 2.0 cm^3 min^{-1}, 0.80g ($Pr(NO_3)_3.6(H2O)$ + 0.80g $Er(NO_3)_3.5(H_2O)$.

B1 Chromatograms

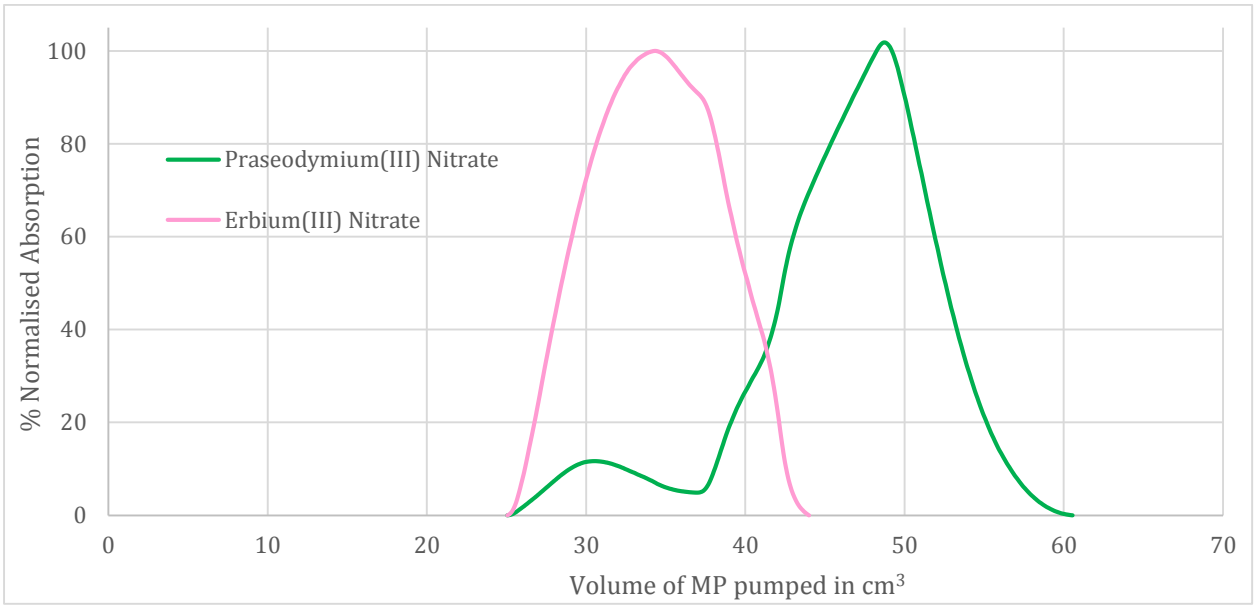

Figure B1 - Entry 05, Solvent System = B1, 0.5 cm^3 min^{-1}, 0.80g ($Pr(NO_3)_3.6(H2O)$ + 0.80g $Er(NO_3)_3.5(H_2O)$.

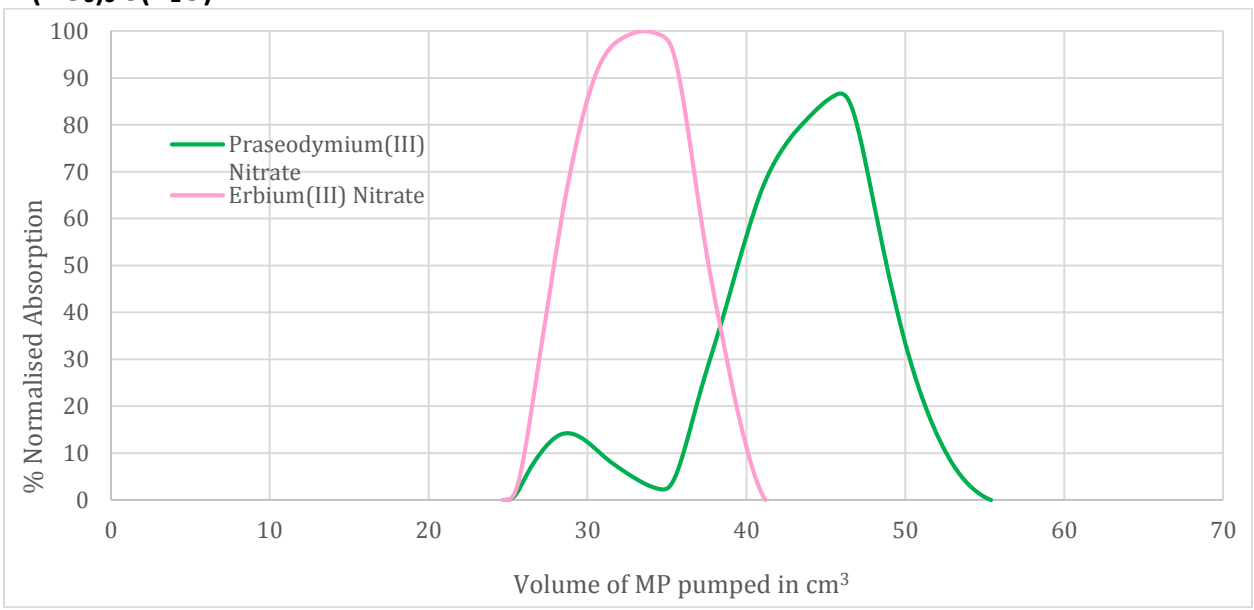

Figure B1 - Entry 06, Solvent System = B1, 1.0 cm^3 min^{-1}, 0.80g ($Pr(NO_3)_3.6(H2O)$ + 0.80g $Er(NO_3)_3.5(H_2O)$.

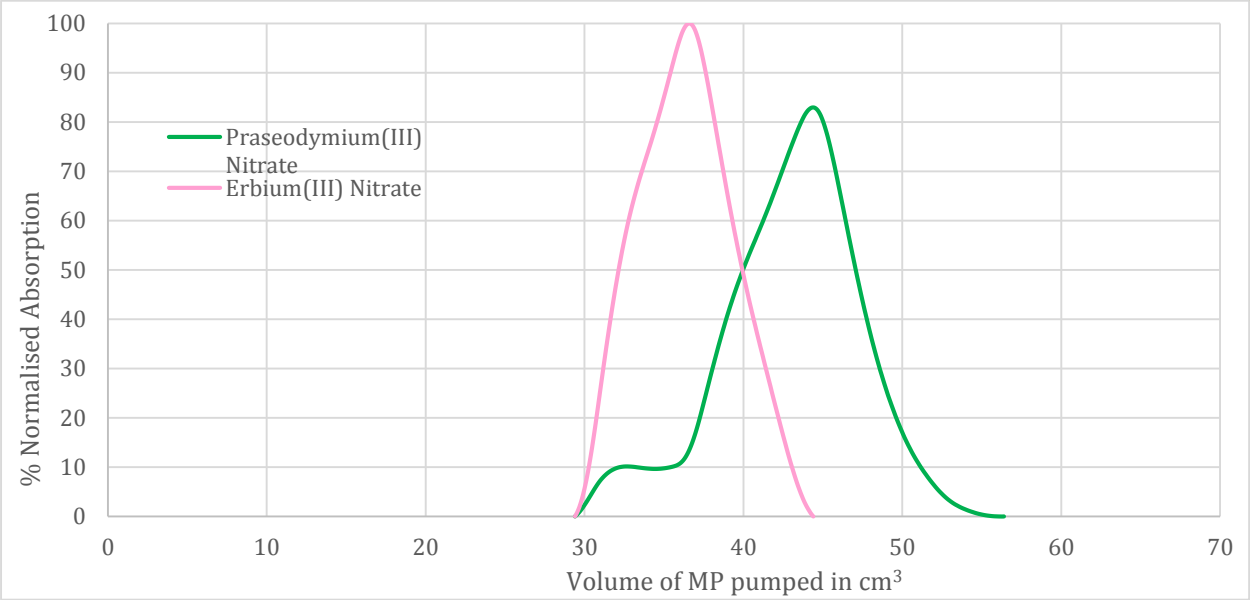

Figure B1 - Entry 07, Solvent System = B1, 2.0 cm^3 min^{-1}, 0.80g ($Pr(NO_3)_3.6(H2O)$ + 0.80g $Er(NO_3)_3.5(H_2O)$.

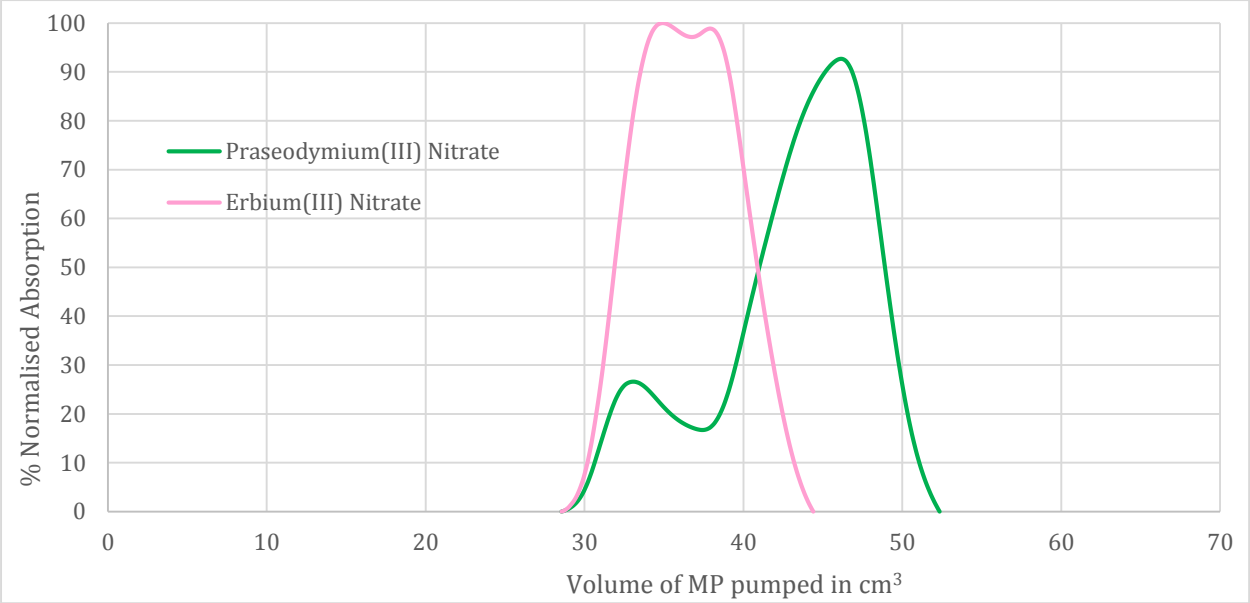

Figure B1 - Entry 08, Solvent System = B1, 3.0 cm^3 min^{-1}, 0.80g ($Pr(NO_3)_3.6(H2O)$ + 0.80g $Er(NO_3)_3.5(H_2O)$.

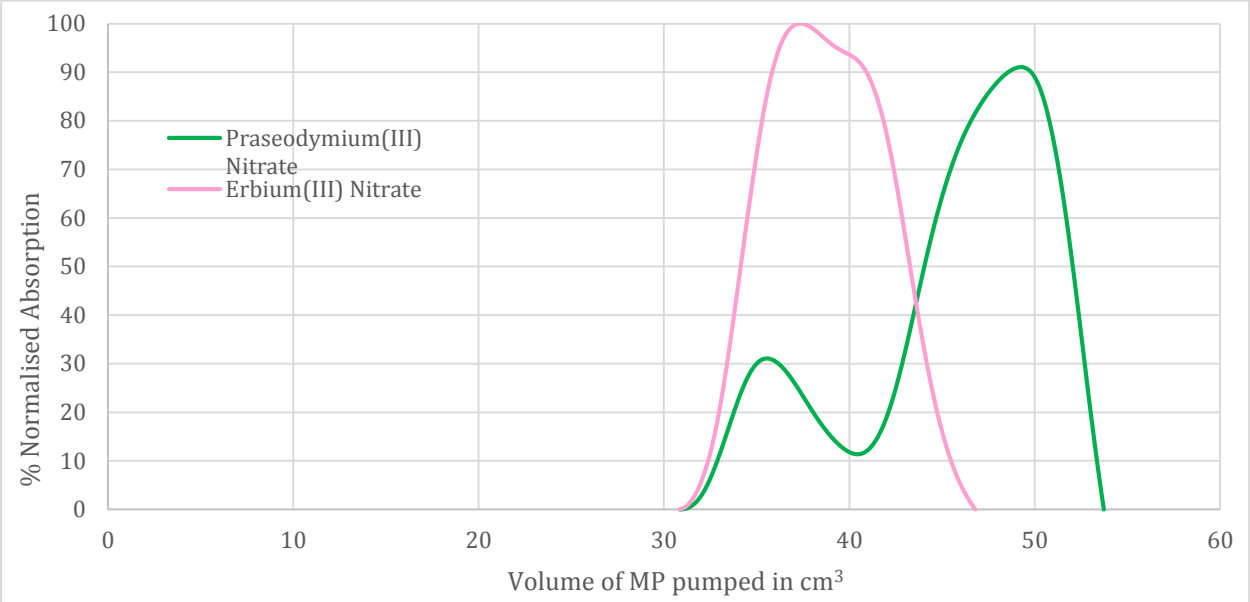

Figure B1 - Entry 09, Solvent System = B1, 4.0 cm^3 min^{-1}, 0.80g ($Pr(NO_3)_3.6(H2O)$ + 0.80g $Er(NO_3)_3.5(H_2O)$.

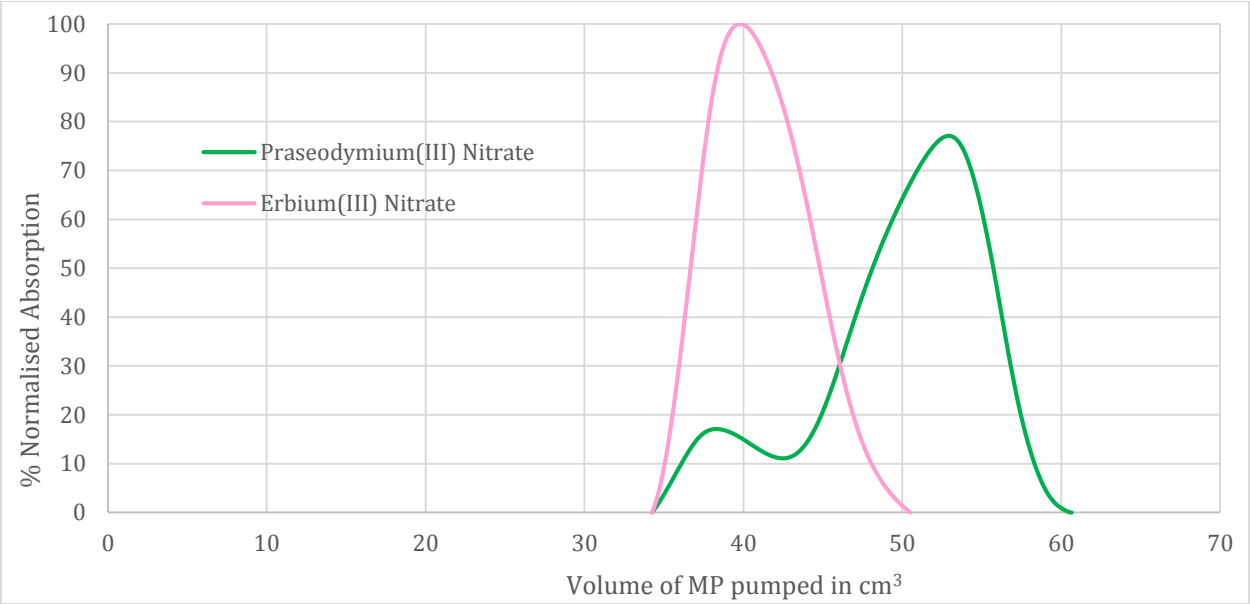

Figure B1 - Entry 010, Solvent System = B1, 5.0 cm^3 min^{-1}, 0.80g ($Pr(NO_3)_3.6(H2O)$ + 0.80g $Er(NO_3)_3.5(H_2O)$.

B2 Chromatograms

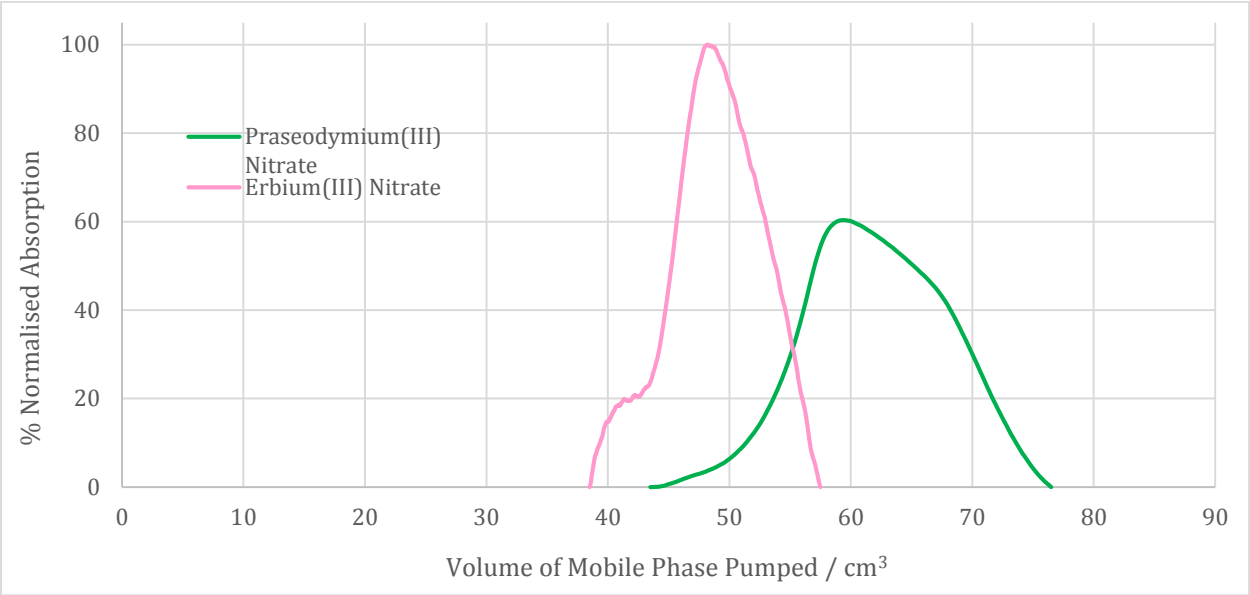

Figure B2 - Entry 11, Solvent System = B2, 1.0 cm^3 min^{-1}, 0.80g ($Pr(NO_3)_3.6(H2O)$ + 0.80g $Er(NO_3)_3.5(H_2O)$.

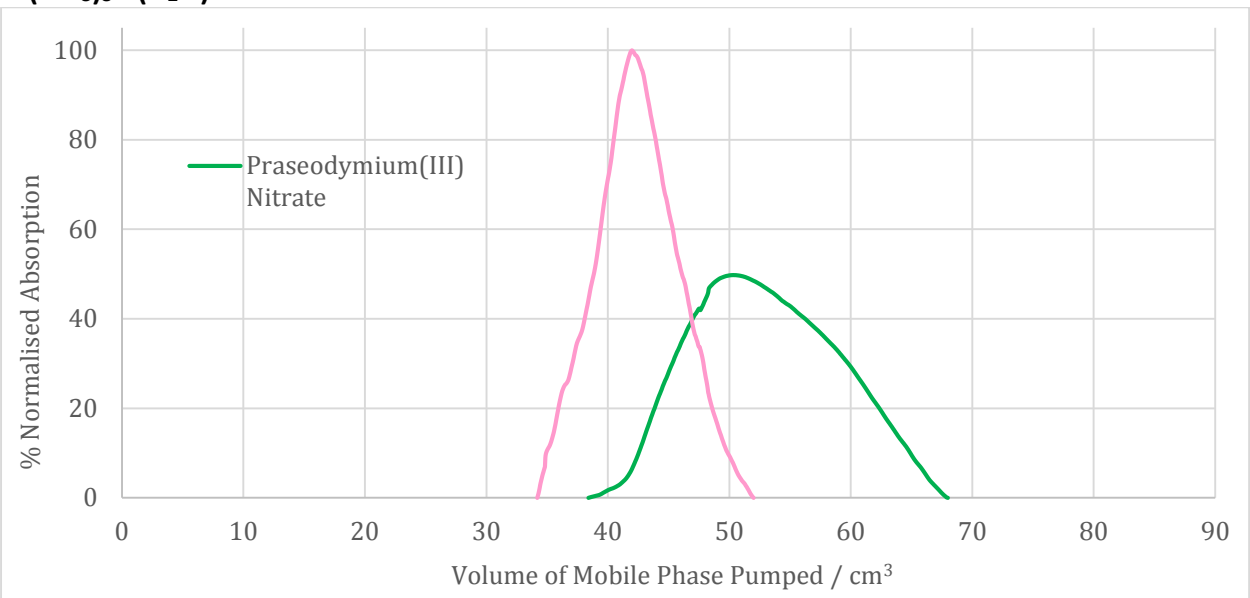

Figure B2 - Entry 12, Solvent System = B2, 2.0 cm^3 min^{-1}, 0.80g ($Pr(NO_3)_3.6(H2O)$ + 0.80g $Er(NO_3)_3.5(H_2O)$.

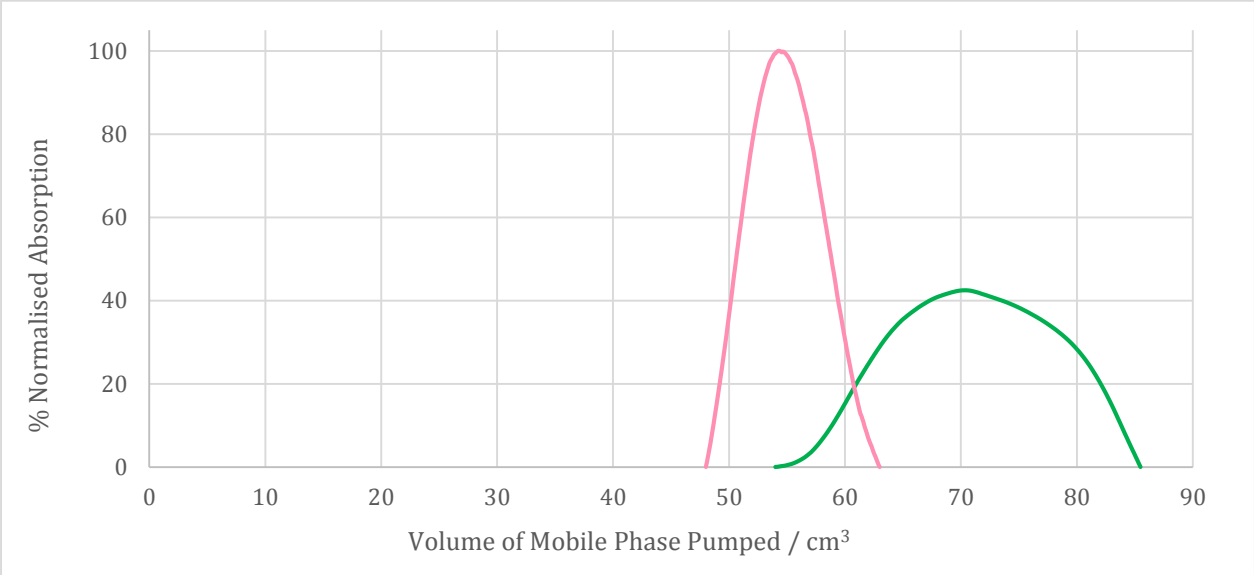

Figure B2 - Entry 13, Solvent System = B2, 0.5 cm^3 min^{-1}, 0.80g ($Pr(NO_3)_3.6(H2O)$ + 0.80g $Er(NO_3)_3.5(H_2O)$.

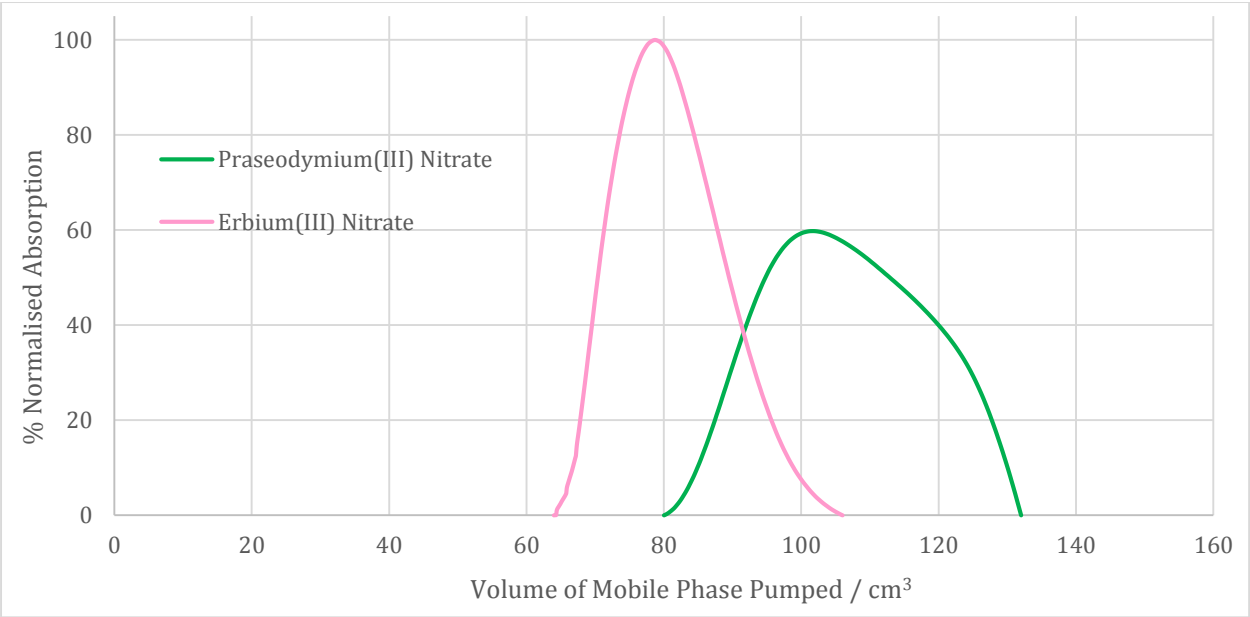

Figure B2 - Entry 14, Solvent System = B2, 4.0 cm^3 min^{-1}, 0.80g ($Pr(NO_3)_3.6(H2O)$ + 0.80g $Er(NO_3)_3.5(H_2O)$.

C1 Chromatograms

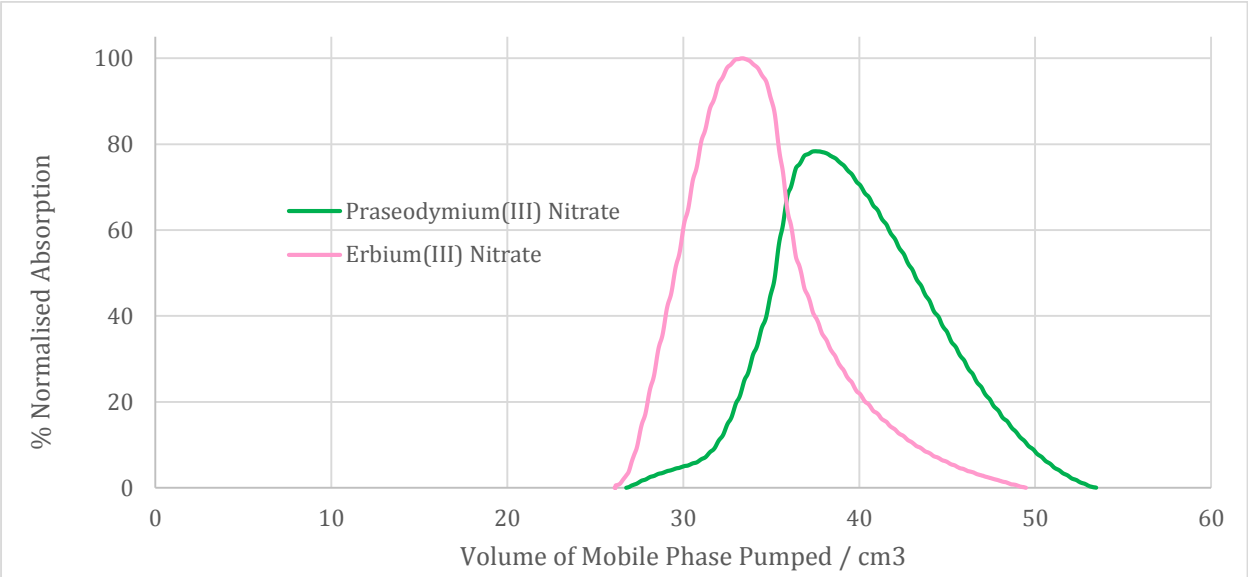

Figure C1 - Entry 15, Solvent System = C1, 0.5 cm^3 min^{-1}, 0.80g ($Pr(NO_3)_3.6(H_2O)$ + 0.80g $Er(NO_3)_3.5(H_2O)$.

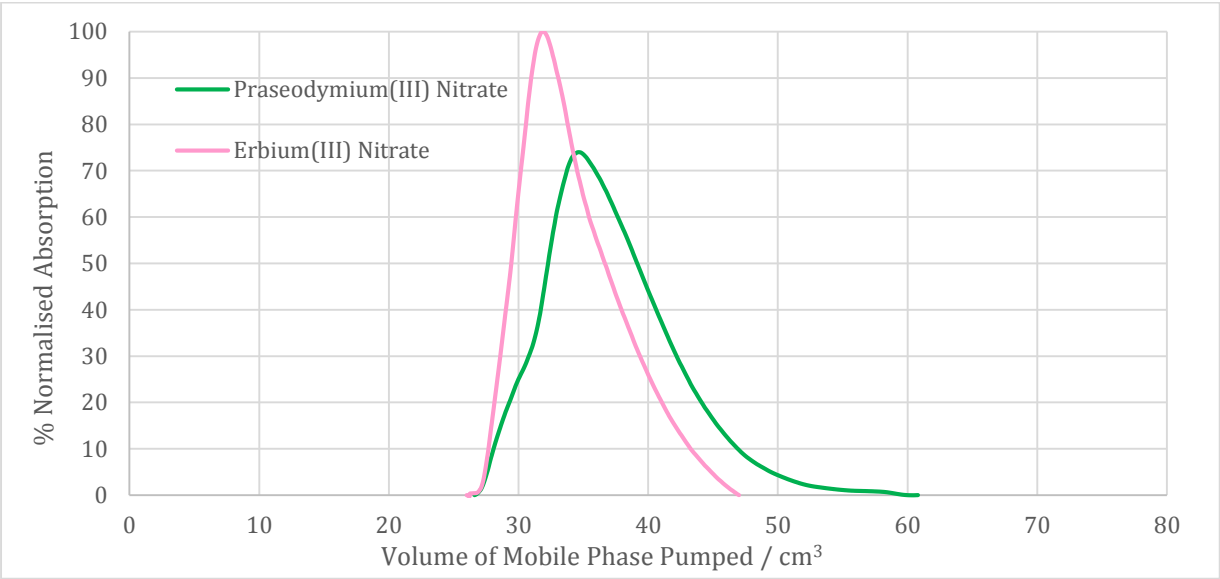

Figure C1 - Entry 16, Solvent System = C1, 1.0 cm^3 min^{-1}, 0.80g ($Pr(NO_3)_3.6(H_2O)$ + 0.80g $Er(NO_3)_3.5(H_2O)$.

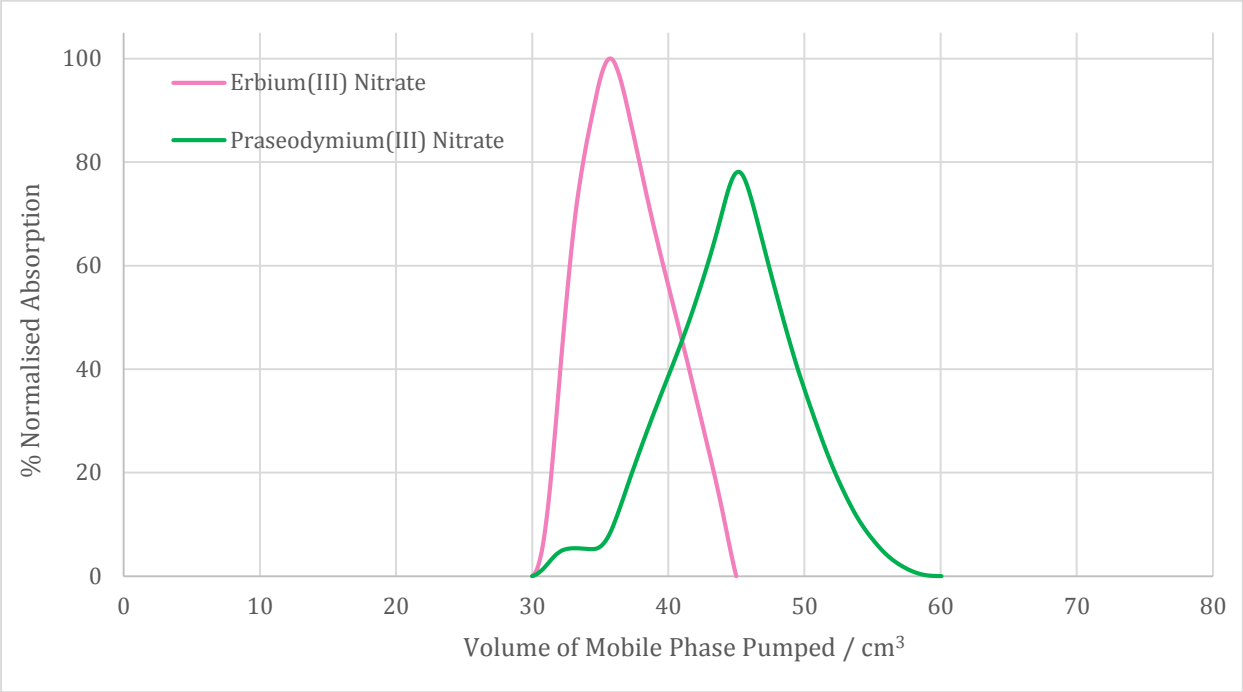

Figure C1 - Entry 17, Solvent System = C1, 2.0 cm^3 min^{-1}, 0.80g ($Pr(NO_3)_3.6(H_2O)$ + 0.80g $Er(NO_3)_3.5(H_2O)$.

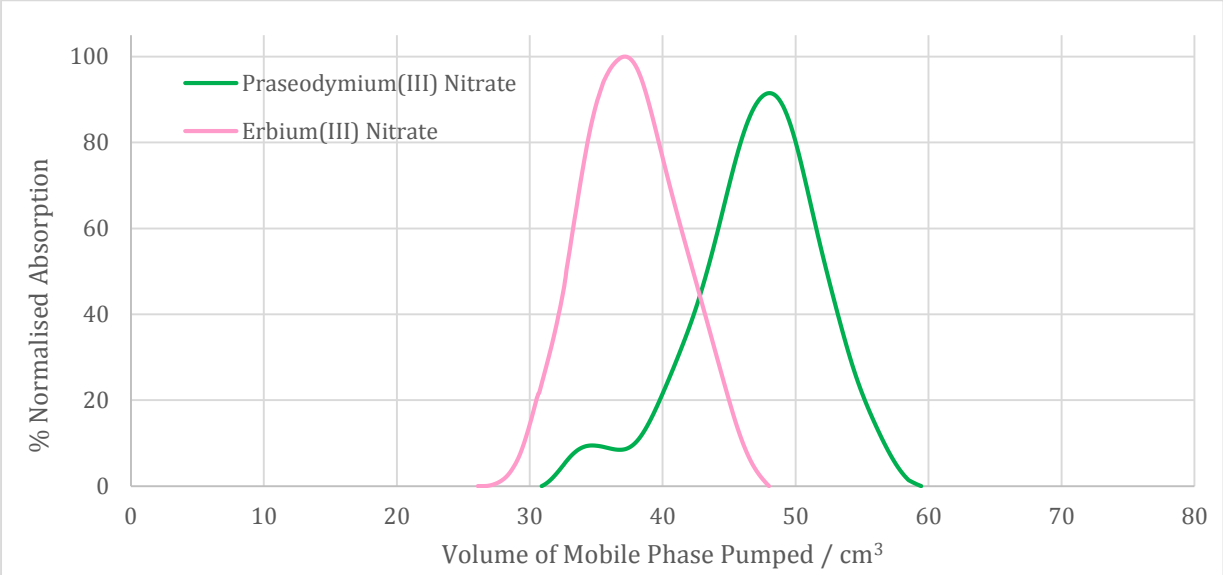

Figure C1 - Entry 18, Solvent System = C1, 3.0 cm^3 min^{-1}, 0.80g ($Pr(NO_3)_3.6(H_2O)$ + 0.80g $Er(NO_3)_3.5(H_2O)$.

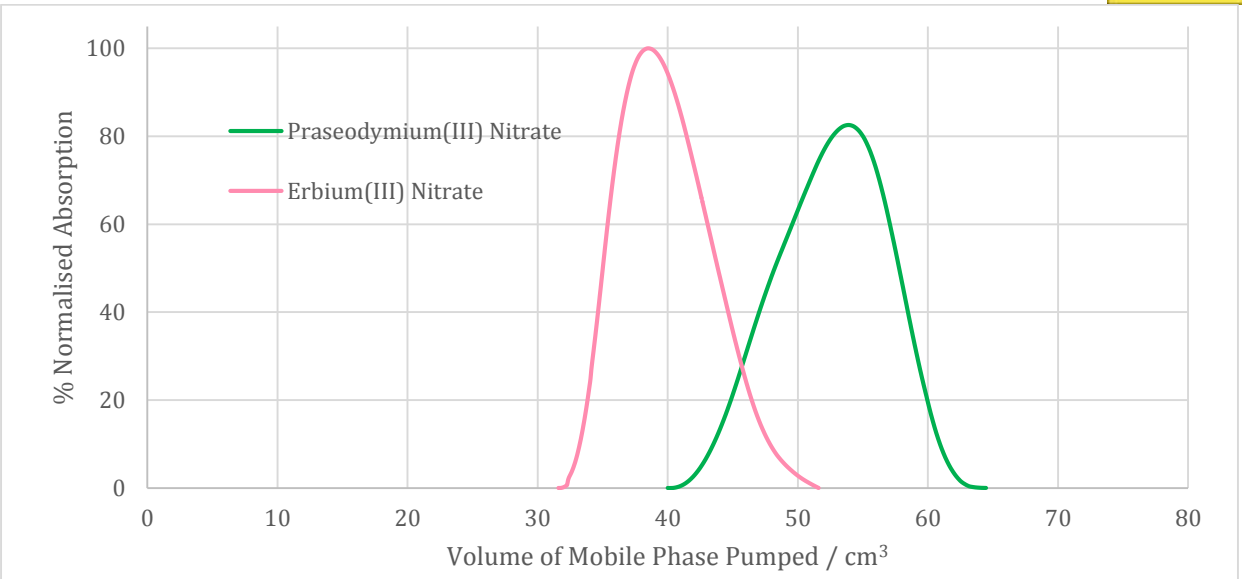

Figure C1 - Entry 19, Solvent System = C1, 4.0 cm^3 min^{-1}, 0.80g ($Pr(NO_3)_3.6(H_2O)$ + 0.80g $Er(NO_3)_3.5(H_2O)$.

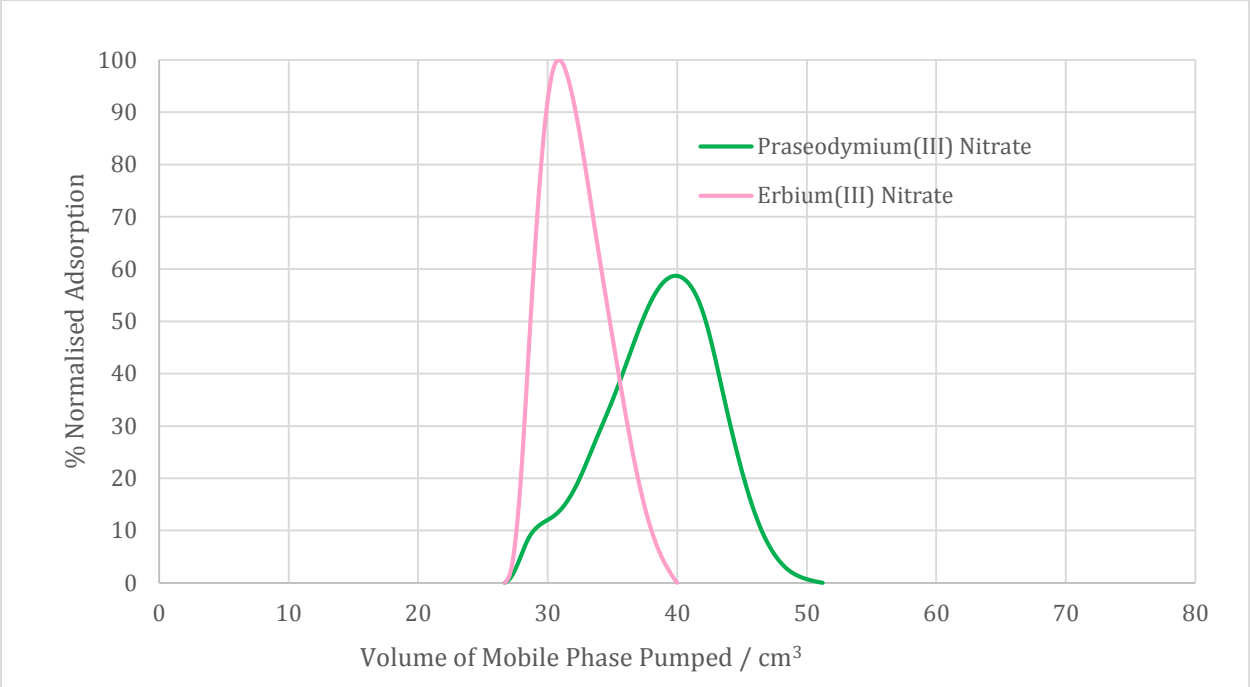

Figure C1 - Entry 20, Solvent System = C1, 2.0 cm^3 min^{-1}, 0.35g ($Pr(NO_3)_3.6(H_2O)$ + 0.35g $Er(NO_3)_3.5(H_2O)$.

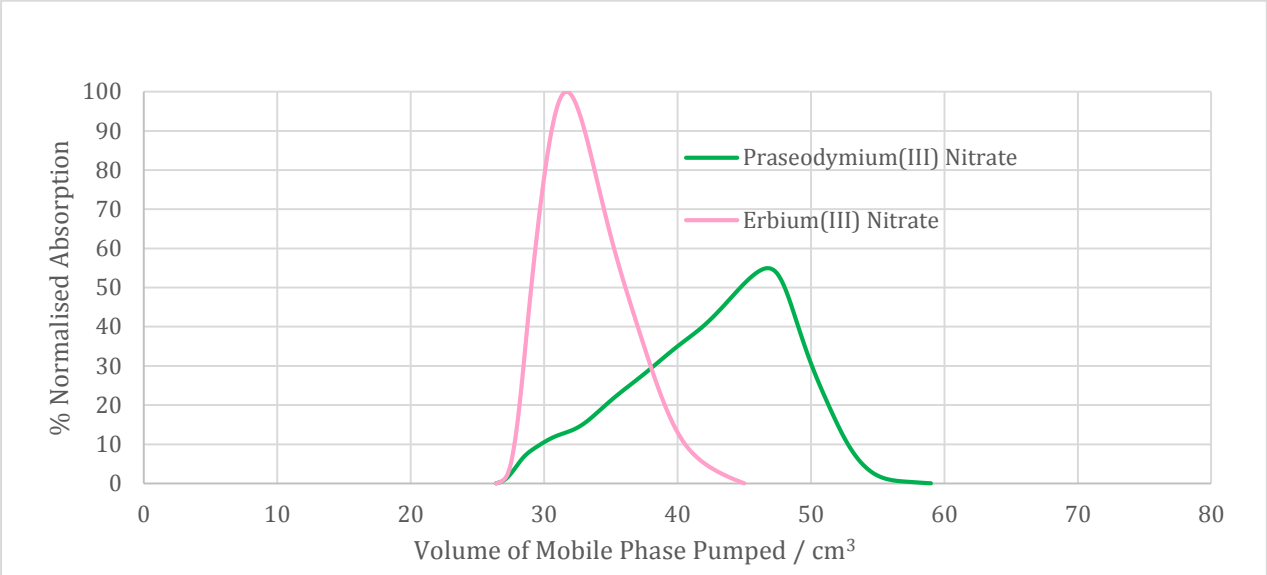

Figure C1 - Entry 21, Solvent System = C1, 2.0 cm^3 min^{-1}, 0.50g ($Pr(NO_3)_3.6(H_2O)$ + 0.50g $Er(NO_3)_3.5(H_2O)$.000

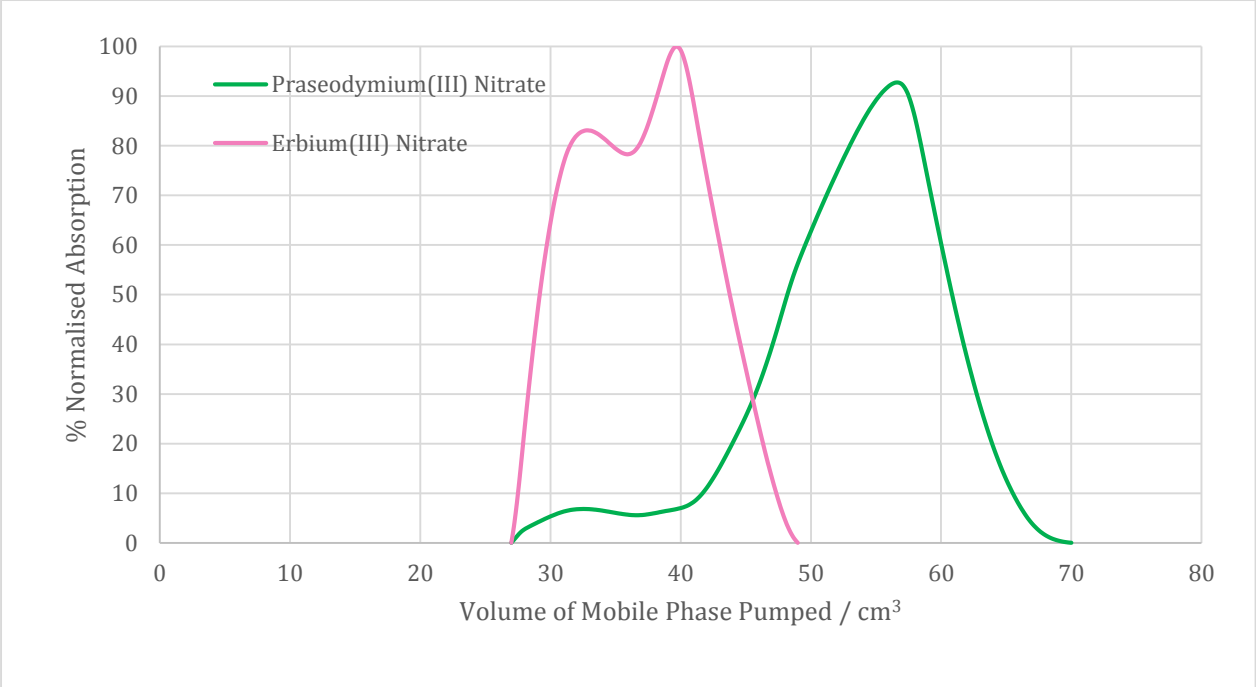

Figure C1 - Entry 22, Solvent System = C1, 2.0 cm^3 min^{-1}, 1.40g ($Pr(NO_3)_3.6(H_2O)$ + 1.40g $Er(NO_3)_3.5(H_2O)$.

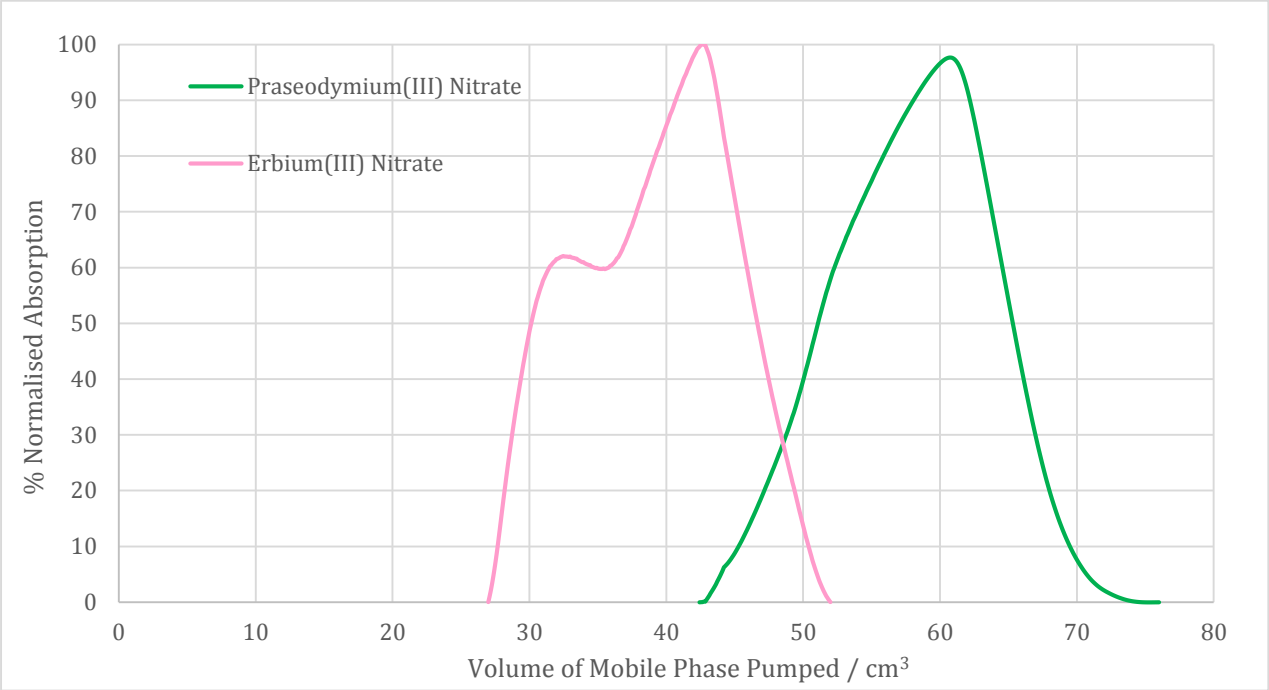

Figure C1 - Entry 23, Solvent System = C1, 2.0 cm^3 min^{-1}, 2.00g ($Pr(NO_3)_3.6(H_2O)$ + 2.00g $Er(NO_3)_3.5(H_2O)$.

C2 Chromatograms

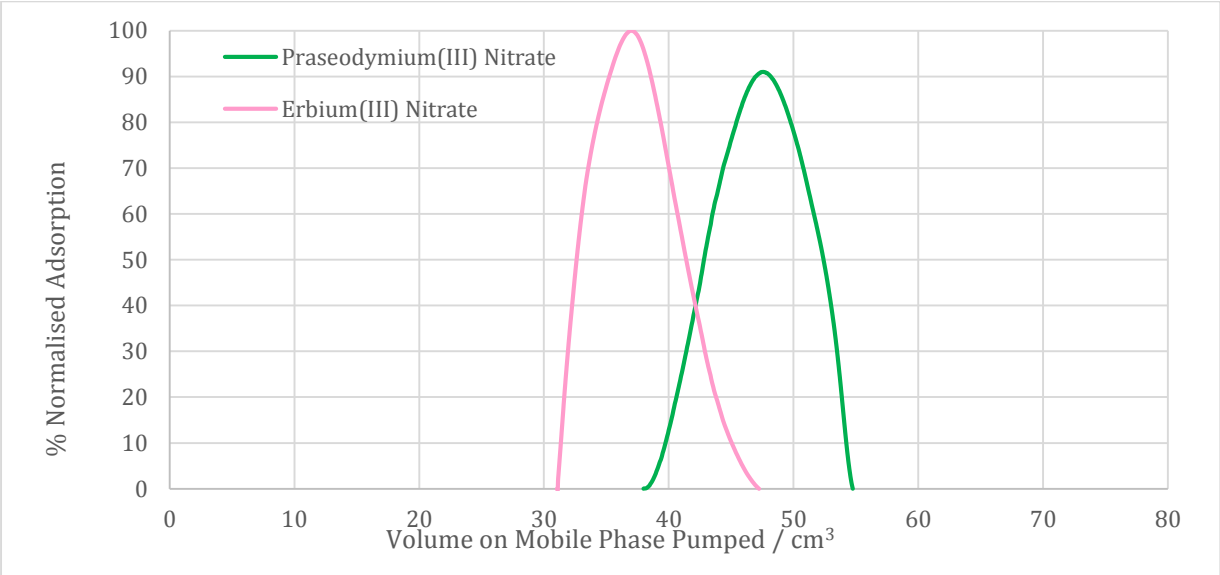

Figure C2 - Entry 24, Solvent System = C2, 1.5 cm^3 min^{-1}, 0.35g ($Pr(NO_3)_3.6(H_2O)$ + 0.35g $Er(NO_3)_3.5(H_2O)$.

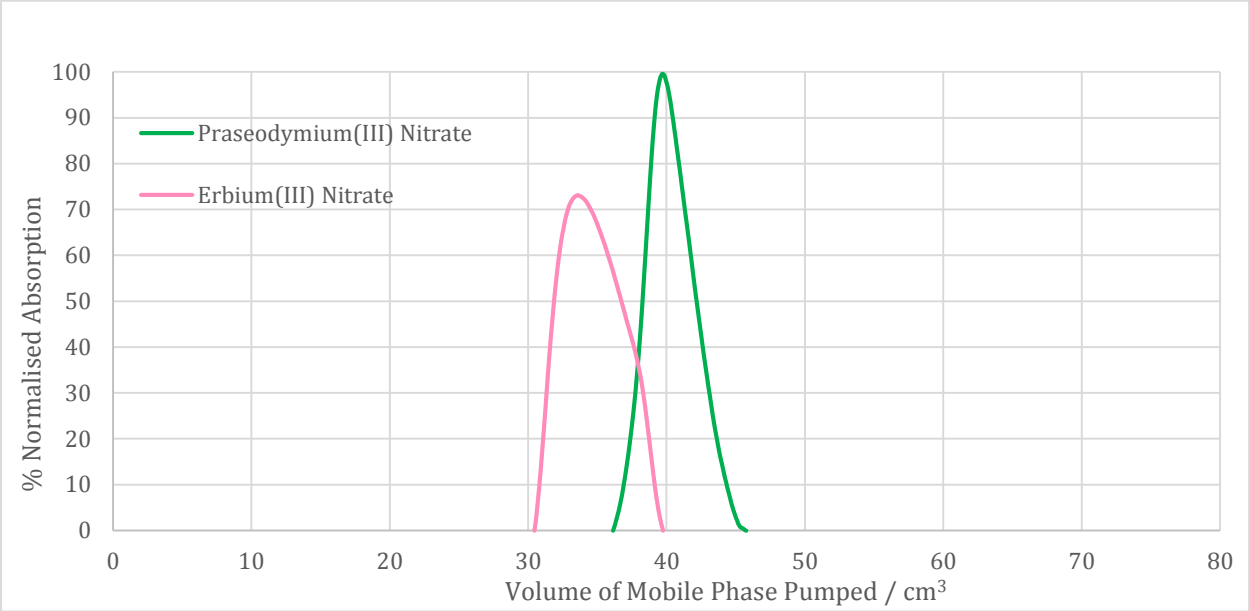

Figure C 2 - Entry 25, Solvent System = C2, 1.5 cm^3 min^{-1}, 0.50g $(Pr(NO_3)_3.6(H_2O)$ + 0.35g $Er(NO_3)_3.5(H_2O)$.

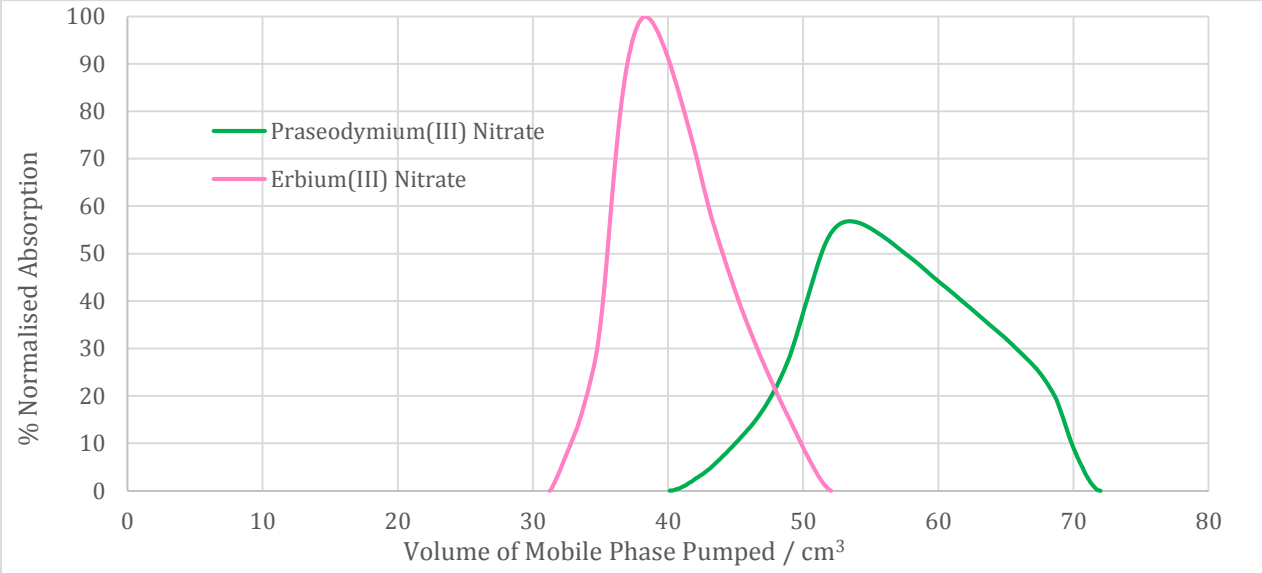

Figure C2 - Entry 26, Solvent System = C2, 1.5 cm^3 min^{-1}, 0.80g $(Pr(NO_3)_3.6(H_2O)$ + 0.80g $Er(NO_3)_3.5(H_2O)$.

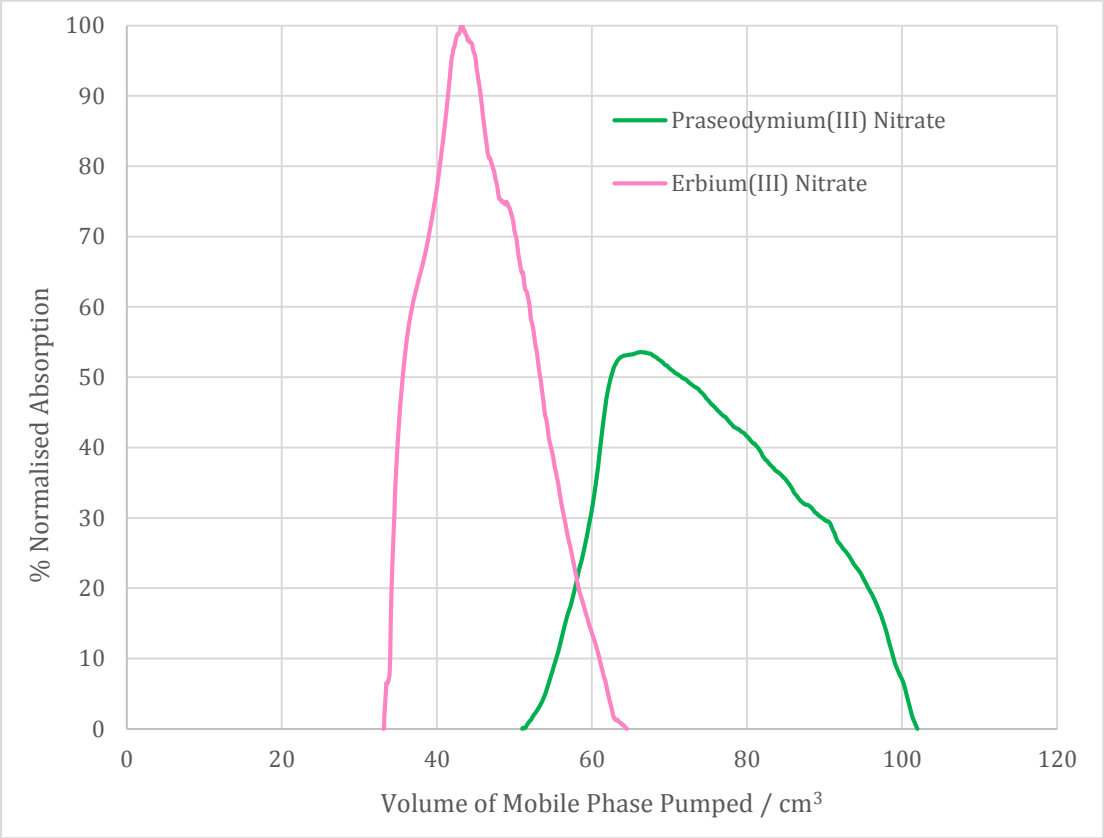

Figure C2 - Entry 27, Solvent System = C2, 1.5 cm^3 min^{-1}, 1.40g ($Pr(NO_3)_3.6(H_2O)$ + 1.40g $Er(NO_3)_3.5(H_2O)$.

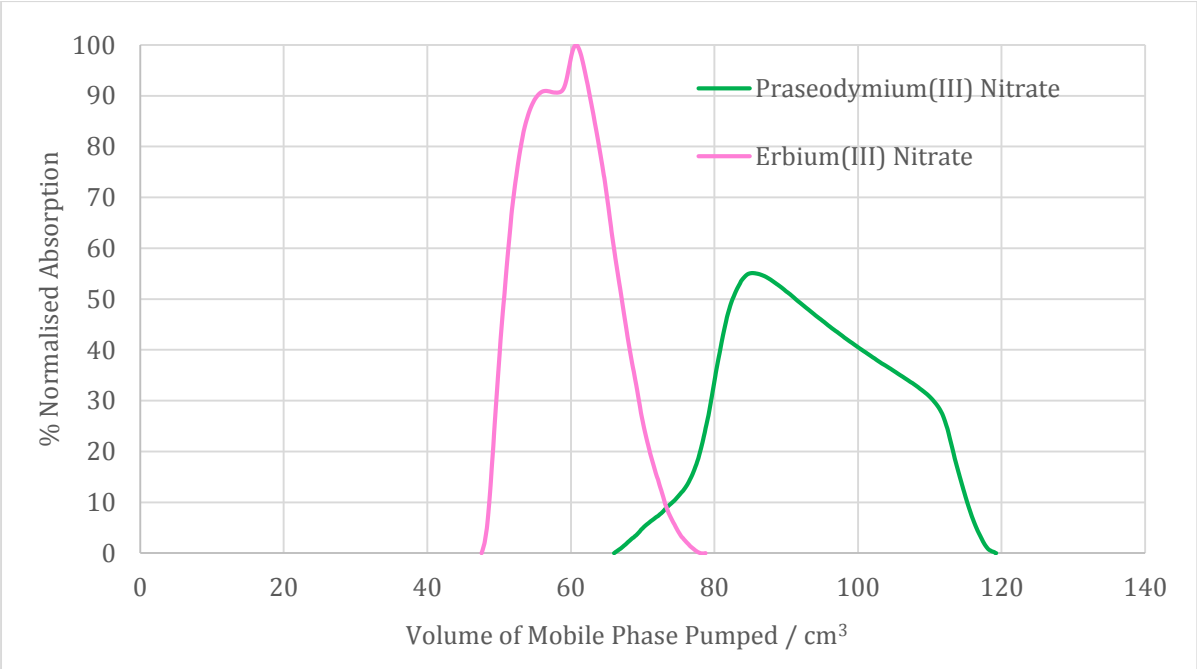

Figure C2 - Entry 28, Solvent System = C2, 1.5 cm^3 min^{-1}, 2.00g ($Pr(NO_3)_3.6(H_2O)$ + 2.00g $Er(NO_3)_3.5(H_2O)$.

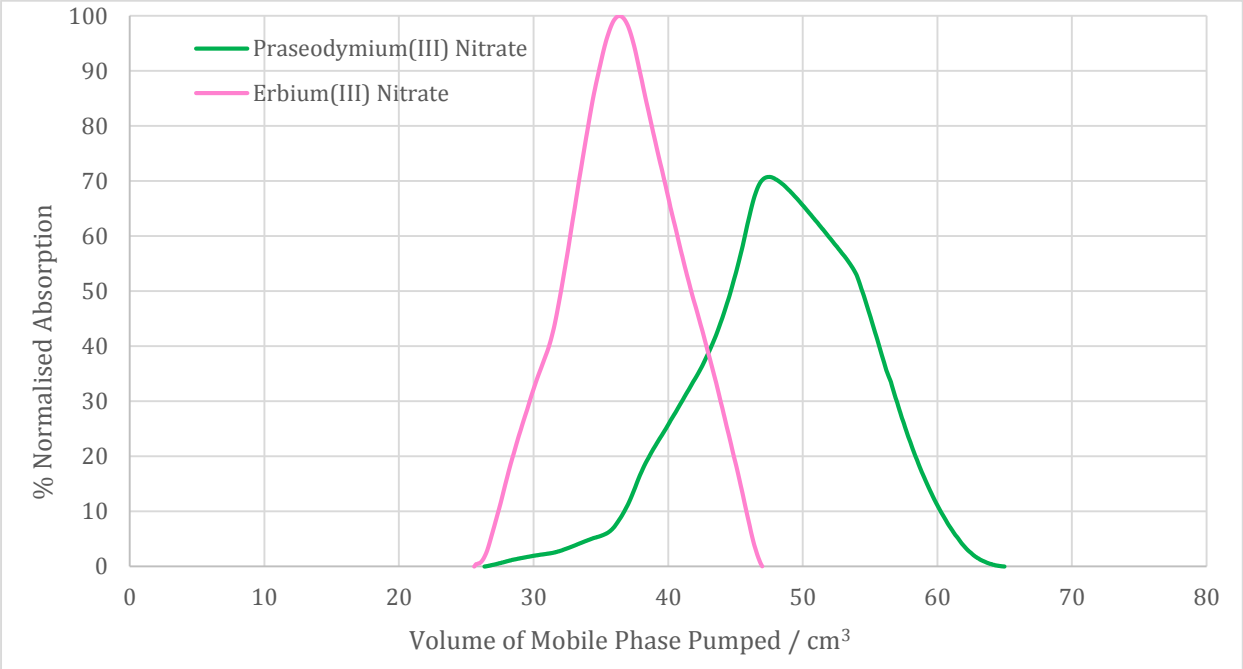

Figure C2 - Entry 29, Solvent System = C2, 0.5 cm^3 min^{-1}, 0.80g ($Pr(NO_3)_3.6(H_2O)$ + 0.80g $Er(NO_3)_3.5(H_2O)$.

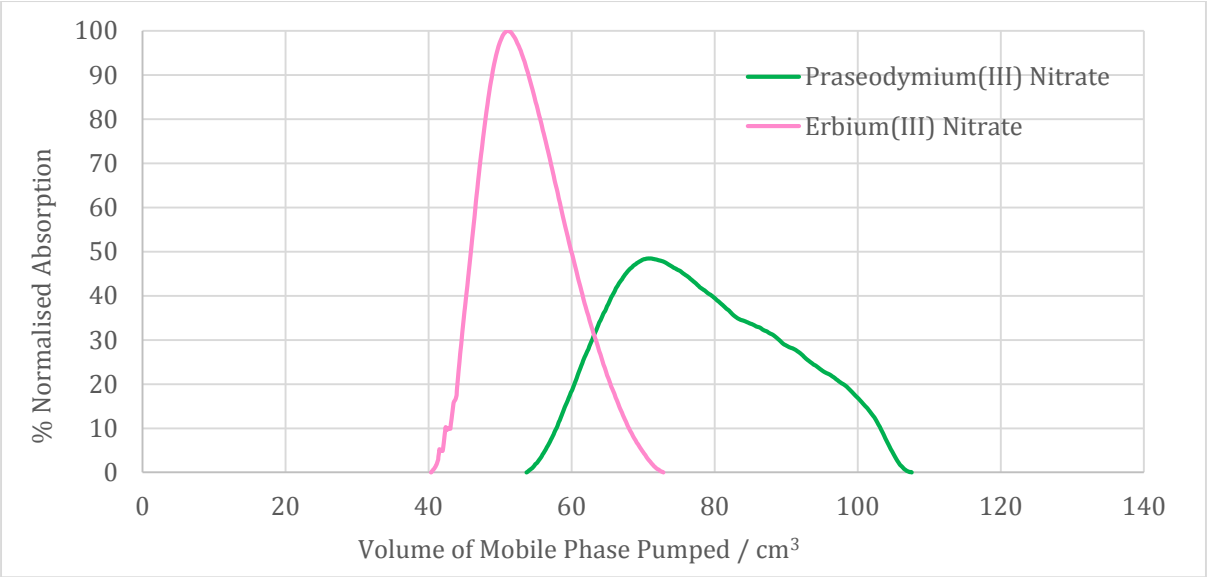

Figure C2 - Entry 30, Solvent System = C2, 1.0 cm^3 min^{-1}, 0.80g ($Pr(NO_3)_3.6(H_2O)$ + 0.80g $Er(NO_3)_3.5(H_2O)$.

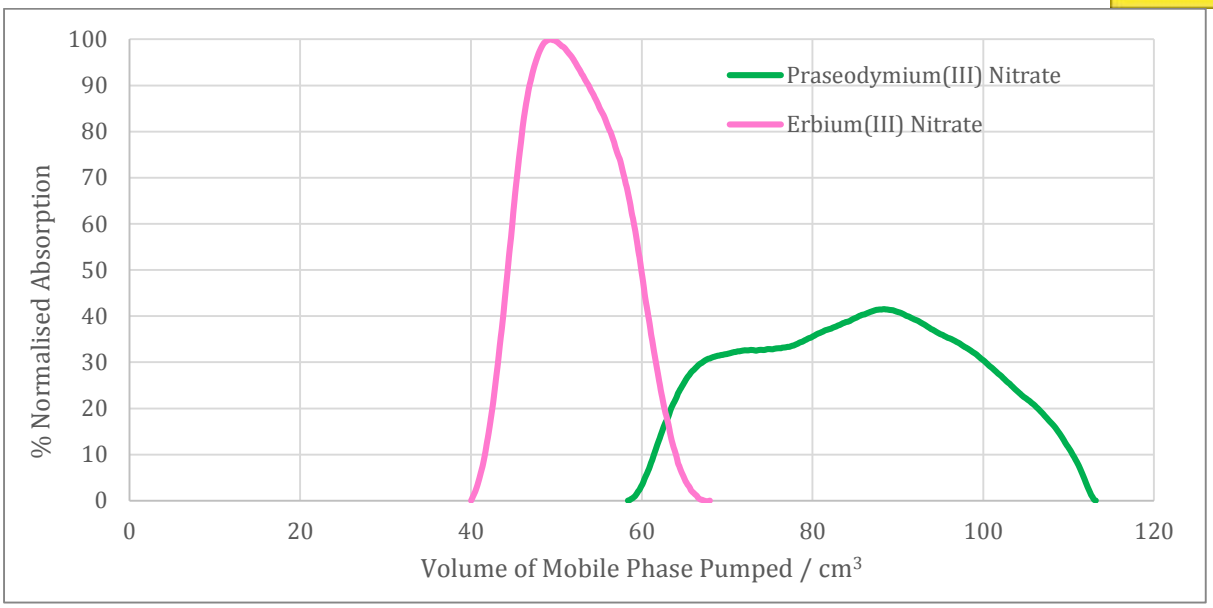

Figure C2 - Entry 31, Solvent System = C2, 2.0 cm^3 min^{-1}, 0.80g ($Pr(NO_3)_3.6(H_2O)$ + 0.80g $Er(NO_3)_3.5(H_2O)$.

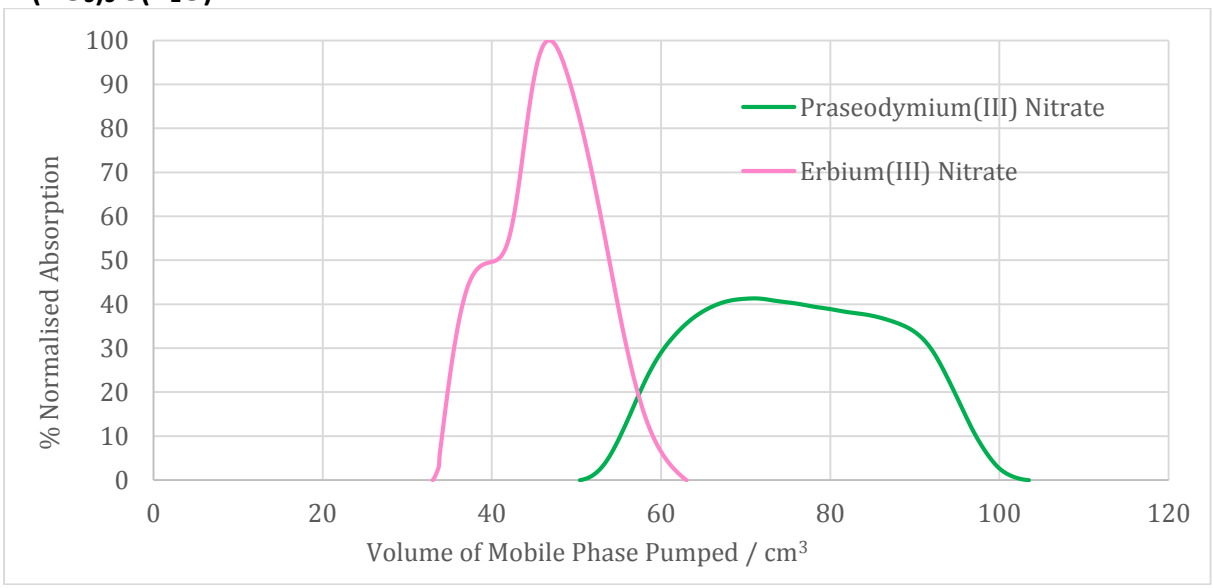

Figure C2 - Entry 32, Solvent System = C2, 3.0 cm^3 min^{-1}, 0.80g ($Pr(NO_3)_3.6(H_2O)$ + 0.80g $Er(NO_3)_3.5(H_2O)$.

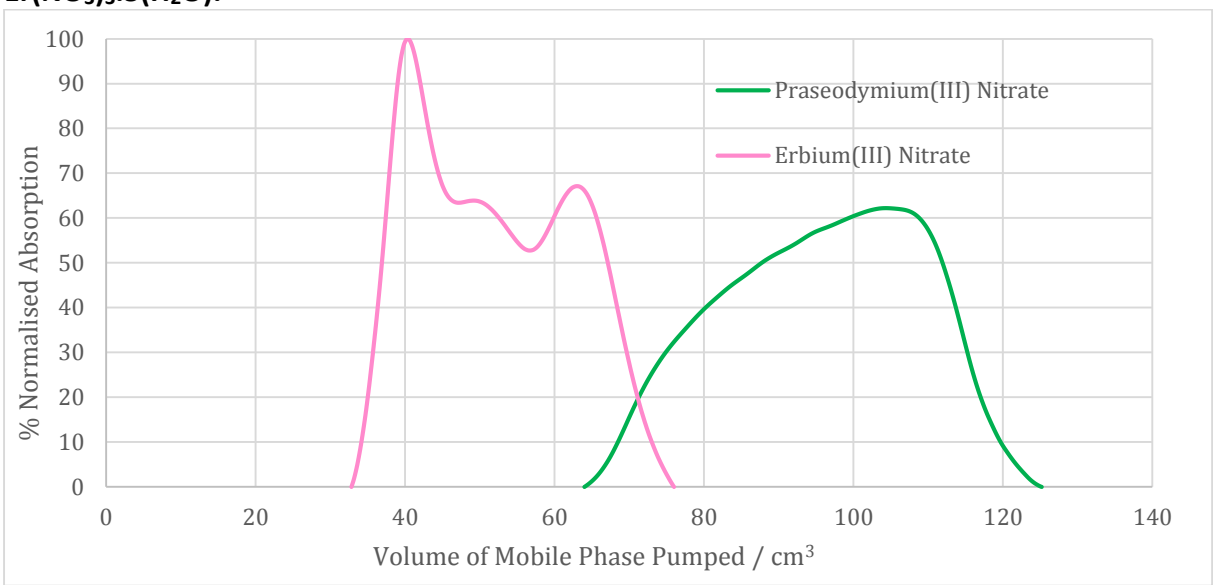

Figure C2 - Entry 33, Solvent System = C2, 4.0 cm^3 min^{-1}, 0.80g ($Pr(NO_3)_3.6(H_2O)$ + 0.80g $Er(NO_3)_3.5(H_2O)$.

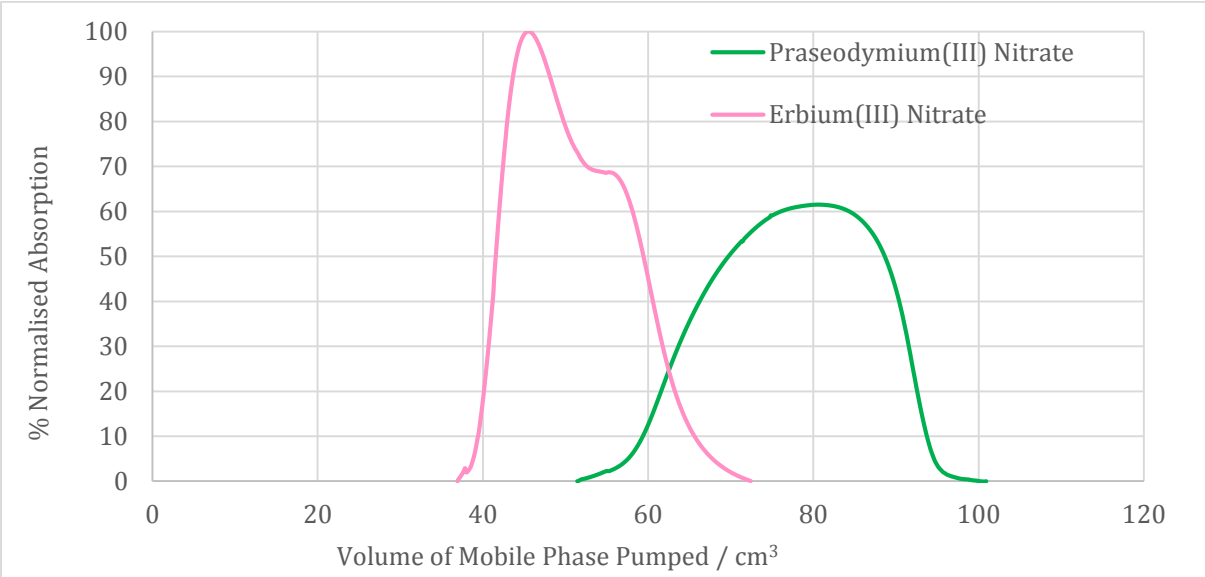

Figure C2 - Entry 34, Solvent System = C2, 5.0 cm^3 min^{-1}, 0.80g ($Pr(NO_3)_3.6(H_2O)$ + 0.80g $Er(NO_3)_3.5(H_2O)$.

QUILL Quarterly Report

November 2018 – January 2019

Name:	**Helene Raabjerg Eriksen**		
Supervisor(s):	Dr Nimal Gunaratne		
Position:	Chemical Research Apprentice		
Start date:	01.11.2018	Anticipated end date:	31.08.2019
Funding body:			

Reactive ionic liquid esters for perfume release in neutral water

Background

Our ionic liquids will be activated by the positive charge on the nitrogen atom on the cation.
We started out with a model study but we have later on attached perfume alcohols to the ionic liquid, in the hopes that we can utilise them as pro-fragrances for slow perfume release in water.
We ran kinetic runs, heating these compounds in D_2O solutions (identical concentrations) at 80°C in NMR tubes. These reactions were monitored by running NMRs at different time intervals to observe the release of product.

From the results, we can clearly see how the position of the side group effects the pace of the release of the product.

Right now, we are working on attaching several perfume alcohols to on ionic liquid and by during this hopefully we can create a perfume with different notes that are released at different periods.

Progress to date

Kinetic runs have been done on ionic liquids where new perfume alcohol citronellol was attached to the ester group, following the same kind of pattern as described in the previous report. The experiment was once again carried out in neat D_2O without acid, base or enzymes. Reactions were followed by NMRs and the results can be seen below.

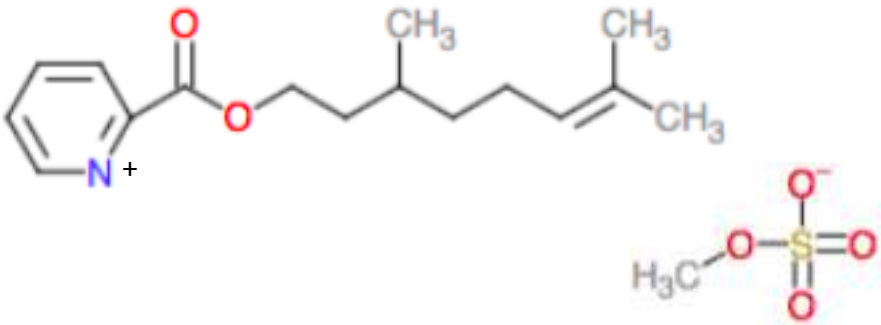

Molecular structure of 2PyCIT-MS. Showing how the citronellol molecule is attached to the pyridine-ring in the second position from the nitrogen atom.

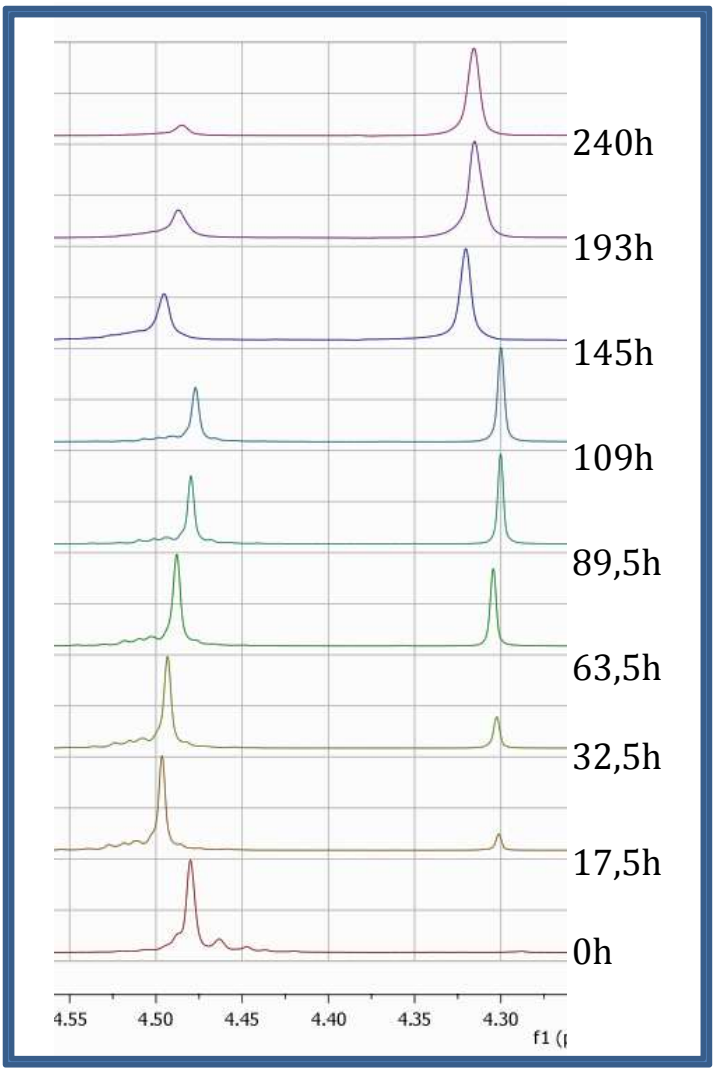

2PyCit-MS
Here are the stacked NMR spectra of 2PyCit-MS. The peaks on the left are the starting material and the peaks on the right are the product or the released perfume.

Figure 1 - Results on the hydrolysis of perfume tagged ionic liquid ester at 80°C in neutral water.

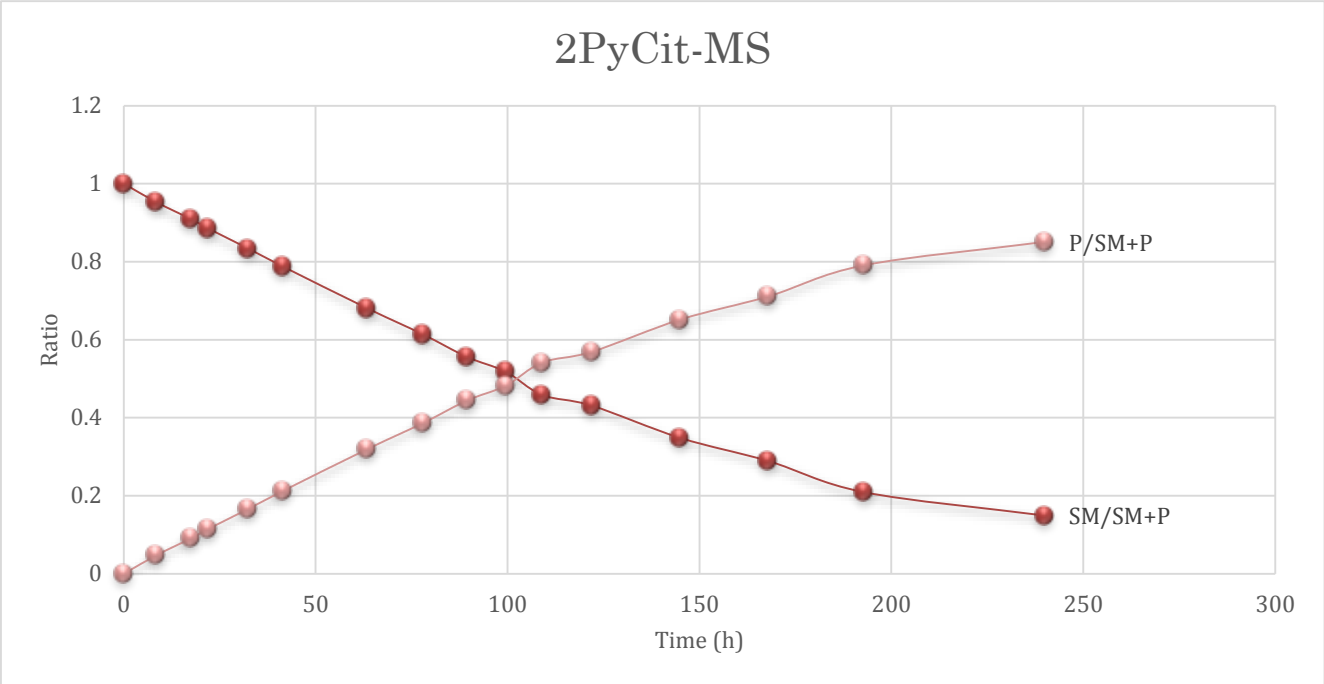

***Figure 2* - Graph showing the progression of the release of perfume tagged to ionic liquid ester.**
NB: P/SM+P = Product/(Starting Material + Product) and SM/SM+P = Starting Material/(Starting Material + Product)

This does not curve as much as anticipated, it might have something to do with the size of the molecule. The slower the release of the product or written differently: the harder it is to hydrolyse, the more gradual the curve increase.

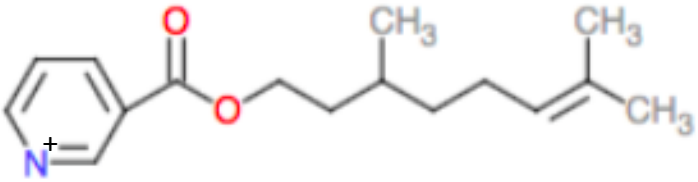

Molecular structure of 3PyCIT-MS. Showing how the citronellol molecule is attached to the pyridine-ring in the third position from the nitrogen atom.

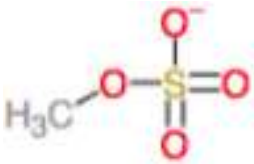

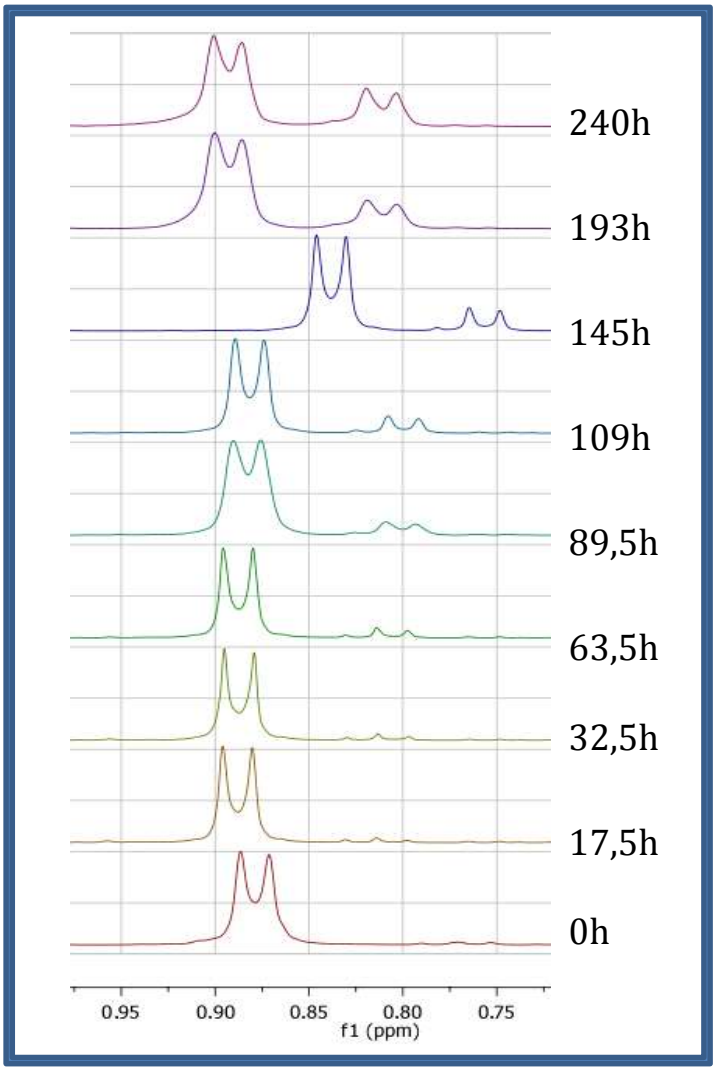

3PyCit-MS
Here are the stacked NMR spectra of 3PyCit-MS. The peaks on the left are the starting material and the peaks on the right are the product or the released perfume.

Figure 3 - Results on the hydrolysis of perfume tagged ionic liquid ester at 80°C in neutral water.

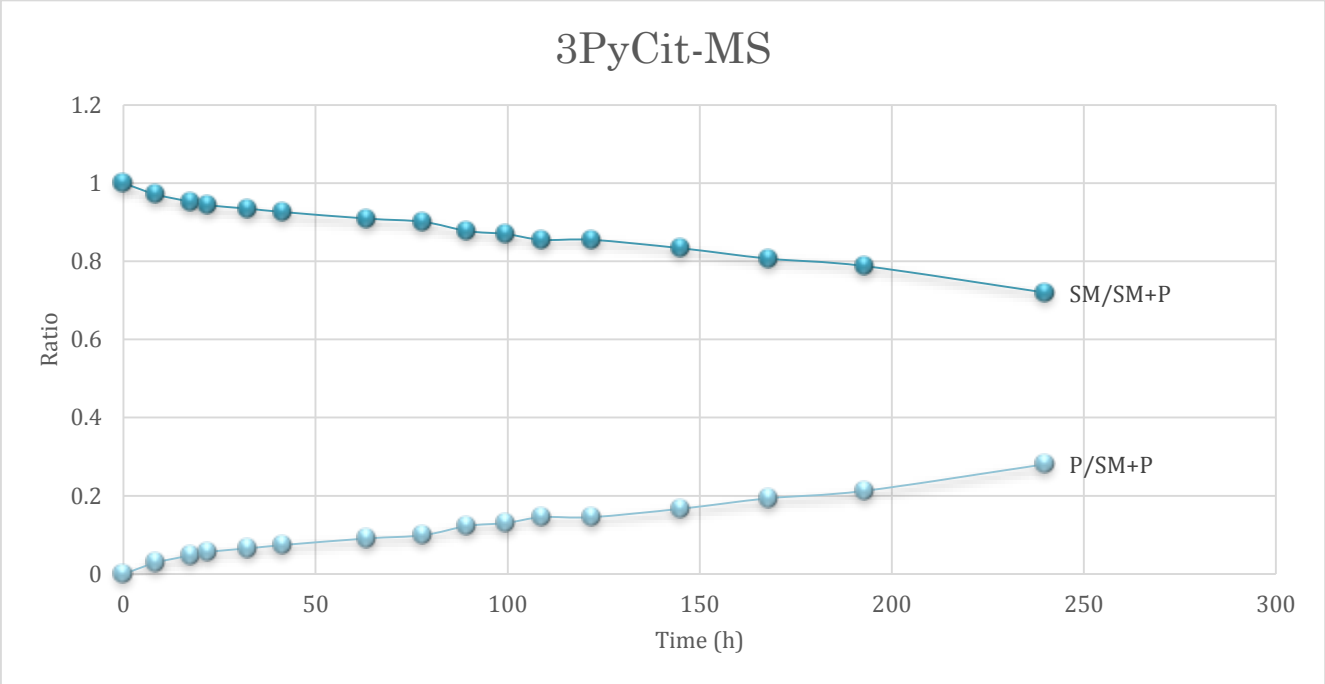

Figure 4 **- Graph showing the progression of the release of perfume tagged to ionic liquid ester.**
NB: P/SM+P = Product/(Starting Material + Product) and SM/SM+P = Starting Material/(Starting Material + Product)

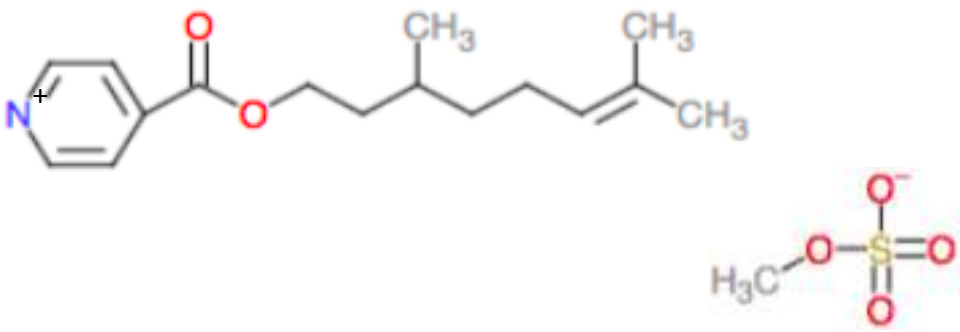

Molecular structure of 4PyCIT-MS. Showing how the citronellol molecule is attached to the pyridine-ring in the fourth position from the nitrogen atom.

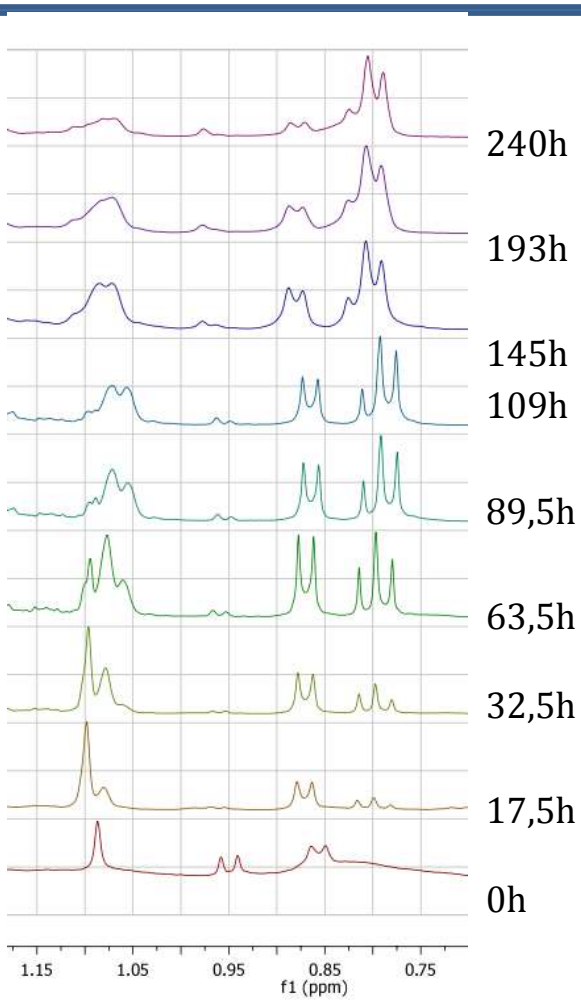

4PyCit-MS

Here are the stacked NMR spectra of 4PyCit-MS. The peaks on the left are the starting material and the peaks on the right are the product or the released perfume.

As seen in the graph below, it is not the smoothest, therefore we will try and integrate different peaks, see if we get a different outcome, to make sure we get the correct results and work on the right peaks.

The baseline on this does not look well either.

Figure 5 - Results on the hydrolysis of perfume tagged ionic liquid ester at 80°C in neutral water.

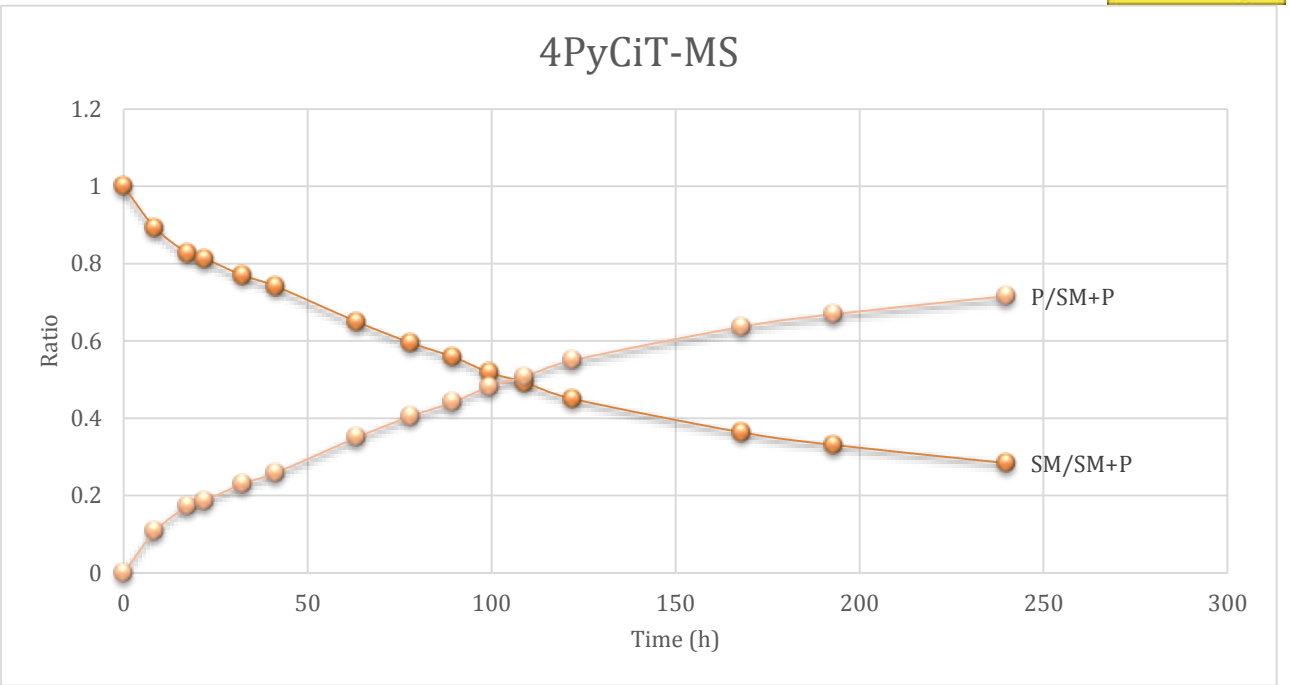

***Figure 6* - Graph showing the progression of the release of perfume tagged to ionic liquid ester.**
NB: P/SM+P = Product/(Starting Material + Product) and SM/SM+P = Starting Material/(Starting Material + Product)

These are the perfume alcohols we are currently working with:

Majantol – Currently doing kinetic runs

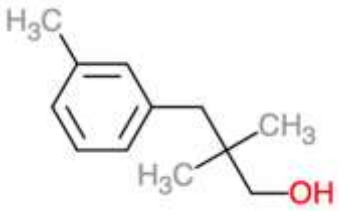

Geraniol –

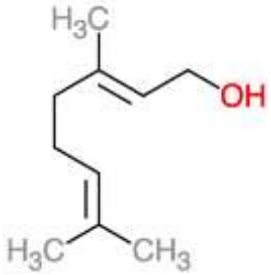

Conclusions and future work

Alternated methods were also explored to improve the yields. For example, picolinic acid + thionyl chloride + any perfume alcohol to form the ester.

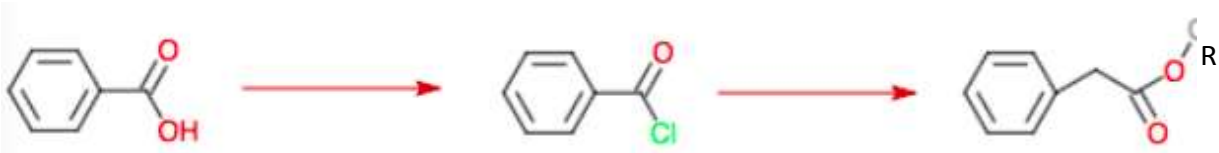

The reaction monitoring process is still ongoing. Similar compounds will be made with other perfume alcohols and kinetic study will be undertaken.
We also plan to run further analysis including TGA, MS and possibly FTIR among other analysis.

QUILL Quarterly Report

February – April 2019

Name:	**Martin Gillespie**		
Supervisor(s):	Prof Peter Nockemann, Dr Małgorzata Swadźba-Kwaśny and Dr Steven Glover		
Position:	PhD student		
Start date:	1/10/18	Anticipated end date:	30/09/21
Funding body:	Dfte N.I.		

Hybrid Electrolytes for Solid-State Batteries in Electric Vehicles

Background

Petrol and diesel engines in vehicles are likely to soon become a thing of the past. Declining amounts of fossil fuels, rising atmospheric carbon dioxide levels, worsening air quality in cities and out of control climate change demand significant changes to global human behaviour. Transitioning from fossil fuel powered transport to electric vehicles (EVs) represents a huge step in humanity taking responsibility for caused environmental deterioration and a striving to correct past poor practices.

Electric vehicles provide transport without any of the noxious exhaust emissions from traditional combustion engines. Presently the build-up of combustion fumes in traffic dense areas causes a localised reduction in life quality, an increase in respiratory diseases, numerous deaths each year as well as adding to already elevated greenhouse gas levels globally. Much of the electricity needed to charge EVs will presently be generated from burning fossil fuels at existing power plants but this energy generation can be over ten times more efficient than within a combustion engine and of course electricity for EVs can be generated from renewable energy sources resulting in very little or no detrimental effects to the environment. Due to having vastly less quantities of individual moving parts when compared to combustion engines EVs require significantly fewer the consumable components. Noise pollution is also reduced by using EVs,

The electrolyte is a vital component in secondary batteries for EVs. A poor-quality electrolyte results in a poor-quality EV. The electrolyte facilitates the transport of metal cations between electrodes during charge/discharge cycles. A highly functioning electrolyte must display some vital characteristics, these are mentioned below and the presence of these qualities within electrolytes will be the focus of this work.

Objective of this work

To improve on the current state-of-the-art electrolytes with respect to ionic conductivity, ionic transference number, electrode compatibility, stability (electrochemical, chemical and thermal), recyclability, integrity under stress and environmental impact from non-intentional cell rupture. The goal is to optimise an electrolyte formulation which can be scaled up and used directly in EVs and possibly in other energy storage entities.

Progress to date

Straight chain oligoethers which contain electron donating ether oxygen atoms have been shown to have much potential when used within a solvate ionic liquid electrolyte system. The glyme

molecules when coordinated around an alkali metal ion act as cation shuttles between electrodes during charge/discharge cycles. Coordination around the Lewis acidic alkali metal ion lowers the highest occupied molecular orbital energy level. This reduction in energy level greatly increases both the thermal and chemical stabilities of the electrolyte. Competitive coordination of the metal salt anion affects ionicity and ionic conductance efficiency. Structural isomers of straight chain oligethers have not yet been investigated as part of a solvate ionic liquid electrolyte. 1,2,3-Trimethoxypropane is a structural isomer of diglyme. Both contain 3 ether oxygen atoms for metal ion coordination. Glycerol can be directly methylated to 1,2,3-trimethoxypropane. This synthesis was recently attempted but GC-MS analysis revealed only partial methylation and that glycerol with increased purity should be used in synthesis. The products of this experiment are shown below.

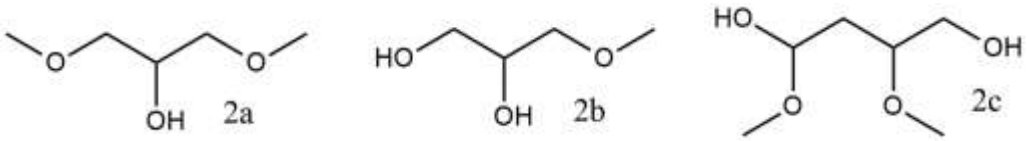

These products are not suitable for use for electrolyte synthesis or further investigation. As a result the synthesis will be redone using higher quality starting materials. When pure 1,2,3-trimethoxypropane is obtained electrolyte systems will be formulated and tested for potential as electrolytes.

Conclusions and future work.

Highly pure oligethers must be obtained. Once this is achieved their use in metal ion batteries will be assessed. 1,2,3-Trimethoxypropane contains 3 electron donating oxygen atoms, structural isomers of longer glymes containing more electron donating groups will be synthesised and purified for testing.

QUILL Quarterly Report

February – April 2019

Name:	**Oliver Hammond**		
Supervisor(s):	Dr Marijana Blesic		
Position:	Postdoctoral Research Fellow		
Start date:	1/11/18	Anticipated end date:	31/10/19
Funding body:	EPSRC		

Exploring the potential of zwitterionic salts

Background

One of the biggest problems encountered at any interface with biological substances is the undesired and uncontrolled adsorption of protein, which is known as fouling.[1] The properties of zwitterionic materials, principally their superhydrophilicity, makes them ideally-suited to be used as interfacial coatings to form ultralow-fouling surfaces which selectively resist the formation of these protein coatings.[2] Zwitterionic materials have accordingly found myriad applications where this is advantageous such as hydrogels for cell culture, and protein-resistant coatings for nanoparticles and biomedical devices such as catheters, notwithstanding their widespread application in contact lenses, and even as zwitterionic liquids.[3] In all of these applications the unique properties of zwitterions means that they are far more effective than traditional non-zwitterionic polymers such as PEG.[4] As well as the selective resistance of zwitterionic surfaces towards nonspecific aggregation of proteins, it is possible to design preferable interactions towards certain substrates, creating a surface which repels all but the object of desire, which have been dubbed 'romantic surfaces'.[5]

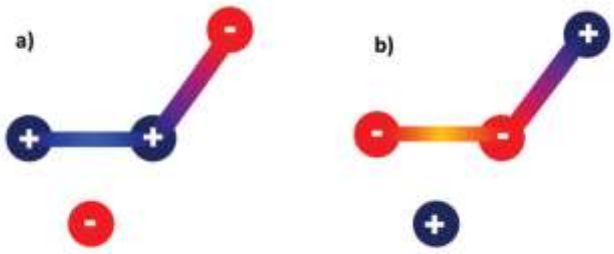

Figure 1 - Cartoon examples of the structure of 'Zwitterionic Salts' (ZWS). A ZWS is formed when either the cation (a) or anion (b) of a binary salt contains an odd number of formal charges, leaving one unit of charge effectively unpaired. This makes them distinct from traditional salts, zwitterions, and polyelectrolytes.

This work is concerned with the so-called 'Zwitterionic Salts' (ZWS), which are a category of asymmetrically-charged compounds containing a formal cation and anion, where one of these units has an embedded zwitterion, shown in Figure 1.[6] As a relatively recent discovery, the scope,

properties and potential applications of ZWS has not been explored.[7] This project therefore integrates several goals with the overall aim of developing further the fundamental understanding of ZWS and establishing their potential for future applications. Firstly, it is intended to synthesise some novel zwitterionic materials, and expand the current library of known compounds to further understand structure-property relationships. Then, the physical properties of the synthesised ZWS will be measured, with emphasis on solution-phase interactions. This analysis will primarily focus on interpretation of neutron diffraction data using atomistic modelling, for alkyl-diammonium-bromide-sulfonate ZWS and novel dizwitterionic bolaforms (see Figure 2) with different alkyl spacer lengths, giving insight into properties and interactions of these different zwitterionic species with biomolecules. These advanced measurement techniques will be complemented by measurements of solution physical properties (ie. viscosity, surface tension and excess molar volume measurements) and *ab initio* computational chemistry methods. Following this, methodology will be developed for the preparation of new surfaces coated with ZWS-based materials, and the hypothesis that ZWS will form effective protein-resistant coatings will be tested using techniques such as AFM and QCM.

Objectives of this work

- Devise preparations for new zwitterionic materials and determine their bulk solution properties, particularly ZW-water interactions (ie. H-bonding), with neutron scattering and modelling techniques and measurements of physical properties and phase behaviour.
- Develop methodology for ZWS-coated surfaces to assess whether more efficient protein-resistant surfaces can be prepared, for potential applications in biomedical devices or antifouling marine coatings.

Progress to date

The first stage of this work has been to synthesise various zwitterionic salts and zwitterionic compounds for neutron scattering measurements at the STFC ISIS Neutron & Muon Facility, where a 5-day beamtime was awarded to this project on the SANDALS diffractometer. Two experiments were planned. Firstly, a series of bolaform dizwitterionic species were synthesised by symmetric dialkylation of *N*,*N*,*N*',*N*'-tetramethylethylenediamine (TMEDA) with 1,3-propanesultone, and analogues of TMEDA with higher alkyl chain lengths in the centre of the molecule (n = 2, 3, 6; named 'DSZ2', 'DSZ3' and 'DSZ6' hereafter); the structure of these zwitterionic species is shown in Figure 2. The hypothesis of this study was that neutron scattering would provide structural understanding of the structure-property relationships observed for the different molecules, which presumably arise due to differences in hydration. The zwitterions were dissolved in water, D_2O, and mixtures thereof, and measured. While these salts are not zwitterionic salts, per se, they remain of fundamental interest and their chemical symmetry makes them more simple analogues for studies of hydration and alkyl chain length effects.

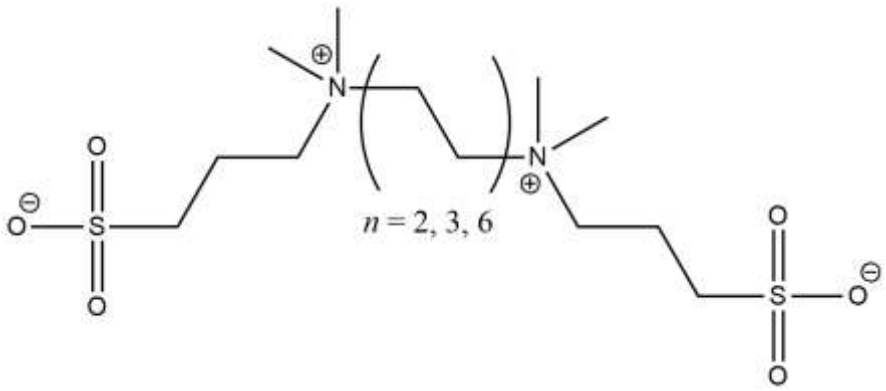

Figure 2 - Structure of the bolaform dizwitterionic species synthesised for neutron scattering measurements to take place in March. The synthesis is a diquaternisation of either TMEDA, TMPDA or TMHDA using 1,3-propanesultone.

The second experiment at ISIS was designed to understand the interactions between zwitterions and zwitterionic salts with hydrophobes, as these species have been found to have significant salting-in/out-ability, presumably due to strong hydration of the zwitterionic species and further ion-specific effects and interactions. To do this, then, protonated and deuterated versions of the zwitterionic salt 'C_2-NC_2N-C_3SO_3' were prepared by first alkylating *N*,*N*,*N*',*N*'-tetramethylethylenediamine (TMEDA) with (d_5-)bromoethane in a 1:1 ratio, and then adding a sulfonate group to the isolated and purified product using 1,3-propanesultone. Additionally, the 'SO_3C_3-NC_2N-C_3SO_3' bolaform zwitterion was prepared for these experiments. These zwitterionic compounds were used to prepare solutions in a 1:30 ZW:water ratio, and protonated and/or deuterated phenol were added in a 1:12.2 ratio of phenol:water, and the solutions measured.

Work was then done to fit these models and understand the structural information presented by the neutron data. This is achieved by using Empirical Potential Structure Refinement (EPSR) modelling, which is a Reverse Monte Carlo-derived model which fits a classically-parameterised atomistic simulation to the experimental scattering data.[8] Models were built from the ground up using OPLS-AA parameters derived from work by Jorgensen and Canongia Lopes, respectively for generic compounds, ionic liquid-type materials and for substituted benzenes.[9–11] Initially, the phenol molecules were found to be too flexible and were strengthened with rigid dihedral constraints. The models for the DSZn series of bolaform zwitterionic species fits to the data well, as shown by the close match between scattering data (markers) and model (lines) in Figure 3. Following this, we have begun further analysis of these models to extract structural characterisation such as partial radial distribution functions (pRDFs) and spatial density functions (SDFs). Similarly, Figure 4 shows expanded plots of the fits and data for the zwitterionic salts and double-zwitterions mixed with phenol. In this case the model is slightly more overstructured, as shown by exaggerated peak intensities which are due to the more rigid constraints on the flexibility of phenol. In both cases analysis is progressing well.

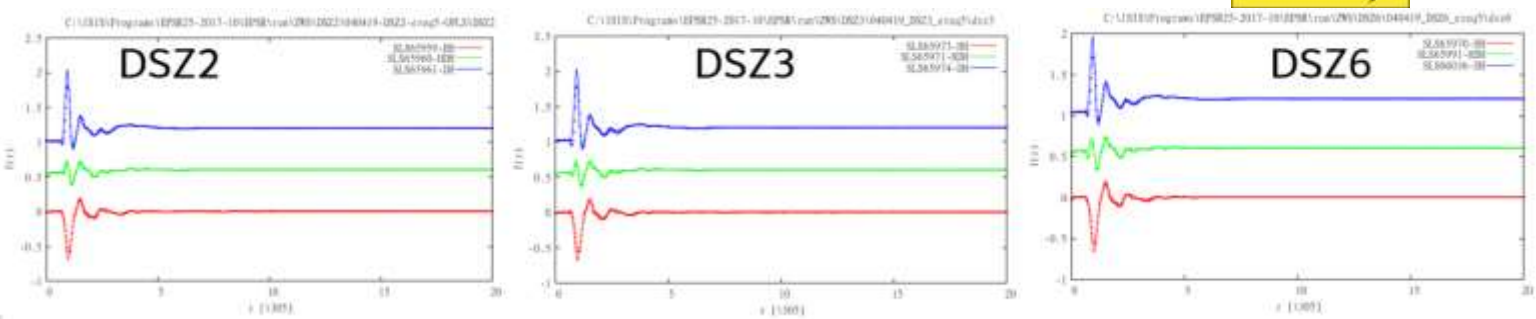

Figure 3 - Real (R-) space neutron scattering data (markers) and EPSR model fits (lines) made using improved potentials for the double-sulfonate zwitterion/water mixtures.

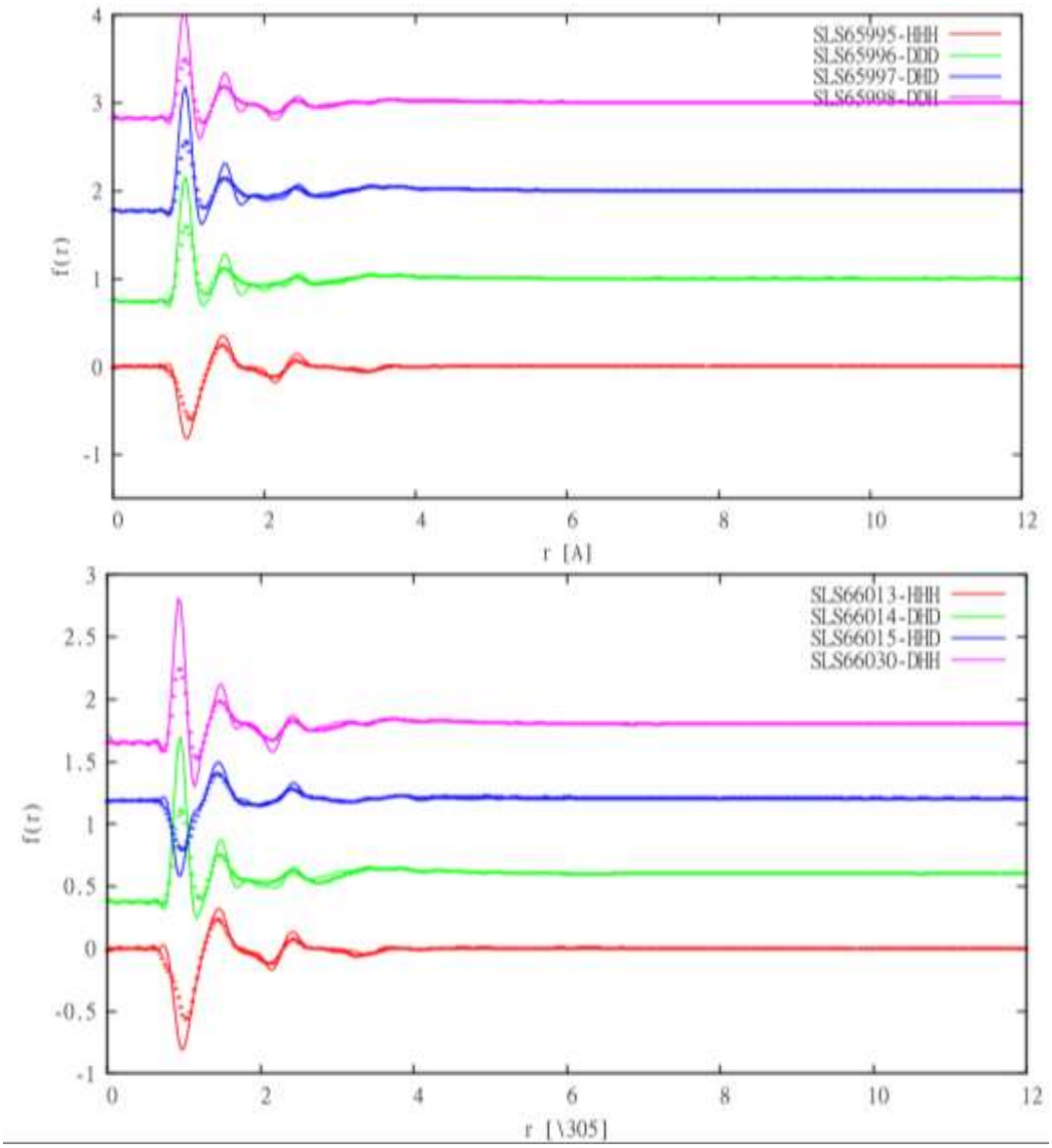

Figure 4 - Enlarged real (R-) space neutron scattering data (markers) and EPSR model fits (lines) made using improved potential for solutions of (top) the zwitterionic salt 'C_2-NC_2N-C_3SO_3' mixed with phenol and (bottom) the 'SO_3C_3-NC_2N-C_3SO_3' bolaform zwitterion mixed with phenol.

In addition to neutron scattering analysis, we have been measuring the physicochemical properties of zwitterionic salt solutions to better understand their solvation and interaction characteristics through bulk phenomena. We have been measuring the density and viscosity of aqueous solutions

of zwitterions using a densitometer, and capillary and rolling ball viscometers. We have also been measuring the effect of synthesised zwitterions on the critical micelle concentration of common surfactants, to determine salting-out/salting-in effects and specific ion interactions with surfactant headgroups and counterions. Example viscosity data taken using the rolling ball instrument is shown in Figure 5. The viscosity of a dilute aqueous solution provides a bulk indication of the sum of molecular-scale effects such as hydrodynamics (ie. size and shape of ions), structure (solute-solute and solvent-solute interactions), and Coulombic forces (ie. long-range Debye-Hückel forces). It was hypothesised, simply, that the most highly hydrated compounds should exhibit high viscosity, and zwitterions are known to exhibit strong local hydration and 'superhydrophilic' character.[12] Therefore, it is interesting to confirm that a small simple synthesized zwitterion 'ZW' increases the viscosity of water in the dilute regime significantly more than the simple salt, tetramethylammonium bromide. The synthesised dicationic ammonium dibromide species 'DC' has a slightly greater effect than the zwitterion, being two units of charge but each less well-hydrated than a single zwitterion. The strongest effect is seen for the double-zwitterion, followed by the 'C2S' zwitterionic salt, which is effectively a fused zwitterion and ammonium bromide group, and falls slightly below the double-zwitterion and slightly above the double-cation, showing a synergistic effect and the expected ordering of kosmotropicity. Finally, in addition to these measurements and synthesis, further synthetic experiments have been carried out to determine the viability of different approaches towards new ZWS, as it has been found that selectivity can be difficult to achieve. It was found that, with enough purification, the reaction can be run in the opposite order, by first forming a zwitterion with the addition of 1,3-propanesultone, enabling a simpler route towards novel ZWS materials.

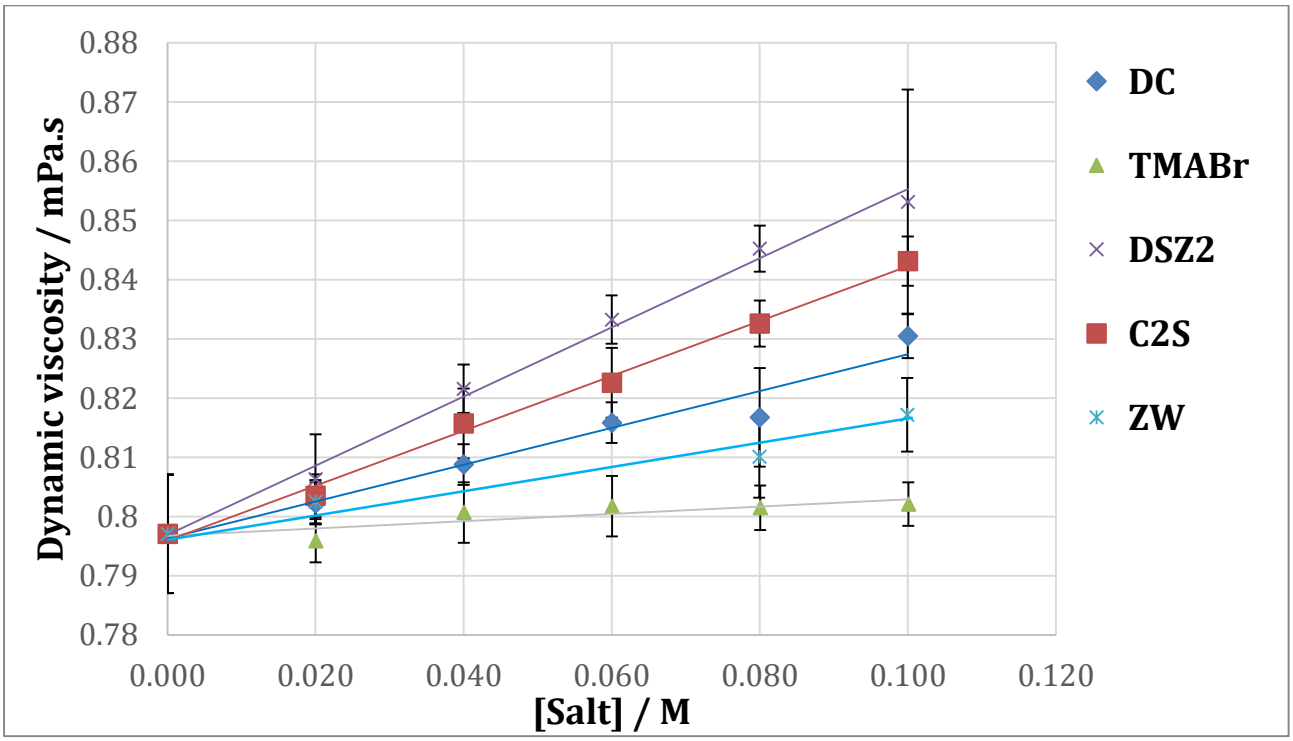

Figure 5 - Viscosity of dilute aqueous solutions of zwitterion 'ZW', zwitterionic salt 'C2S', double-zwitterion 'DSZ2', double-cation 'DC' and tetramethylammonium bromide.

Conclusions and future work

A new family of bolaform dizwitterions based on TMEDA, TMPDA and TMHDA di-sulfonates was taken to ISIS Neutron & Muon Source in March for neutron scattering measurements of their

solution-state structure, alongside measurements of zwitterionic salts and double-zwitterions in phenolic aqueous solution to determine interactions with hydrophobes. These systems are now being modelled using EPSR modelling and further fundamental structural information will be extracted from these. We will attempt to form monocrystals of the synthesised compounds to contrast the solution-state structure with the crystal structures. We have measured physical properties of the prepared compounds and determined an effective order of kosmotropicity through interpreting the effect of added salts on solution viscosity. We will continue to prepare novel zwitterionic materials and measure their properties to determine the best candidates to create functionalised protein-resistant surfaces, contrasting this with scattering measurement and modelling where possible. Synthesis will be attempted of precursors for surface functionalisation, and the ability of these to resist protein attachment will be screened systematically.

References

1. Blaszykowski, C.; Sheikh, S.; Thompson, M. Surface Chemistry to Minimize Fouling from Blood-Based Fluids. *Chem. Soc. Rev.* **2012**, *41* (17), 5599–5612. https://doi.org/10.1039/c2cs35170f.
2. Kane, R. S.; Deschatelets, P.; Whitesides, G. M. Kosmotropes Form the Basis of Protein-Resistant Surfaces. *Langmuir* **2003**, *19* (6), 2388–2391. https://doi.org/10.1021/la020737x.
3. Wu, B.; Kuroda, K.; Takahashi, K.; Castner, E. W. Structural Analysis of Zwitterionic Liquids vs. Homologous Ionic Liquids. *J. Chem. Phys.* **2018**, *148* (19), 193807. https://doi.org/10.1063/1.5010983.
4. Callow, J. A.; Callow, M. E. Trends in the Development of Environmentally Friendly Fouling-Resistant Marine Coatings. *Nat. Commun.* **2011**, *2* (1), 210–244. https://doi.org/10.1038/ncomms1251.
5. Baggerman, J.; Smulders, M. M. J.; Zuilhof, H. Romantic Surfaces: A Systematic Overview of Stable, Biospecific, and Antifouling Zwitterionic Surfaces. *Langmuir* **2019**, *35* (5), 1072–1084. https://doi.org/10.1021/acs.langmuir.8b03360.
6. Blesic, M.; Gilmore, B. F.; Holbrey, J. D.; Jacquemin, J.; Level, G.; Nockemann, P.; Stella, L. An Introduction to Zwitterionic Salts. *Green Chem.* **2017**, *19* (17), 4007–4011. https://doi.org/10.1039/c7gc01523b.
7. Level, G.; Vieira Fadul, M.; Blesic, M. Solubility-Modifying Power of Zwitterionic Salts. *ChemPhysChem* **2018**, *19* (5), 575–580. https://doi.org/10.1002/cphc.201701229.
8. Soper, A. K. Partial Structure Factors from Disordered Materials Diffraction Data: An Approach Using Empirical Potential Structure Refinement. *Phys. Rev. B* **2005**, *72*, 104204. https://doi.org/10.1103/PhysRevB.72.104204.
9. Jorgensen, W. L.; Maxwell, D. S.; Tirado-Rives, J. Development and Testing of the OPLS All-Atom Force Field on Conformational Energetics and Properties of Organic Liquids. *J. Am. Chem. Soc.* **1996**, *118* (45), 11225–11236. https://doi.org/10.1021/ja9621760.
10. Jorgensen, W. L.; Nguyen, T. B. Monte Carlo Simulations of the Hydration of Substituted Benzenes with OPLS Potential Functions. *J. Comput. Chem.* **1993**, *14* (2), 195–205. https://doi.org/10.1002/jcc.540140207.
11. Canongia Lopes, J. N.; Pádua, A. A. H.; Shimizu, K. Molecular Force Field for Ionic Liquids IV: Trialkylimidazolium and Alkoxycarbonyl-Imidazolium Cations; Alkylsulfonate and Alkylsulfate Anions. *J. Phys. Chem. B* **2008**, *112* (16), 5039–5046. https://doi.org/10.1021/jp800281e.
12. Cao, Z.; Zhang, L.; Jiang, S. Superhydrophilic Zwitterionic Polymers Stabilize Liposomes. *Langmuir* **2012**, *28* (31), 11625–11632. https://doi.org/10.1021/la302433a.

QUILL Quarterly Report

February – April 2019

Name:	**Yongdi (Dean) Lou**		
Supervisor(s):	Prof John Holbrey		
Position:	MPhil of Chemical Engineering		
Start date:	01-10-2018	Anticipated end date:	31-12-2019
Funding body:	-		

IL as a Dissolution System for Preparing Graphene/ Cellulose Based Materials

Background

Cellulose composite polymers have been considered as advanced environmental- friendly materials that can be biocompatible and biodegradable, and already have produced mature industrial applications such as in the textile industry. However, because of the dense hydrogen bonding present in cellulose, it presents severe problems for dissolution and processing. Room temperature ionic liquids, especially those which contain strong hydrogen bond acceptor anions, have been reported to be effective and promising cellulose solvents. Graphene continues to play an important role in many fields such as carbon nano-materials because of its unique optical, electrical, mechanical, and structural properties. The large delocalized π-electron system and high theoretical specific surface area of graphene make the material suitable for electronic composites or adsorbent/thermal conduction materials. The pure ionic nature of ionic liquids can also help stabilize the dispersion of graphene in materials by insertion into the sheet structure. This ability of ionic liquids to both stabilize graphene dispersions and dissolve cellulose suggests their application as solvents to prepare cellulose/graphene composite, however, many challenges such as the slow dissolution rate of cellulose, inhomogeneous dissolution, and strong shrinkage of aerogel dehydration still restricts the development of this method. This project explores the preparation of outstanding graphene/cellulose composites by dissolution, regeneration, and modification in order to construct monolithic composites with controlled porosity and structure.

Objective of this work

The solubility characteristics of cellulose in different ionic liquids should be studied and summarized. Combined with the characterization of the prepared materials, one or several ionic liquids should be screened out as an excellent dissolution system for preparing cellulose materials. Find the most promising application direction by studying the properties and characterization of cellulose composites. Therefore, the goal of this project is to explore a cellulose/graphene composite material, the preparation process is based on the dissolution and regeneration in ionic liquids. Through the modification process to achieve two purposes: reduction of graphene oxide and reducing dehydration shrinkage of cellulose aerogels.

Progress to date (new)

1. IL preparation and synthesis

i) Preparation of general ionic liquids [Hemim]Cl, [DBU][OAc] according to literature steps.
ii) Preparation of Dialkyl-phosphate anion ionic liquids using microwave reactor *Monowave 400*. Mainly synthetic IL: [Emim][DMP] (DMP: Dimethyl-phosphate).

2. Cellulose, Cellulose/GO composite dissolve in different solvent systems and regenerate in distillation water, hydrogel was immersed into Vitamin C soln. to reduce GO to reduction GO (rGO).

i) Finished dissolution rate compares.
ii) Tried different regeneration methods, obtained different shapes of hydrogel.
iii) Adjusted GO mass presents in GO/cellulose composite from 1% to 10%.
iv) Solvent regeneration with water evaporation and vacuum distillation.
v) Observe the volume shrinkage of the materials by oven-dried and freeze-dried methods.

3. Hydrogel composites modification: single co-solvent system replacing treatment by alcohol solvent (methanol, ethanol, and *n*-butanol) and non-hydrophilic solvent toluene. Observed whether it could effectively control the shrinkage of materials from hydrogel to aerogel.

4. Tests conducted so far.

i) NMR tests for Dialkyl-phosphate anion ionic liquids and [DBU][OAc], [Hemim]Cl structural presumption.
ii) FT-IR tests for composition and functional group determination of Cellulose and Cellulose/GO aerogels.
iii) SEM tests for synthesized composites morphology display.
iv) TGA & XRD tests for composites morphology characteristic.
v) Auxiliary tests (eg: Chloride contents tests) submitted to and finished by ASEP.

Conclusions

In summary, a series of GO/cellulose composites have been synthesized in this project. Using a hydrogen bond acceptor type ionic liquid to better dissolve cellulose, try to dissolve cellulose and graphene oxide using a variety of ionic liquids, and through distillation water regeneration, modification, and different drying methods to obtain different material structure. In the ionic liquids synthesis stage, a sealed microwave reactor and a new reaction procedure were used of microwave-assisted reaction. It was found that the ionic liquid 1-ethyl-3-methylimidazolium dimethyl-phosphate prepared by the reaction has a good dissolution for cellulose. Determines the characterization and spatial structure, and found that graphene (GO/rGO) can be well embedded in the cellulose skeleton. For the modification section, the single co-solvent systems replacement does not effectively solve the problem of material shrinkage.

Future work

1. Complementary the experiment of ILs solubility for cellulose.
2. Prepared the 7×7cm mould for the regeneration of cellulose/GO to prepare composites film. Try to use longitudinal pressurization with acetylation and co-solvent replacement to reduce material shrinkage to achieve the experimental direction.
3. BET testing to explore materials pore characterization, and other testing to complete experimental data.
4. The application direction of the material is set as a graphene-cellulose thermal-stable composite, and the corresponding material preparation research and characterization performance test will be carried out.

QUILL Quarterly Report

February - April 2019

Name:	**Peter McNeice**		
Supervisor(s):	Dr Andrew Marr and Dr Patricia Marr		
Position:	PhD student		
Start date:	October 2016	Anticipated end date:	July 2020
Funding body:	QUILL IAB		

Base Stable and Basic Ionic Liquids

Background

The imidazolium cation is the most common cation in ionic liquids due to its acid stability, thermal stability and oxidative stability.[1] Unfortunately, it can be extremely sensitive to base. The most acidic position is the C2 proton which deprotonates to form a carbene (Figure). The instability of the C2 position in base was demonstrated in 1964 with heavy water buffers causing deuteration at the C2 position.[2] The acidity of this proton limits the use in base catalysed reactions. This has been investigated by Aggarwal *et. al.*[3] who found that [BMIM][Cl] was deprotonated to form a carbene which went on to attack the aldehyde component of a Baylis-Hillman reaction, reducing the yield. They found that bases with pK_a as low as 8 or 9 could generate a carbene.

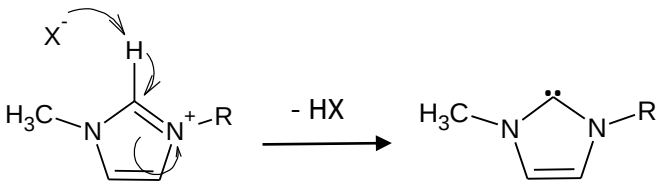

Figure 1 - Deprotonation of an imidazolium cation to form a carbene. X^- can be the anion or a base.

When an ionic liquid is able to catalyse a reaction, it is called a functionalised ionic liquid (FIL), previously known as task specific ionic liquids (TSIL).[4] These materials can be created due to the tuneable properties of ionic liquids and have the potential to cut down on auxiliary stoichiometric catalysts and prevent the formation of salts.

Ionic liquids can be basic due to the presence of a Brønsted basic (proton accepting) anion. Examples include ionic liquids with OH^-,[5] imidazolate ($[Im]^-$),[6] carboxylate,[7,8] amino acids[9] and dicyanamide ($[DCA]^-$)[10] as anions (Figure).

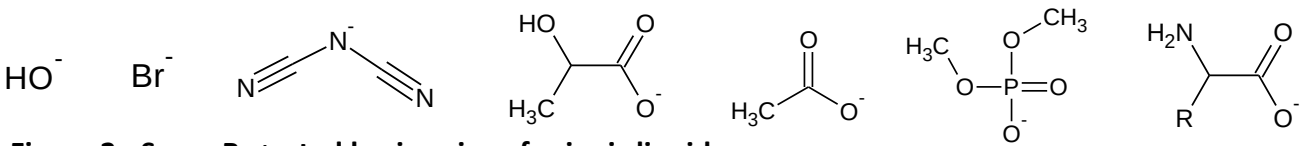

Figure 2 - Some Brønsted basic anions for ionic liquids.

Ionic liquids with basic anions often suffer from instability. The anion is able to attack the cation to form two neutral species as shown in Figure . Strong bases such as halide ions and OH^- in particular suffer from this effect.

Heterogenising ionic liquids can increase their stability and allows for simple separation of the ionic liquid catalyst from the reaction mixture. Gels are 99 % liquid and yet do not flow due to the 1 % solid forming a matrix which entraps the liquid phase.[11] The solid matrix is porous and allows materials to diffuse into and out the liquid phase, prompting gels to be used in entrapping homogeneous catalysts.[12,13] Gels made from neutral ionic liquids and catalysed by base have been prepared but these have exhibited poor mechanical strength.[14] This occurs because the base-catalysed sol-gel process causes the reaction seen to proceed too quickly. This creates large sol particles which leads to opaque gels with low porosity, low mechanical strength and a denser ceramic structure.[15] Bothwell and Marr[16] have demonstrated a solution to this problem. They used the basic ionic liquid $[P_{66614}][OH]$ to catalyse the sol-gel formation of SiO_2 and TiO_2 ionic liquid gels. The gels formed were clear and had good mechanic stability.

Objective of this work

The overall aim of this project is to synthesise functionalised ionic liquids which are base stable and basic. Basic ionic liquids will be able to act as both solvent and catalyst for reactions, which will eliminate waste. Stability is key for catalysis as well as recovery of the ionic liquid.

Progress to date

Previous reports have shown the use of binary basic ionic liquids to catalyse Knoevenagel and Aldol reactions.[17,18] The ionic liquid could not be recycled homogeneously. Physisorbed SILPs were also prepared which could catalyse the Knoevenagel reaction but the ionic liquid leached from the silica support.[19] Unlike SILPs where the ionic liquid is only physically absorbed, a gel entraps the ionic liquid within a silica matrix.[20] Adopting the method of Bothwell and Marr,[16] ionic liquid gels were formed by mixing TEOS with $[Pyrr_{14}][NTf_2]$ and $[Pyrr_{14}][O^iPr]$ solution at room temperature and leaving overnight to gel (Figure). This allowed a range of basic gels to be formed. Ionic liquid gels have been shown to have increased stability when a hydrophobic ionic liquid is present alongside a basic ionic liquid.[21]

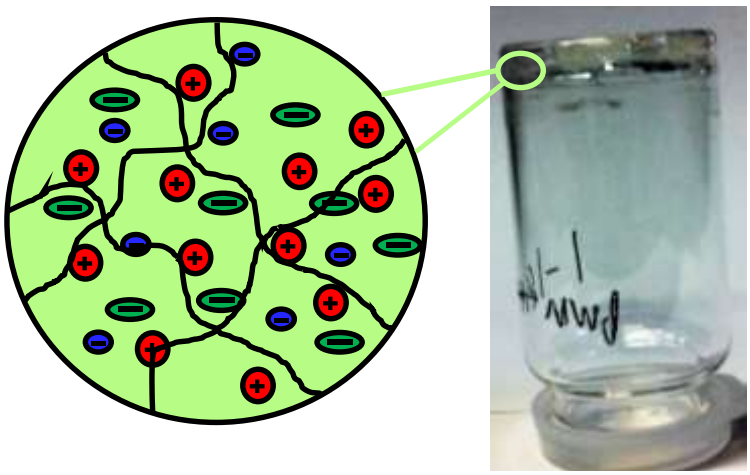

Figure 3 - An ionic liquid gel and representation of its structure.

Table 1 - Decomposition temperatures of $[Pyrr_{14}][NTf_2]_x[O^iPr]_{1-x}$ gels.

Entry	Gel	T_d (°C)[a]
1	$[Pyrr_{14}][NTf_2]_{0.81}[O^iPr]_{0.19}$	230
2	$[Pyrr_{14}][NTf_2]_{0.59}[O^iPr]_{0.41}$	250
3	$[Pyrr_{14}][NTf_2]_{0.32}[O^iPr]_{0.68}$	235
4	$[Pyrr_{14}][O^iPr]$	244

[a] Onset decomposition temperature measured by TGA.

Table 1 shows that while the decomposition temperatures of the gels vary, there is not a trend between the ratio of ions and the decomposition temperature. This indicates that the gels are equally thermally stable. $[Pyrr_{14}][NTf_2]_{0.85}[O^iPr]_{0.15}$ and $[Pyrr_{14}][NTf_2]_{0.58}[O^iPr]_{0.42}$ bulk liquids had T_d of 242 °C and 229 °C respectively so the gels decomposition probably results from decomposition of the ionic liquid. No increase in thermal stability is observed after entrapping these ionic liquids within a gel. While the thermal stability does not seem reliant on the proportion of ions it has been shown that the addition of a hydrophobic ionic liquid to a basic ionic liquid gel can prevent leaching of the ionic liquid catalyst from the gel.[21]

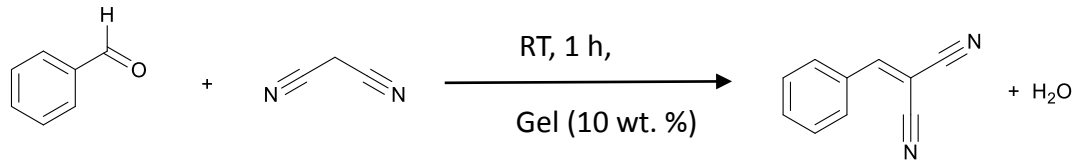

Figure 4 - Knoevenagel Condensation between malononitrile and benzaldehyde.

Table 2 - Yield of Knoevenagel condensation between Malononitrile and Benzaldehyde catalysed by 10 wt. % gel.

Entry	Gel	Yield / %[a] (±, SD)
1	$[Pyrr_{14}][NTf_2]_{0.81}[O^iPr]_{0.19}$	50 (1)
2	$[Pyrr_{14}][NTf_2]_{0.59}[O^iPr]_{0.41}$	36 (2)
3	$[Pyrr_{14}][NTf_2]_{0.32}[O^iPr]_{0.68}$	54 (4)
4	$[Pyrr_{14}][O^iPr]$	44 (6)

Conditions: Malononitrile (0.059 g, 0.089 mmol), benzaldehyde (0.084 g, 0.079 mmol), Gel (0.0086 g, 10 wt. %), DCM (0.127, 1:1 wt/wt DCM:Reagents), (RT, stir rate 500 RPM and time 1 h). [a] Obtained from ^{1}H NMR against a known mass of ethyl trifluoroacetate, value is an average of three reactions.

The gels were applied as heterogeneous catalysts to the Knoevenagel condensation between malononitrile and benzaldehyde (Figure). When the ionic liquids were used as homogeneous catalysts[18] or immobilised as SILPs[19] the yield of the reaction increases as the proportion of $[O^iPr]^-$ increased. This is not seen in the ionic liquid gel catalysed reaction (
Table). The yield varies between the gels but no trend is observed. The reactivity of the gels is affected by their structure as well as the amount of base. Base catalysed sol-gels typically form large sols, leading to less porous gels.[14,15] This means the reagents cannot diffuse into the gel easily. This could lead to the $[Pyrr_{14}][O^iPr]$ gel not having the highest yield despite containing the most base. Different ratios of the anions will form gels with different porosity and therefore the reactants will have different rates of diffusion into the silica matrix and different access to the basic catalyst.

As the reactions are performed on a small scale the entire gel is not used but it is broken into pieces. The morphology of the induvial pieces will also affect the reaction, larger gel pieces will have a lower surface area to interact with the reagents. This effect would probably average out over the three reaction runs performed and so is thought to have less affect than the structure of the gels. Coating the gels onto a surface may prevent diffusion limiting conditions of the reaction.

^{19}F NMR analysis of the reaction mixture did not show any peaks relating to the $[NTf_2]^-$ anion which indicates that any leaching is below the limit of detection of ^{19}F NMR. To further rule out the possibility of ionic liquid leaching out of the gel and catalysing the reaction a "hot filtration"[22] was performed. The reaction was carried out in three stages. In stage one the reaction was carried out normally for 20 minutes, the reaction was filtered and the filtrate was returned to the flask for the second stage. The final stage was when the gel was re-added to the reaction mixture and continued for 40 minutes. Samples were removed periodically and analysed by ^{1}H NMR to assess the yield (Figure). A slight increase in yield is seen between 20 and 30 minutes but this is likely to have occurred during filtration as there is no further increase while the gel is absent from the reaction mixture. Upon re-addition of the gel the yield increases. This test confirms that the gel is acting heterogeneously.

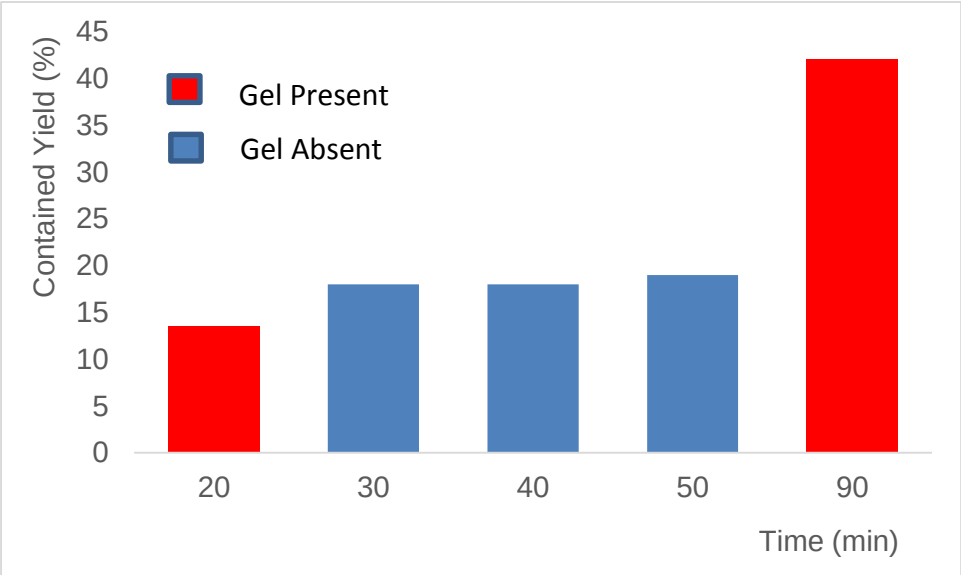

Figure 5 - Hot filtration test performed with $[Pyrr_{14}][NTf_2]_{0.32}[O^iPr]_{0.68}$.

When the reaction time was increased to 24 hours all gels gave 99 % yield. The gels were recovered by filtration after the reaction and washed with methanol. A recycling experiment was performed with $[Pyrr_{14}][NTf_2]_{0.32}[O^iPr]_{0.68}$ and the activity of the gel was maintained for three 24 hour cycles (Figure). This is further evidence that the ionic liquid is not leaching from the gel, nor is it being deactivated during the reaction. The formation of gels is a successful way to heterogenise the $[Pyrr_{14}][NTf_2]_{1-x}[O^iPr]_{1-x}$ ionic liquids to allow for them to be reused.

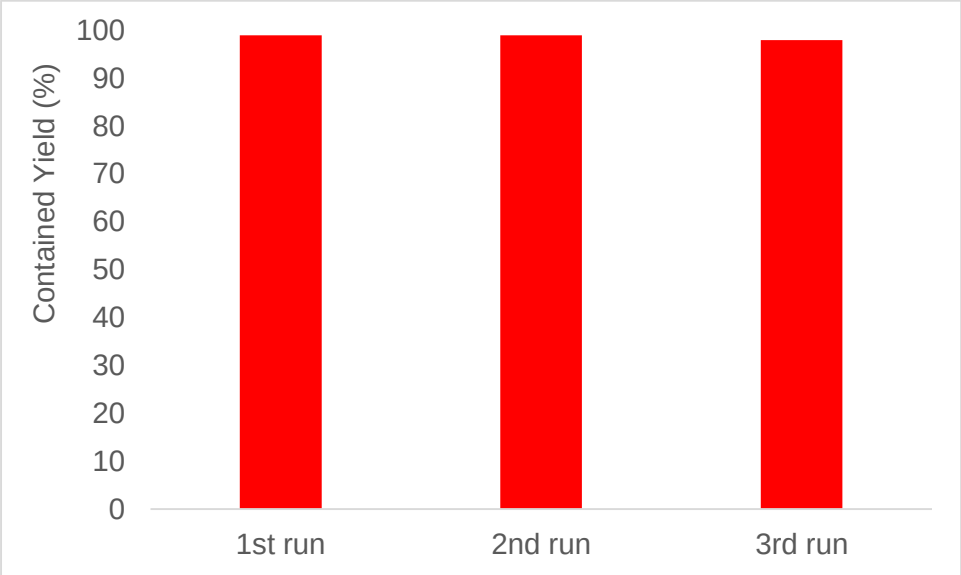

Figure 6 - Recycle of $[Pyrr_{14}][NTf_2]_{0.32}[O^iPr]_{0.68}$ for Knoevenagel reaction.

Conclusions and future work

$[Pyrr_{14}][NTf_2]_x[O^iPr]_{1-x}$ ionic liquids have been heterogenised within a silica matrix as gels. The gels produce moderate yields (36-54 %) in the Knoevenagel condensation between Malononitrile and benzaldehyde after 1 hour, and 99 % after 24 hours. The ionic liquid was found not to have leached from the gel *via* ^{19}F NMR and a hot filtration test. The gel was successfully reused for two further reactions without a drop in activity.

Further work will be performed to assess the diffusion limitations of the gels. Reactions will be performed at higher and lower rates of stirring to see whether there is a significant change in the yield which would indicate the reaction is diffusion limited. A spray coating process could be used during the synthesis of the gels to coat glass beads with the ionic liquid gels. This would create a thin, homogeneous layer of gel which would be less likely to be diffusion limited. BET analysis of the gels will be carried out to quantify the surface area and porosity of the gels to better understand their reactivity.

The catalytic activity and reuse of the gels has been demonstrated. This opens the potential for further modification. Our group has recently published a hydrogen transfer system where a basic ionic liquid gel and homogeneous catalyst acted in tandem but could not be combined in one material.[21] The new gels could be modified with catalyst or nanoparticles and tested for hydrogen transfer reactions which would allow for reuse of both the base and expensive metal catalyst.

References

1. S. T. Handy, *Curr. Org. Chem.*, 2005, **9**, 959-988.
2. R. A. Olofson, W. R. Thompson, J. S. Michelman, *J. Am. Chem. Soc.*, 1964, **86**, 1865-1866.
3. V. K. Aggarwal, I. Emme, A. Mereu, *Chem. Commun.*, 2002, 1612-1613.
4. A. C. Cole, J. L. Jensen, I. Ntai, K. Loan, T. Tran, J. K. Weaver, D. C. Forbes, J. H. J. Davis, *J. Am. Chem. Soc.*, 2002, **124**, 5962-5963.
5. J.-M. Xu, Q. Wu, Q.-Y. Zhang, F. Zhang, X.-F. Lin, *Eur. J. Org. Chem.*, 2007, 1798-1802.
6. H. Luo, Z. Zhai, W. Fan, W. Cui, G. Nan, Z. Li, *Ind. Eng. Chem. Res.*, 2015, **54**, 4923-4928.
7. Y. Liu, Y. Huang, P.-O. Boamah, L. Cao, Q. Zhang, Z. Lu, H. Li, *J. Appl. Polym. Sci.*, 2015, **132**, 41727.

8. A. Cieniecka-Rosłiewicz, K. Kita, A. Fojutowski, J. Nawrot, K. Materna, J. Pernak, *Chem. Eur. J.*, 2008, **14**, 9305-9311.
9. H. Peng, Y. Zhou, J. Liu, H. Zhang, C. Xia, X. Zhou, *RSC Adv.*, 2013, **3**, 6859-6864.
10. D. R. MacFarlane, S. A. Forsyth, J. Golding, G. B. Deacon, *Green Chem.*, 2002, **4**, 444-448.
11. J. W. Steed, *Chem. Commun*, 2011, **47**, 1379-1383.
12. F. Shi, Q. Zhang, D. Li, Y. Deng, *Chem. Eur. J.*, 2005, **11**, 5279-5288.
13. A. C. Marr, P. C. Marr, *Dalton Trans.*, 2011, **40**, 20-26.
14. M. A. Gelesky, S. X. Chiaro, F. A. Pavan, J. H. Z. dos Santos, J. Dupont, *J. Dalton. Trans.*, 2007, **47**, 5549-5553.
15. C. J. Brinker, G. W. Scherer, *Sol Gel Science*, Academic Press Limited, London, 1990.
16. K. M. Bothwell, P. C. Marr, *ACS Sustainable Chem. Eng.*, 2017, **5**, 1260-1263.
17. P. McNeice, *Base Stable and Basic Ionic Liquids*, QUILL Quarterly Report December-March 2018, Unpublished, March 2018.
18. P. McNeice, A. C. Marr, P. C. Marr, M. J. Earle, K. R. Seddon, Binary Alkoxide Ionic Liquids, *ACS Sustainable Chem. Eng.*, 2018, **6**, 13676-13680.
19. P. McNeice, *Base Stable and Basic Ionic Liquids*, QUILL Quarterly Report August-October 2018, Unpublished, November 2018.
20. P. C. Marr, A. C. Marr, *Green Chem.*, 2016, **18**, 105-128.
21. K. M. Bothwell, F. Lorenzini, E. Mathers, P. C. Marr, A. C. Marr, *ACS Sustainable Chem. Eng.*, 2019, **7**, 2686-2690.
22. J. E. Hamlin, K. Hirai, A. Millan, P. M. Maitlis, *J. Mol. Catal.*, 1980, **7**, 543-544.

QUILL Quarterly Report

February – April 2019

Name:	**Keith Moore**		
Supervisor(s):	Prof Peter Nockemann		
Position:	Project Manager		
Start date:	Feb 2019	Anticipated end date:	Sep 2019
Funding body:	IERC (ImpRESS)		

ImpRESS – Vanadium Redox Flow Energy Storage

Background

Increased uptake of renewable energy sources to replace fossil fuels in providing electricity is essential to combat the carbon emission that are escalating climate change around the world. However, supply of renewable energy (e.g. solar, wind, hydro) is rarely in sync with the times of peak demand on the energy grid. To make full use of the energy supplied by these "green" energy sources, it is essential that large scale energy storage solutions are found that can harvest the electricity when abundant and return it to the grid with a fast response when required.

A highly viable technology for this purpose is the vanadium redox flow battery, in which two tanks of electrolyte are used to store or deliver electrical energy by flowing them through an electrical cell. When charging VO^{2+} ions in the catholyte are oxidised to VO_2^{+}, while V^{3+} ions in the anolyte are reduced to V^{2+} ions. H^{+} transfer across a membrane allows the circuit to be completed.

The technology substantially rivals technology like lithium ion due to its lower cost, dramatically longer lifetime and greatly improved safety. However substantially improvement are still required for better efficiencies, power densities and grid integration.

Objective of this work

The ImpRESS energy storage project focuses on vanadium redox flow energy storage solutions for integration of renewable energy source into the all-Ireland electrical grid. The project seeks to improve the technology through development of new electrolytes (including through incorporation of ionic liquids) and testing of electrical models for grid integration.

Progress to date

As project manager I facilitate the day to day tasks of researchers on the project, liaise with partners and stakeholders in the project and assist with the preparation of grants to continue the project. This has included coordinating a mid-project review meeting in April, attending the 8th annual IERC conference, and assistance with a recently submitted application to CASE at QUB.

QUILL Quarterly Report

February – April 2019

Name:	**Gareth Nelson**		
Supervisor(s):	Prof John Holbrey and Dr Małgorzata Swadźba-Kwaśny		
Position:	PhD student		
Start date:	13/09/16	Anticipated end date:	13/09/19
Funding body:	DEL		

Ionic Liquid Catalysts for the Glycolysis of PET

Background

There are 4 broad types of PET recycling, primary recycling is pre-consumer scrap recycling. Secondary recycling is physical recycling, this approach first grinds the PET, then melts it before reforming it. The heat and force exerted in this process degrades the polymer leaving it unsuitable for many uses. Tertiary recycling is chemical recycling, the PET is recycled through chemical action, generally through depolymerisation of PET into constituent monomers. These monomers are re-polymerised to regenerate virgin PET. Quaternary recycling is the recovery of energy from the material, this is usually through incineration. This project focuses on chemical recycling of PET as it gives high quality polymers as a product. There are several methods for the depolymerisation of PET, these methods attack the ester linkage to break down the polymer. The use of alcohols (alcoholysis), amines (aminolysis), glycols (glycolysis), or water (hydrolysis) have previously been successful in the depolymerisation of PET. The focus of this project is glycolysis; this occurs through a transesterification reaction between PET and ethylene glycol, commonly catalysed by a metal acetate, carbonate or sulfate. This reaction is attractive because the product, BHET, requires no additional processing before being converted to PET thus is easy to incorporate into PET production. Work utilising ionic liquids as a catalysts was investigated by H, Wang et al.[1,2] Initially their work utilised imidazolium halide and several acidic ionic liquids, poor yields were achieved but this showed a new approach to the glycolysis reaction.[2] Q, Wang also utilised ionic liquids as catalysts, previously H, Wang had performed this reaction using [bmim][$FeCl_4$], the logical extension of this was to test other transition metal salt containing ionic liquids.[3,4] Q, Wang found that while [bmim][$FeCl_4$] was effective, $[bmim]_2[ZnCl_4]$ and $[bmim]_2[CoCl_4]$ were more effective, achieving similar conversion of PET (almost 100%) but greater yields of BHET with an increase of almost 20% over [bmim][$FeCl_4$] for both ionic liquids. Work in literature had previously used acetate ionic liquids, however the results reported were lower and required higher temperatures and more catalyst than those reported by H, Wang using halometallate ionic liquids.[5]

1. H. Wang, Y. Lui, Z. Li, X. Zhang, S. Zhang, and Y. Zhang, **Eur. Polym. J.,** 2009, **45**, 1535–1544
2. H. Wang, Z. Li, Y. Liu, X. Zhang, and S. Zhang, Green Chem., 2009, **11**, 1568-1575.
3. H. Wang, R. Yan, Z. Li, X. Zhang, and S. Zhang, Catal. Commun., 2010, **11**, 763–767.
4. Q. Wang, Y. Geng, X. Lu, and S. Zhang, ACS Sustain. Chem. Eng. 2015, **3**, 340−348
5. A.M. Al-Sabagh, F.Z. Yehia, A.M.M.F. Eissa, M.E. Moustafa, G. Eshaq, A.R.M. Rabie, and A.E. El-Metwally Ind. Eng. Chem. Res., 2014, **53**, 18443−18451

Objective of this work

The objective of this work is the production of bis(2-hydroxyethyl)terephthalate, a monomeric intermediate in PET production, from the glycolysis of waste PET. To achieve this, the applications of halometallate ionic liquids in the catalysis of the glycolysis of PET will be investigated and the use of acetate containing ionic liquids as catalyst for the glycolysis of PET will be explored.

Progress to date

Work was carried out on investigating the differences between [bmim][OAc] and [bmmim][OAc] as catal;ysts for this reaction, it is well documented that the acetate ionic liquids do produce in situ carbenes at higher temperatures. Looking further into this, reactions were performed at 195 °C and [bmim][OAc], [bmmim][OAc], [bmim]Cl, and [bmmim]Cl were selected for use as catalysts. These ionic liquids were chosen to show the impact of the acetate ion as well as the effect of C(2)-methylation. The HPLC traces for the experiments using [bmim]Cl and [bmmim]Cl as catalysts showed abnormally high noise. This means that the yield calculated for these reactions are likely far higher than they should be. These samples are set to be run again to return HPLC traces without excessive noise. The results in figure 1 show that the presence of an acetate ion in these ionic liquids is required to drive the reaction forward. However, the method by which the acetate drives the reaction differs between [bmim][OAc] and [bmmim][OAc]. This can be seen by the differences in yields across time, with [bmmim][OAc] appearing to be an exponential curve whereas the reaction with [bmim][OAc] appears to be a logarithmic graph instead. This shows that the rate of reaction for [bmim][OAc] is much higher as it breaks apart the polymer chain more rapidly until plateauing towards to end as there is less available PET and its oligomers to break apart. When [bmmim][OAc] is used as a catalyst the same end result is achieved, however the reaction rate is much poorer and requires more time to achieve the same results but doesn't yet plateau.

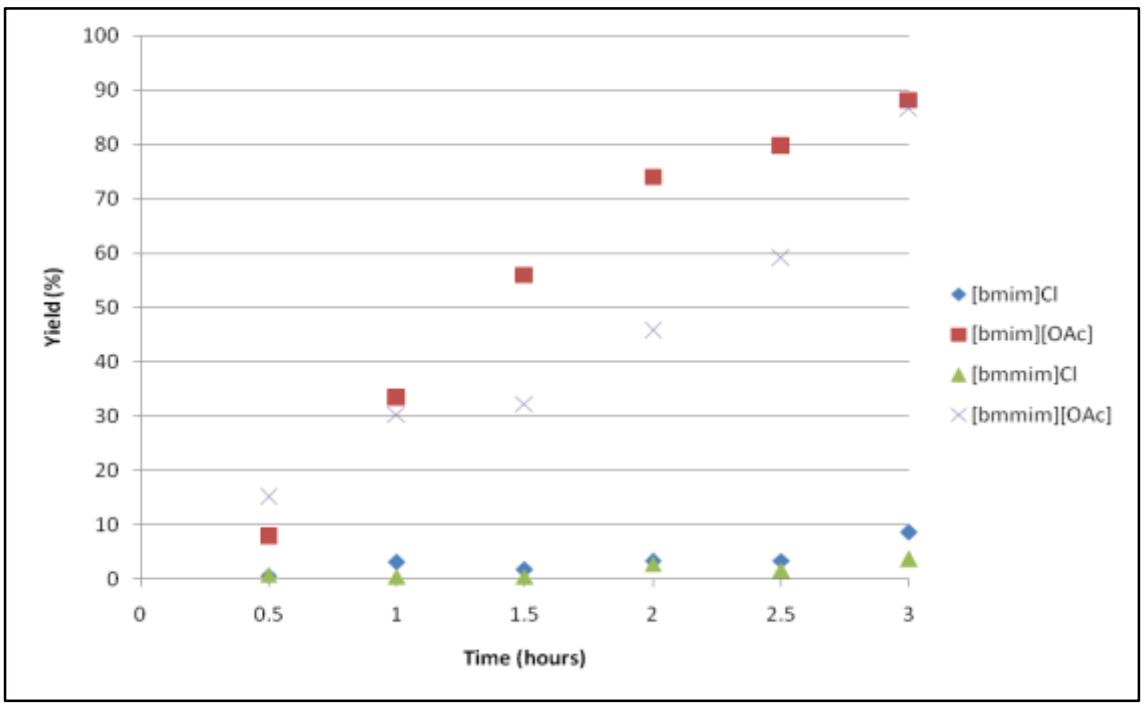

Figure 1 - Graph to show yield of BHET using ionic liquid catalysts in the glycolysis of PET, temperature 195 °C, 0.01 mol catalyst, 2 g PET and 20 g ethylene glycol at 195 °C.

A set of experiments were performed in which [bmim][OAc] and [bmimm][OAc] were used separately as catalysts while the temperature was varied, shown in figure 2. From this it can be seen

that increasing the temperature correlates to an increase in conversion and yield. It also suggests that catalysis only occurs at 170 °C and higher, this is similar to the minimum catalytic temperature for $[bmim]_2[ZnCl_4]$ and many other halometallate ionic liquids that were tested in the literature. There is a clear difference in the probable mechanism of the reaction when looking at figure 1, which was performed at 195 °C. However below reflux temperatures, even 190 °C (figure 3), we don't see a clear difference in the yields over time to suggest a meaningful change in mechanism. This difference in mechanism is likely a switch from using acetate as a base to the acetate abstracting the C(2) proton to form a carbene which is a far more potent base than the acetate ion. Thus it more rapidly increases until it plateaus at a maximum yield whereas the acetate barely achieves the maximum yield by the 3 hours of the reaction.

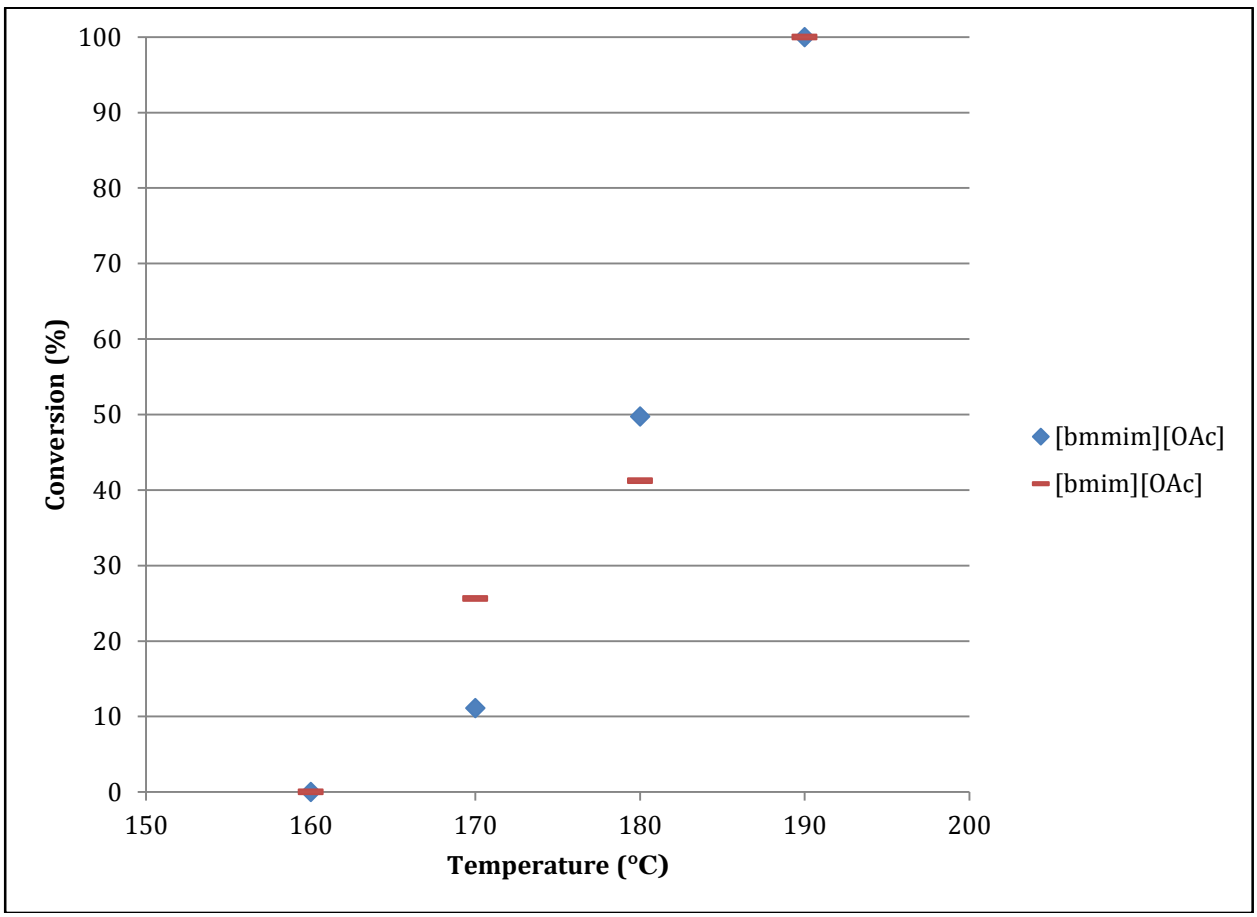

Figure 2 - Graph to compare conversion at different temperatures using [bmim][OAc] or [bmmim][OAc] in the glycolysis of PET, 0.01 mol catalyst, 2 g PET and 20 g ethylene glycol, reaction time 3 hours.

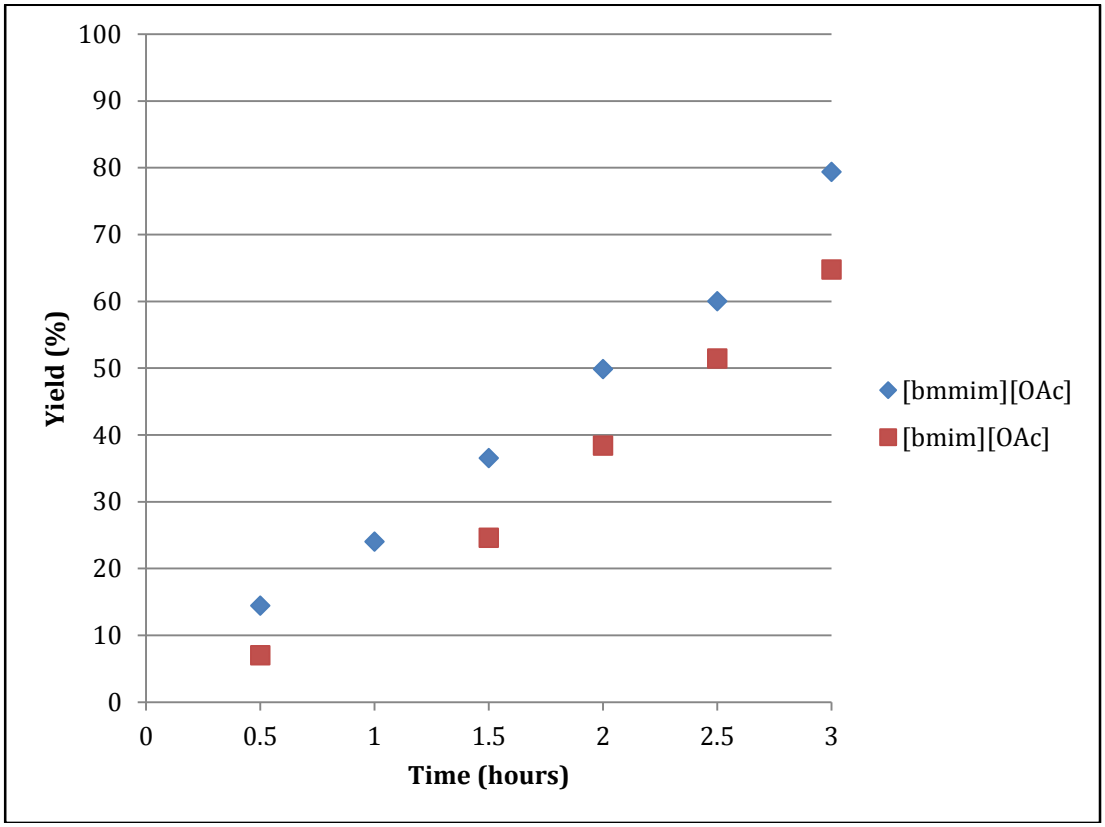

Figure 3 - Graph to compare conversion using [bmim][OAc] or [bmmim][OAc] in the glycolysis of PET, 0.01 [bmim][OAc], 2 g PET and 20 g ethylene glycol at 190°C.

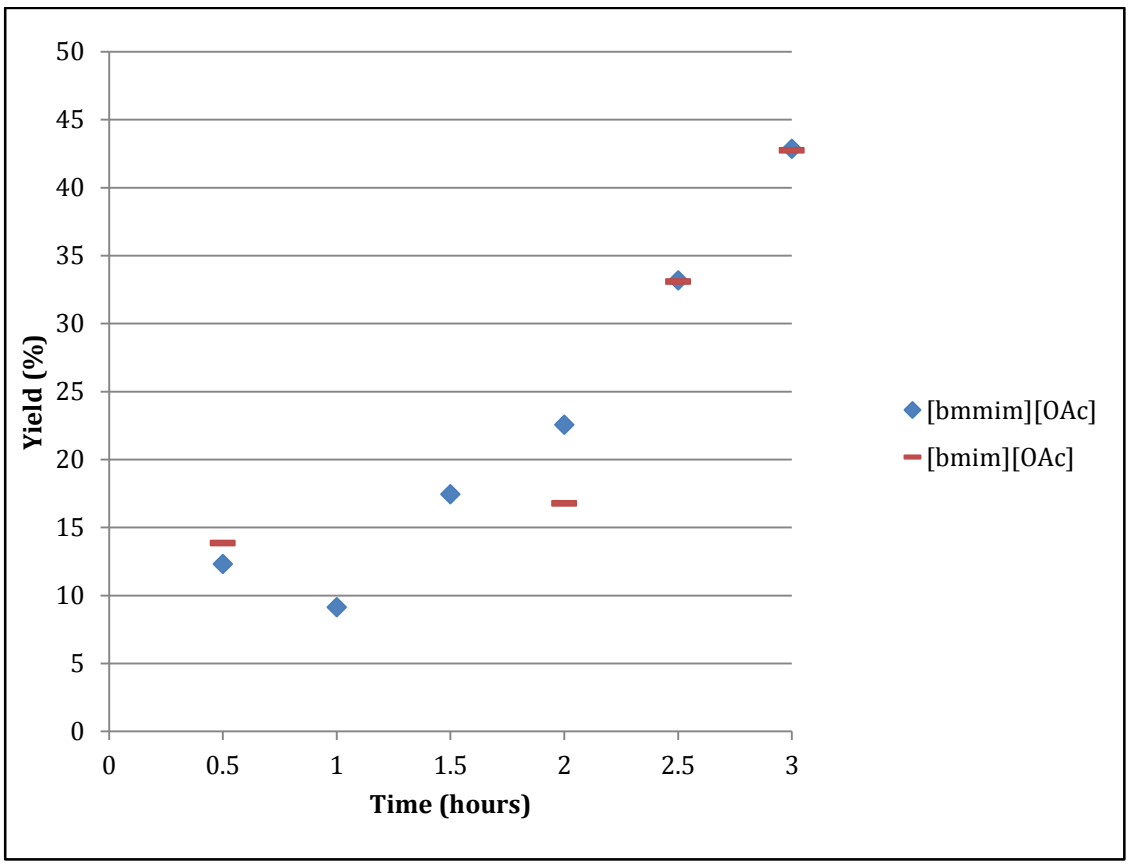

Figure 4 - Graph to compare conversion using [bmim][OAc] or [bmmim][OAc] in the glycolysis of PET, 0.01 [bmim][OAc], 2 g PET and 20 g ethylene glycol at 180°C.

Other work that was investigated was the potential addition of tetraphenyl phosphonium bromide to salts known to be active in the glycolysis as a way to improve the separation of catalyst and potential dyes from the reaction mixture. The catalysts used were $[PPh_4][OAc]$, $[PPh_4]Br/NaCO_3$, and $[PPh_4]Br/Zn(OAc)_2$ and followed the same method as previous glycolysis reactions. While these catalysts worked well, I was unable to achieve any separation and so the work was stopped at this point.

Conclusions and future work

From the work that I have performed it is clear that at 180 °C the acetate ionic liquids are effective catalysts due to the basicity of the acetate ion and that the cation's role in the reaction is limited to directing effects utilising either the C(2) proton or the positively charged nitrogen in the imidazole ring. This is illustrated by the similarity in the results between [bmim][OAc] and [bmmim][OAc]. A direct comparison between [bmim][OAc] and [bmmim][Oac] at 195 °C shows that both catalysts proceed through different mechanisms, this difference is due to the methylation of the C(2) position as it is the sole difference between the reactions. Since a proton in the C(2) position allows for in situ carbene formation these results further support the idea that this reaction continues through a carbene type mechanism.

My plans for future work are to initially gather data for both [bmim][OAc] and [bmmim][OAc] as catalysts across a range of times and temperatures. Next is to investigate possible additives to induce carbene formation whilst being unreactive themselves. This will initially look at basic group 1 and group 2 salts. These tests will run at 195 °C initially but the temperature will then be lowered to determine the minimum temperature at which the carbene will form.

QUILL Quarterly Report

February - April 2019

Name:	**Kathryn Ralphs**		
Supervisor(s):	Dr Nancy Artioli and Dr Gosia Swadźba-Kwaśny		
Position:	PDRA		
Start date:	01/06/2018	Anticipated end date:	30/06/2019
Funding body:	CASE/QUB/QUILL/Energia		

Renewable methanol from biogas for a low carbon economy in Northern Ireland

Background

Methanol is gaining increasing importance as a precursor to alternative fuels, fuel cells, DME and LPG. However, currently the UK methanol market accounts for only 4% of the European market, resulting in reliance on importation of methanol. Most methanol synthesized worldwide is from syngas (200 °C, up to 100 bar) obtained from natural gas (fossil fuels).

In this project we are investigating the direct hydrogenation of CO_2 to methanol. The hydrogen used will be obtained from water electrolysis from energy obtained from a curtailed wind farm. CO_2 is a waste product from anaerobic digestor plants. (In the UK there are 640 AD plants and 270 curtailed wind farms).

The direct hydrogenation of CO_2 to methanol recycles CO_2 (major cause of global warming) into a fuel and can provide a source of hydrocarbons. The process is exothermic and hence favours low temperatures and high pressures. However high temperatures are required to achieve a sufficient rate of reaction. At high temperatures the RWGS reaction dominates, reducing selectivity to methanol. In commercial processes the process is operated at low one pass conversions and relies on recycling unconverted reactants to attain high conversions.

In this project we aim to design and synthesize an optimized catalyst to improve methanol selectivity. We are currently investigating Solid catalysts with an ionic liquid layer (SCILL) catalysts as it is thought that an ionic liquid layer on the commercial $CuZnO/Al_2O_3$ catalyst will increase the concentration of the CO_2 near the active site. In the literature the positive effects of ionic liquids on CO_2 hydrogenation to *e.g.* formic acid has been described e.g. stabilization of transition states. At a later stage of the project a novel type of microchannel fixed bed reactor will be developed. This configuration will allow for simultaneous increase in the reaction temperature, pressure and space velocity, resulting in shifting of the equilibrium conversion per pass of CO_2 and boosting catalytic activity.

Objective of this work

The objective of the project is to hydrogenate CO_2 to methanol in high yield and selectivity. This will be achieved by the development of a SCILL based on $CuZnO/Al_2O_3$ and an ionic liquid that will increase the concentration of CO_2 next to catalyst active sites and increase the selectivity towards methanol product. We will also investigate reactor design and optimization. However, as this was a 6-month feasibility study we have only focused on the catalyst design at this time.

Progress to date

Experimental

Ionic liquid synthesis

$[PPh_4][NTf_2]$ was synthesized by an ion exchange of 2.54 g (8.8 $x10^{-3}$ mol) of $Li[NTf_2]$ and 3.32 g (7.9 x 10^{-3} mol) of $[PPh_4]Br$ (Alfa Aesar) in deionized water. The precipitated product was filtered and washed thoroughly with water to remove bromide impurities. The material was dried overnight under vacuum at 150 °C.

$[PPh_4][Bu^FSO_3]$ was synthesized by an ion exchange of 2.98 g (8.8 x 10^{-3} mol) of potassium nonafluoro-1-butanesulfonate and 3.32 g (7.9 x 10^{-3} mol) of $[PPh_4]Br$ (Alfa Aesar) in deionized water. The precipitated product was filtered and washed thoroughly with water to remove bromide impurities. The material was dried overnight under vacuum at 150 °C.

[BMIM][OAc] and [HMIM][FAP] ionic liquids were provided by QUILL.

SCILL synthesis

SCILL's were prepared by dissolving the required amount of ionic liquid to give the desired loading of ionic liquid in 10 ml methanol. To this the required amount of $CuZnO/Al_2O_3$ catalyst was added and the solution stirred for 1 h. The methanol was then removed by rotary evaporation and the SCILL was dried overnight under vacuum at 80 °C.

XRD

The XRD measurements in this work were carried out on a PANanalytical X'Pert Pro X-ray diffractometer. The X-ray source was copper with a wavelength of 1.5405 Å. All measurements were carried out ex-situ using a spinning stage. The diffractograms were recorded from 4° to 75° with a step size of 0.017°.

SEM

SEM analysis in this work was carried out on a Quanta FEG 250 Scanning Electron Microscope. The samples were prepared by placing a small amount of sample on double sided carbon and mounting on a specimen stub. SEM was then carried out under high vacuum and images of the sample recorded in the range of magnifications.

TPR

TPR was carried out on a custom-built rig. The samples were first treated with O_2 at 30 °C for 30 min. The temperature is then increased to 500 °C and held for 20 min. The sample is then cooled to 30 °C. Following this the sample is treated with H_2 at 30 °C for 30 min before increasing the temperature to 500 °C and holding for 30 min. The temperature is then reduced to 30 °C.

Activity tests

Catalytic assessment for CO_2 hydrogenation was carried out in a fixed bed reactor. The catalyst (0.5 g) was placed in a stainless steel tube reactor with an ID of 8mm and a length of 34 cm, occupying a length of ca. 3-6 cm depending on the catalyst. Prior to testing, catalysts were pre-reduced in situ in a flow of 90% H_2 gas and 10% N_2 at 300 °C for 4.5 h. The system was then cooled to ambient then N_2 was flowed over the catalyst for 30 min. The temperature was then increased to 250 °C and pressurised to 20 bar with the reactant gases (1 CO_2 :3 H_2: 1 N_2). A standard reaction gas flow rate of 100cc/min was used throughout the experiment (GHSV 6200 h^{-1}). To avoid product condensation, post reactor lines and valves were heated at 130 °C. Products were analysed via on-line gas chromatography using an Agilent 7820A system fitted with both FID and TCD detectors. Nitrogen was used as an internal standard. The reaction was carried out for 4-16 h.

Results and discussion

To date we have investigated two different classes of ionic liquids to prepare SCILL's; ionic liquids with high thermal stability ($[PPh_4][NTf_2]$ and $[PPh_4][Bu^FSO_3]$) and ionic liquids with lower thermal stability ([BMIM][OAc] and [HMIM][FAP]) (Table 1). The ionic liquids with low thermal stability have been reported in the literature to have good CO_2 solubility or a desirable effect on reactions involving the hydrogenation of CO_2. However, TPR analysis have indicated that during the reduction step these ionic liquids are not stable and decompose on the catalyst. We have investigated the use of ionic liquids with a higher thermal stability due to the high temperature (300°C) required to pre-treat the catalyst prior to the reaction. We have also investigated TMC due to their very high thermal stability.

In addition to catalyst development we have also investigated the pre-treatment step of the catalyst and have determined that a two-step reduction technique works best. The catalyst is reduced first at 170 °C at a rate of 5°C /min after which the temperature is held at 170 °C for 1 h until it is then increased up to 300 °C at a rate of 3 °C/min and held for 2 h in a flow of H_2 gas. The catalyst is then cooled to room temperature under a flow of N_2.

Table 1 - Ionic liquids used in this work

Anion	Cation	Ionic liquid	Properties
OAc	BMIM	[BMIM][OAc]	Buffers reaction, good CO_2 solubility
FAP	HMIM	[HMIM][FAP]	High affinity for CO_2, long carbon chain
Bu^fSO_3	PPh_4	$[PPh_4][Bu^fSO_3]$	High thermal stability (stable to 300 °C +)
NTf_2	PPh_4	$[PPh_4][NTf_2]$	High thermal stability (stable to 300 °C +)

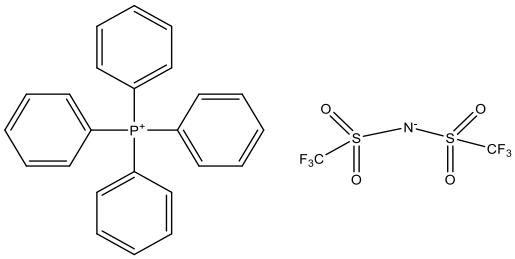

[PPh4][NTf2]

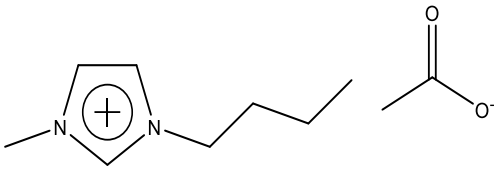

[BMIM][OAc]

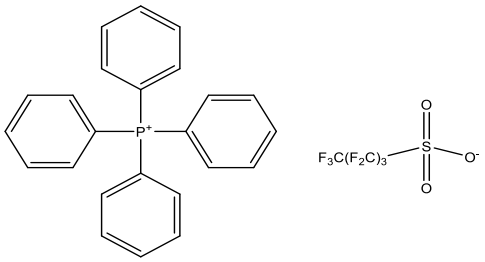

[PPh4][BufSO3]

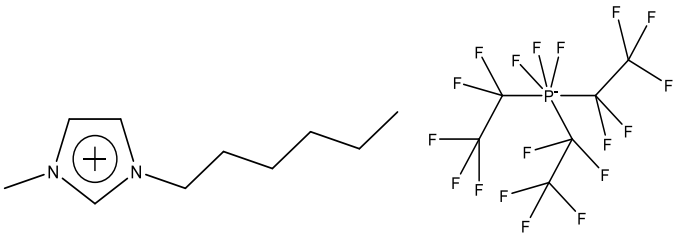

[HMIM][FAP]

Figure 1 - Ionic liquids used in this work

Characterization

TPR

Catalysts prepared are initially analysed by temperature programmed reduction (TPR) as an estimate of activity. Generally, the lower the reduction temperature the more active the catalyst. Fig 2 shows the TPR data for the commercial catalyst and the two SCILL's prepared with ionic liquids with lower thermal stability. The reduction temperature for the $CuZnO/Al_2O_3$ catalyst is approx. 440 K. The reduction temperature for $CuZnO/Al_2O_3$ [BMIM][OAc] SCILL is very similar. This indicates that the due to the lack of thermal stability of the ionic liquid on this catalyst, at high temperatures the ionic liquid has decomposed, and we are in fact analysing the commercial catalyst rather than the SCILL. The reduction temperature for the $CuZnO/Al_2O_3$ [HMIM][FAP] SCILL is around 430 K, however it has shifted to the right and is more difficult to reduce indicating a reduced activity.

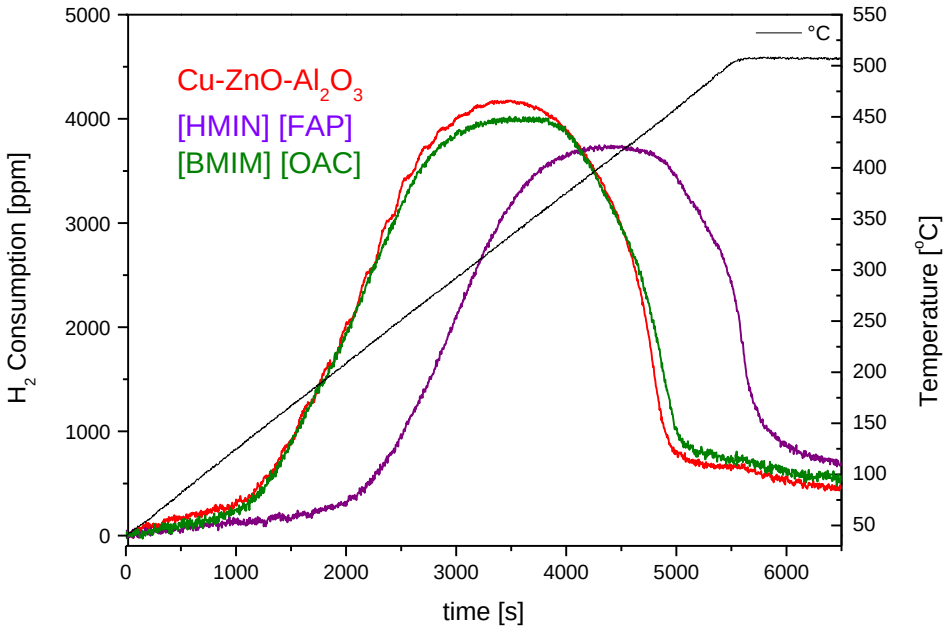

Figure 2 - TPR of catalysts and SCILL's with lower thermal stability

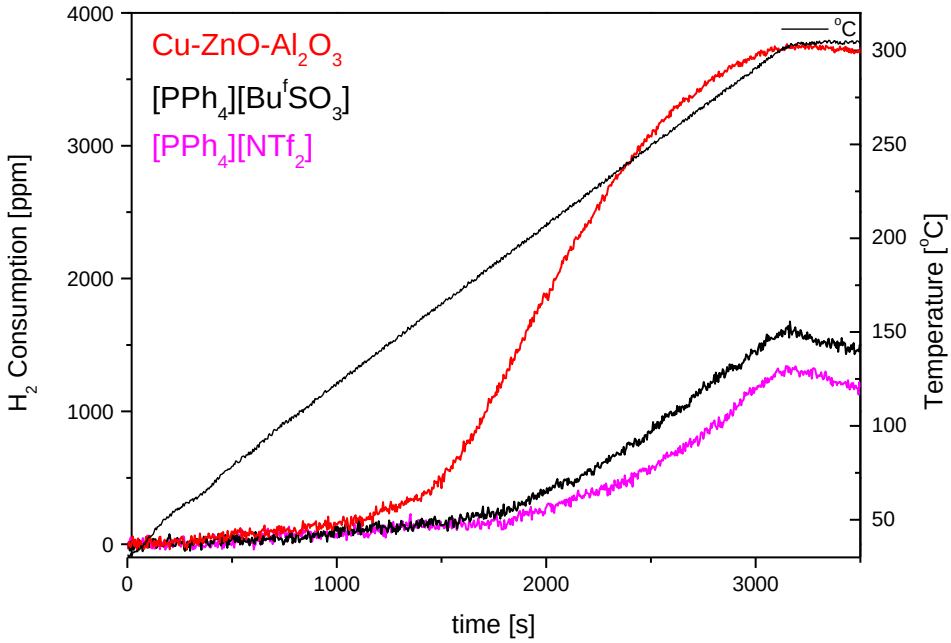

Figure 3 - TPR of catalysts and SCILL's with high thermal stability

Figure 3 shows the TPR data for the two SCILL's with the high thermal stability ionic liquid. The TPR's for both catalysts indicated they are difficult to reduce and therefore catalytic activity is likely to be poor. However, catalytic testing revealed that the $[PPh_4][NTf_2]$ based SCILL results in a change in selectivity from methanol (54% methanol, 46% C-C4 alkanes) and the $[PPh_4][Bu^FSO_3]$ based catalyst shows increased selectivity towards methanol (94% vs 88%) compared to the commercial catalyst.

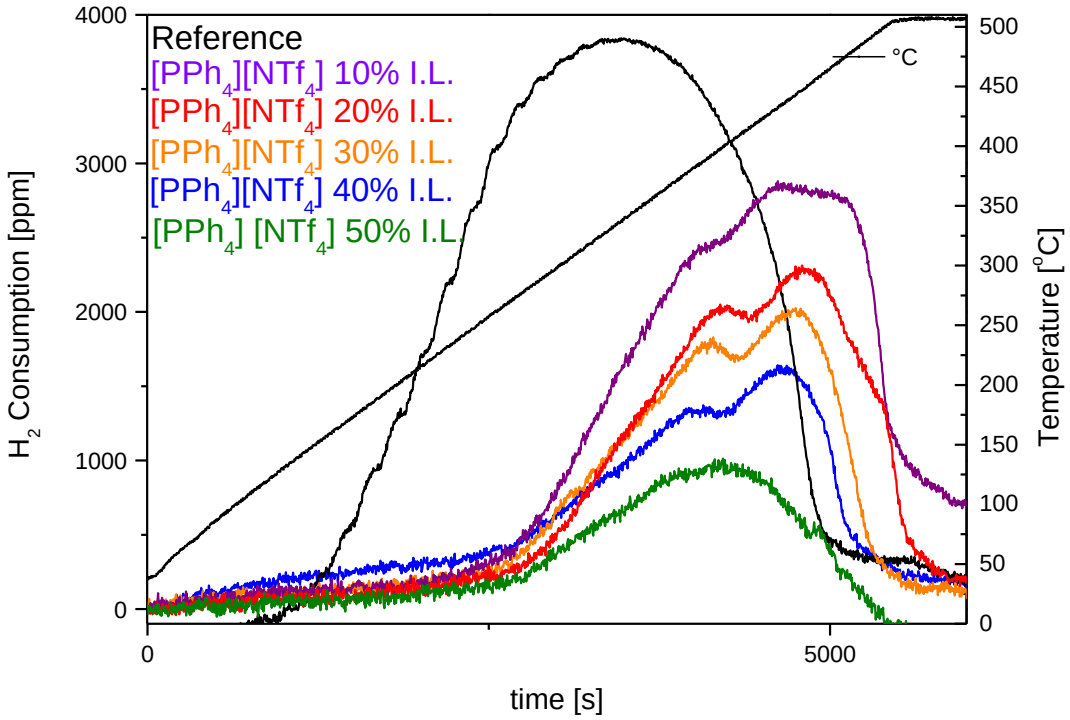

Figure 4 - TPR analysis of SCILL with different loadings of [PPh_4][NTf_2]

Due to the change in selectivity observed with the [PPh_4][NTf_2] based SCILL, we investigated the ionic liquid loading from 10-50 wt %. TPR analysis (fig 4) indicates that as the ionic liquid loading increases the catalyst becomes more difficult to reduce.

TPR analysis of the TMC catalysts indicates that the catalysts are not very active due to their poor reduction ability. The Cu Zn TMC has been carbonized at both 800 °C and 600 °C and the 800 °C sample is slightly more active than the 600 °C sample.

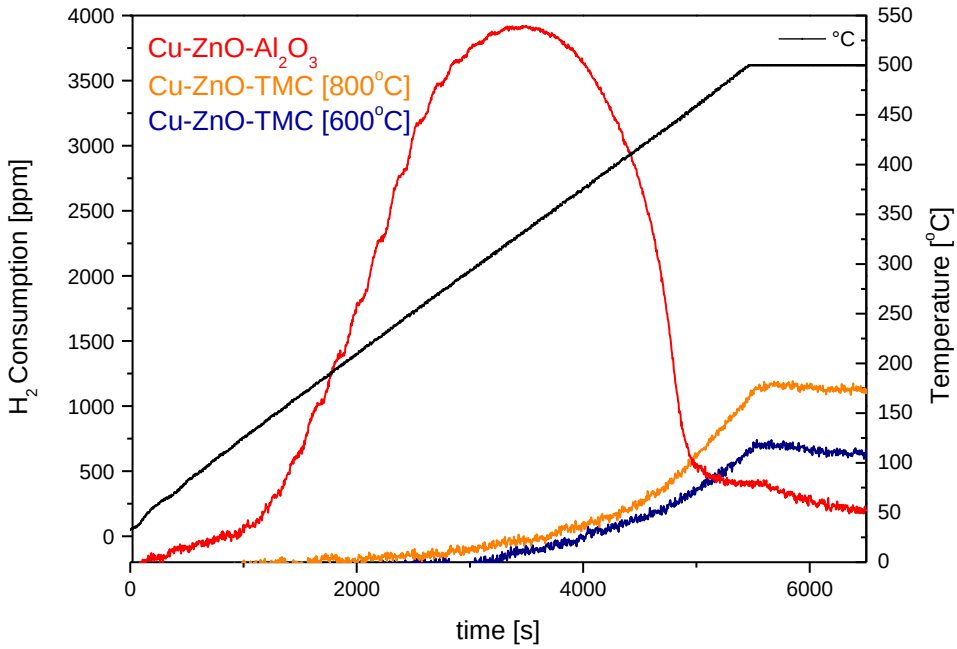

Figure 5 - TPR analysis TMC catalysts

XRD

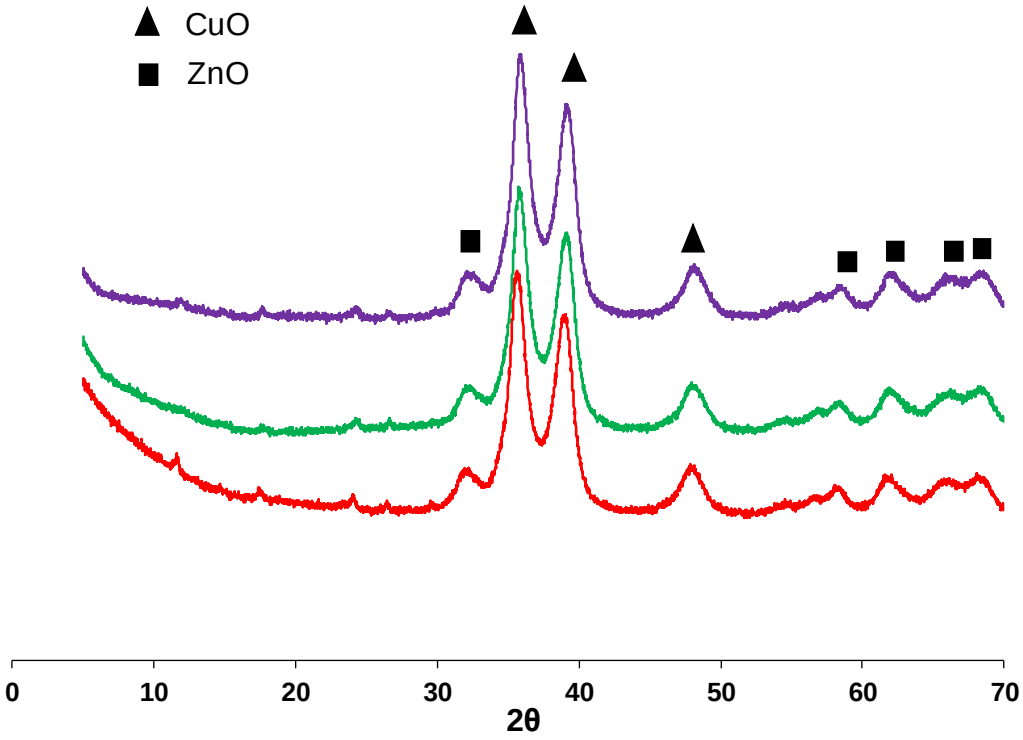

Figure 6 - XRD patterns for SCILL's with lower thermally stable ionic liquids. – $CnZnO/Al_2O_3$, -- [BMIM][OAc] SCILL, -- [HMIM][FAP] SCILL.

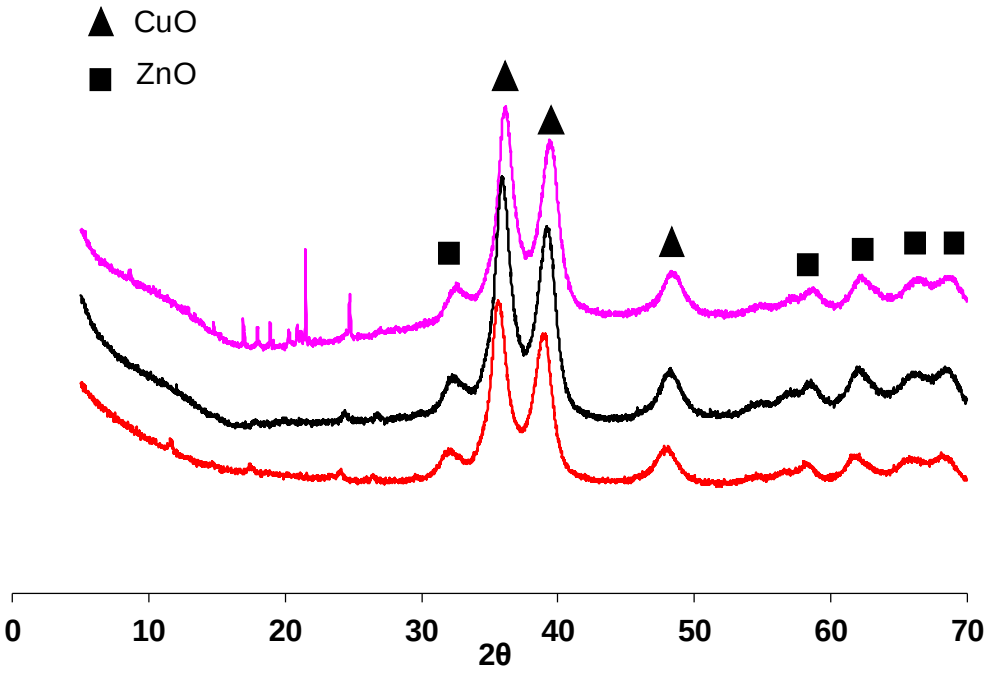

Figure 7 - XRD patterns for SCILL's with ionic liquids with high thermal stability. – $CnZnO/Al_2O_3$, --[PPh_4][Bu^FSO_3] SCILL, -- [PPh_4][NTf_2]] SCILL.

XRD data for the catalysts can be seen in figures 6-9. The XRD patterns of the SCILL's prepared with [BMIM][OAc] and [HMIM][FAP] are very similar to the commercial CuZn catalysts. There appears to be no structural change with the presence of these ionic liquids.

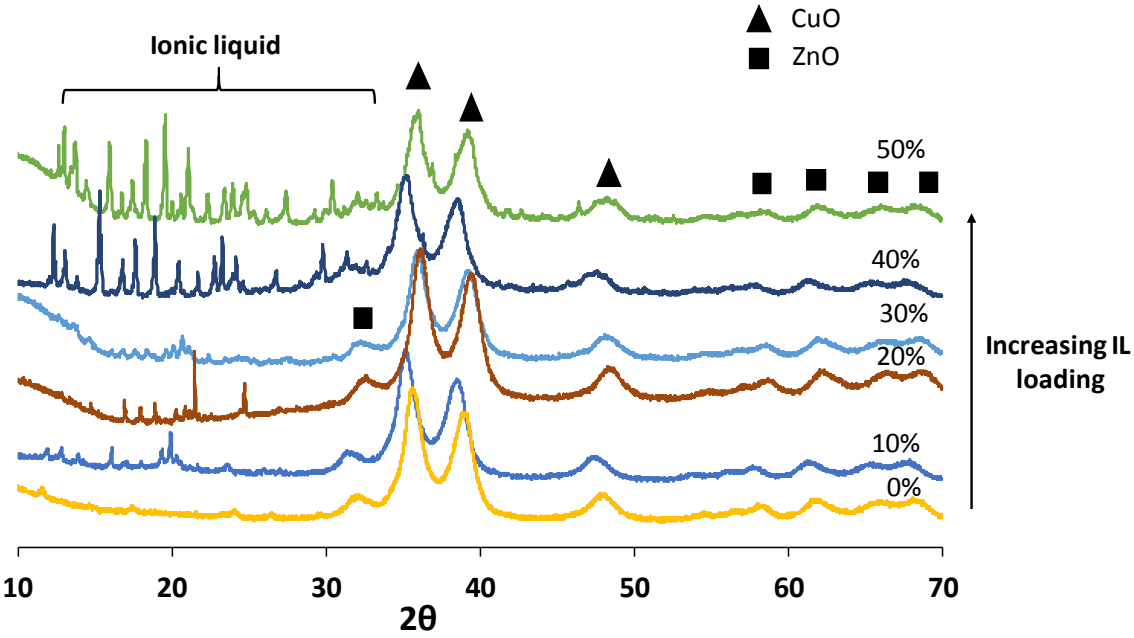

Figure 8 - XRD patterns for SCILL's with $[PPh_4][NTf_2]$ ionic liquid at increasing loadings (0-50 wt %)

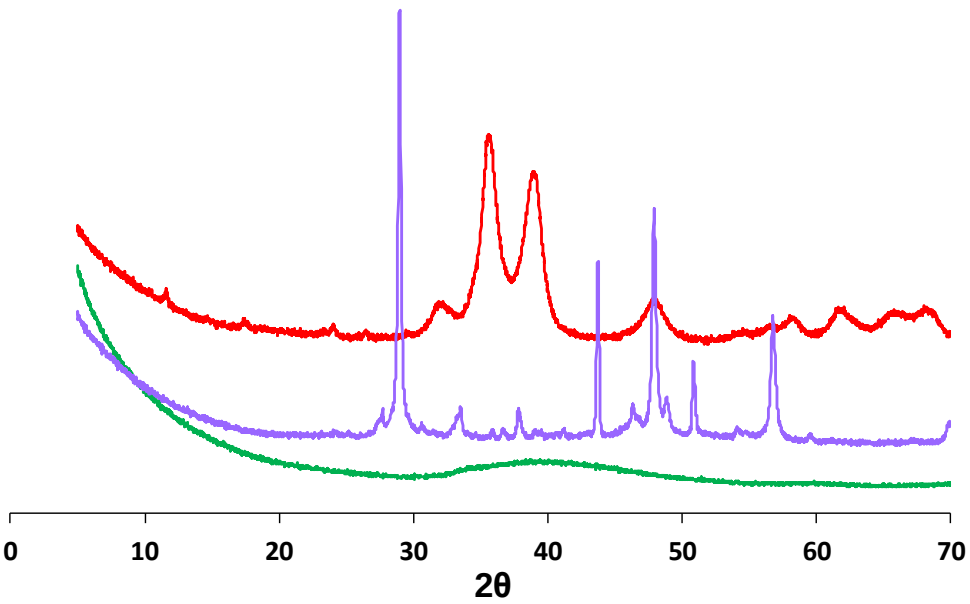

Figure 9 - XRD patterns for TMC catalysts. – Mo TMC, -- CuZn TMC, -- Commercial $CuZn/Al_2O_3$ catalyst

The XRD patterns for the SCILL's prepared with 10 wt % $[PPh_4][NTf_2]$ and $[PPh_4][Bu^FSO_3]$ ionic liquids can be seen in figure 7. There appears to be very little change in the XRD pattern of $[PPh_4][Bu^FSO_3]$ SCILL indicating no change in morphology or crystallinity of the catalyst. The XRD pattern of the SCILL prepared with $[PPh_4][NTf_2]$ appears noticeably different in the area of 10-15 °. As the loading of the ionic liquid is increased (figure 8) the 10 – 30 ° region noticeably changes. The peaks increase in number and intensity as the loading is increased.

XRD analysis for the TMC catalysts can be seen in figure 16. The XRD pattern for the Mo TMC was found to match the XRD pattern reported in the literature. The XRD pattern for Cu-Zn TMC is composed mainly of CuO, ZnO and carbon.

SEM and EDX

SEM and EDX analysis can be seen in figs 10-11 and Tables 2-3 for some of the catalysts. Fig 10 shows SEM images for the commercial catalysts and [BMIM][OAc] and [HMIM][FAP] SCILL's. SEM analysis shows no notable difference in appearance of the catalyst and the SCILL's. EDX analysis for the catalyst and [BMIM][OAc] based SCILL are very similar, however, the EDX analysis for [HMIM][FAP] SCILL is quite different. The percentage of copper in the [HMIM][FAP] SCILL is higher at 53.4% compared to 46-47% for the catalyst and [BMIM][OAc] SCILL. The percentage of oxygen is considerably reduced in the [HMIM][FAP] SCILL and the presence of P and F has been detected.

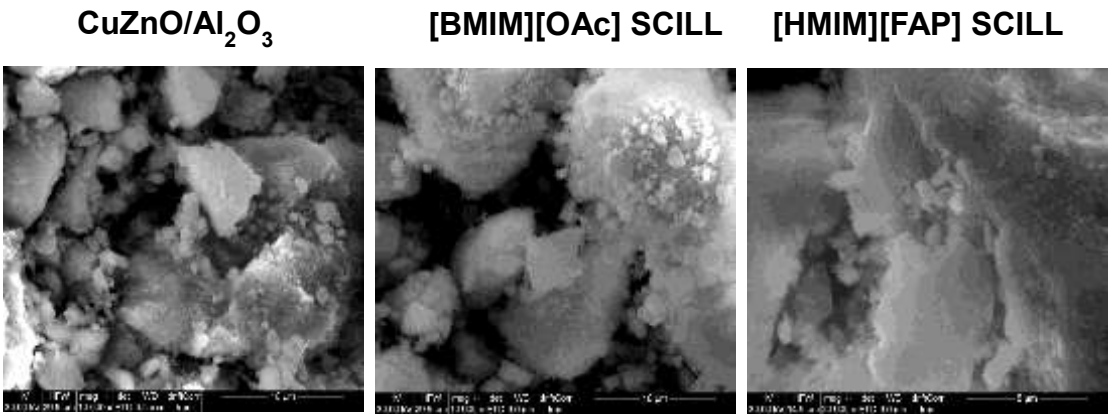

Figure 10 - SEM of SCILL's with lower thermal stability

Table 2
EDX data

	Composition %					
Catalyst	Cu	O	Zn	Al	F	P
[BMIM][OAc]	47	31	15	7	-	-
[HMIM][FAP]	53.4	21.1	16.1	5	4	0.4
Cu−ZnO−Al_2O_3	46	32	15	7	-	-

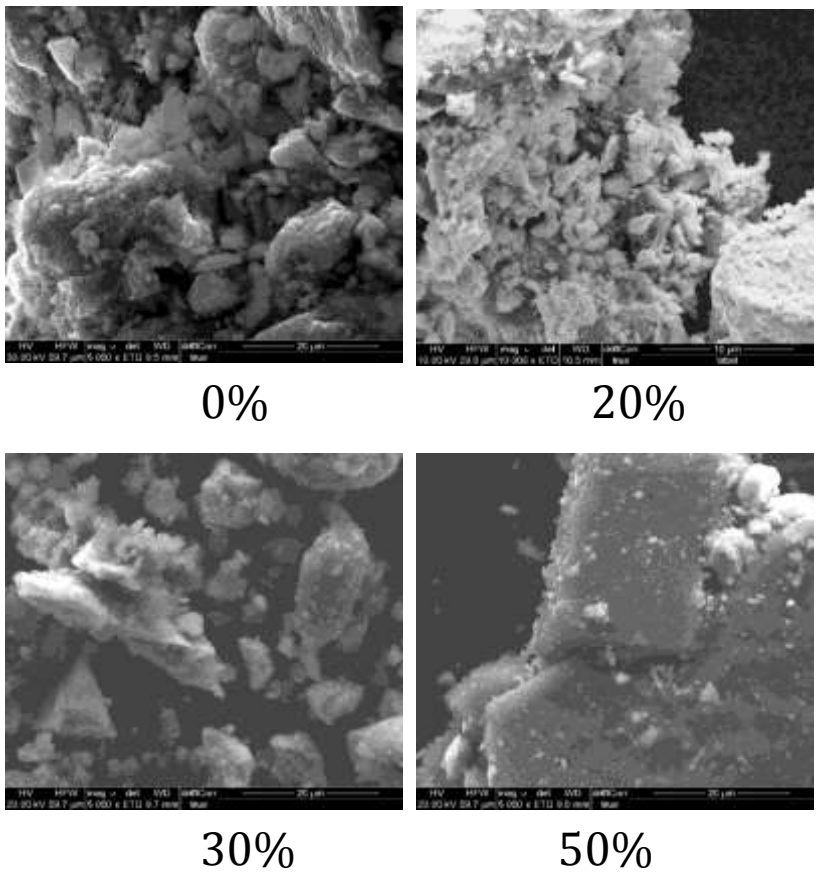

Figure 11 - SEM of SCILL's with increasing ionic liquid loading of [PPh_4][NTf_2]

Table 3 - **EDX data**

	Composition %						
Catalyst	Cu	O	Zn	Al	F	P	S
$[PPh_4][NTf_2]$ 30%	40	25.6	13.06	5.8	8.9	2.8	17.4
$[PPh_4][NTf_2]$ 50%	17.3	26.6	6.4	2.15	26.9	7.7	13.3
$Cu–ZnO–Al_2O_3$	46	32	15	7	-	-	-

SEM and EDX analysis for $[PPh_4][NTf_2]$ SCILL's can be seen in figure 11 and table 3. The quality of these images are quite poor due to the type of the material we are analysing. It can be seen that at lower loadings of ionic liquid (20 wt%) there is not much difference between the images of the 20 wt% and the commercial catalyst with no IL loading. However, as the ionic liquid loading is increased, the particles of catalyst appear larger and solid.

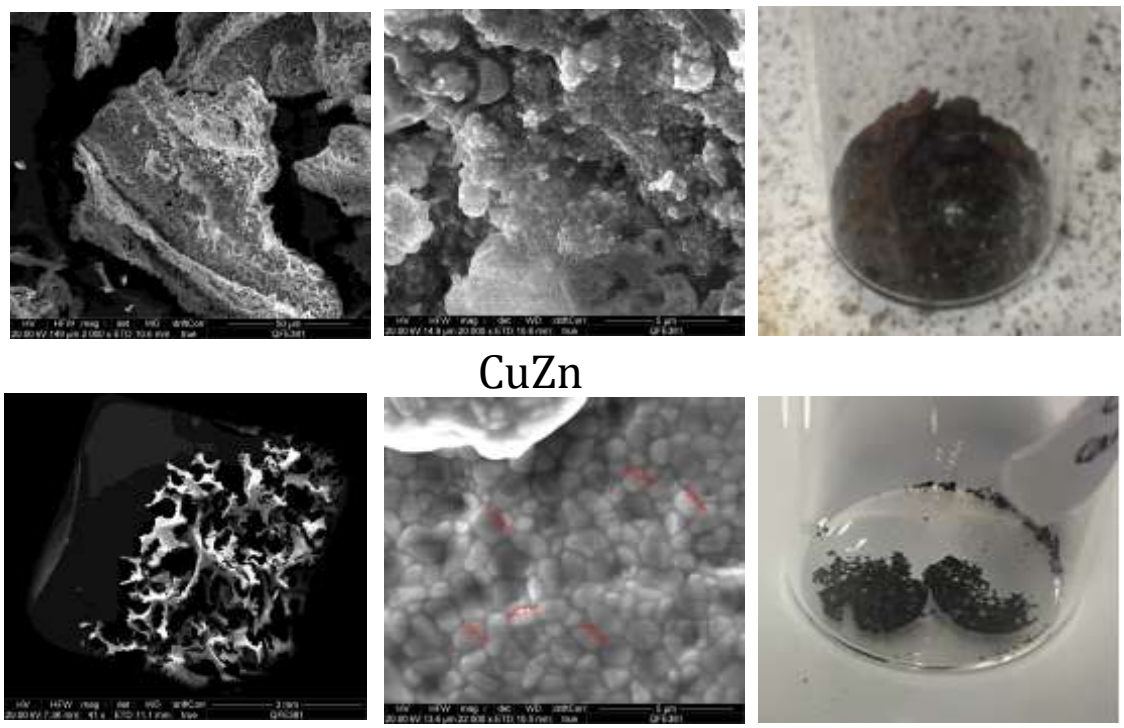

Figure 12 - SEM images for TMC

EDX analysis shows as the ionic liquid loading increases the amount of copper and zinc decreases as expected. However, in the case of the SCILL with 50 % IL loading the decrease is slightly more than it should be, and the amount of fluorine is greater than expected. SEM images for the TMC catalysts. The TMC's catalysts appear porous in nature and EDX analysis revealed a high concentration of carbon present in both samples.

Table 4 - **EDX data**

	Composition %								
Catalyst	C	Cu	O	Zn	Al	N	P	S	Mo
Cu TMC	44.6	14.7	2.3	29.1	-	0.6	-	8.7	-
Mo TMC	38.4	-	6.3	-	-	3.9	0.9	16.2	34.3
Cu−ZnO−Al_2O_3	-	46	32	15	7	-	-	-	-

Catalytic testing

A number of catalysts have been tested under industrially relevant conditons (high temperature and pressure) and the results can be seen in Figures 13-15 and table 5. Figure 13 shows the selectivtiy results of the hydrogenation of CO_2 to methanol for the commerical (CAT C) catalyst and two SCILL catalysts prepared with IL with high thermal stability. After 5 h the commerical catalyst was found to be 88% selective to methanol and 12% to C_2-C_4 hydrocarbons. The CO_2 conversion was 19%. Another commercial catalyst with a magnesium promoter (CAT A) was tested under the same conditions and the selectivtiy towards methanol was found to be 91% and had a slightly lower conversion of 15% (results not shown). The catalyst that displayed the highest selectivtiy and conversion to methanol was the SCILL prepared with 10 wt% $[PPh_4][Bu^FSO_3]$. After 5 h the CO_2 conversion was 22% and the selectivity to methanol was 92%, with the balance made up of C_2-C_4 hydrocarbons. Interestingly the SCILL prepared with 10 wt % $[PPh_4][NTf_2]$ was only 54% selective to methanol and 46% selectvite to C_2-C_4 hydrocarbons. As the loading of this ioinc liquid (figure 14) was increased the selectvitiy to methanol became lower, for example at 20 wt % the selectivtiy to methnaol had decreased to 30% and the selectivtiy to C_2-C_4 increased to 70 %. Above 30 wt % up to the maximum loading of 50 wt % the selectivity to C_2-C_4 was 100 %. By varying the loading and type of the ionic liquid it is possible to tune the catalyst for the desired product, e.g. methanol or hydrocarbon. Unfortunately the conversions obtained using $[PPh_4][NTf_2]$ ionic liquid are considerably lower than when using $[PPh_4][Bu^FSO_3]$ hence the operational conditions would need optimization to increase the conversion.

The Mo-TMC was also tested under industrially relevaent conditions and displayed comparable selectivtiy and actvitiy to the $[PPh_4][NTf_2]$ SCILL. Again, the operational conditions would require further optimization to improve the selectivity.

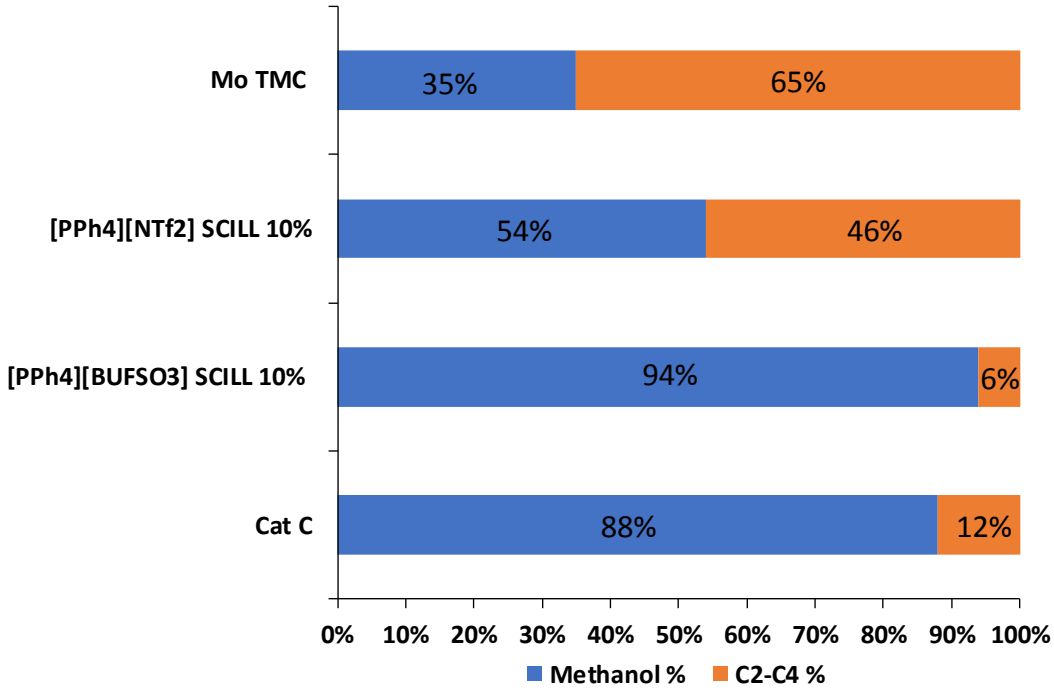

Figure 13 - Selectivity data for commercial catalyst (Cat C), SCILL's with 10 wt % $[PPh_4][NTf_2]$ and $[PPh_4][BU^FSO_3]$ ionic liquids and Mo-TMC.

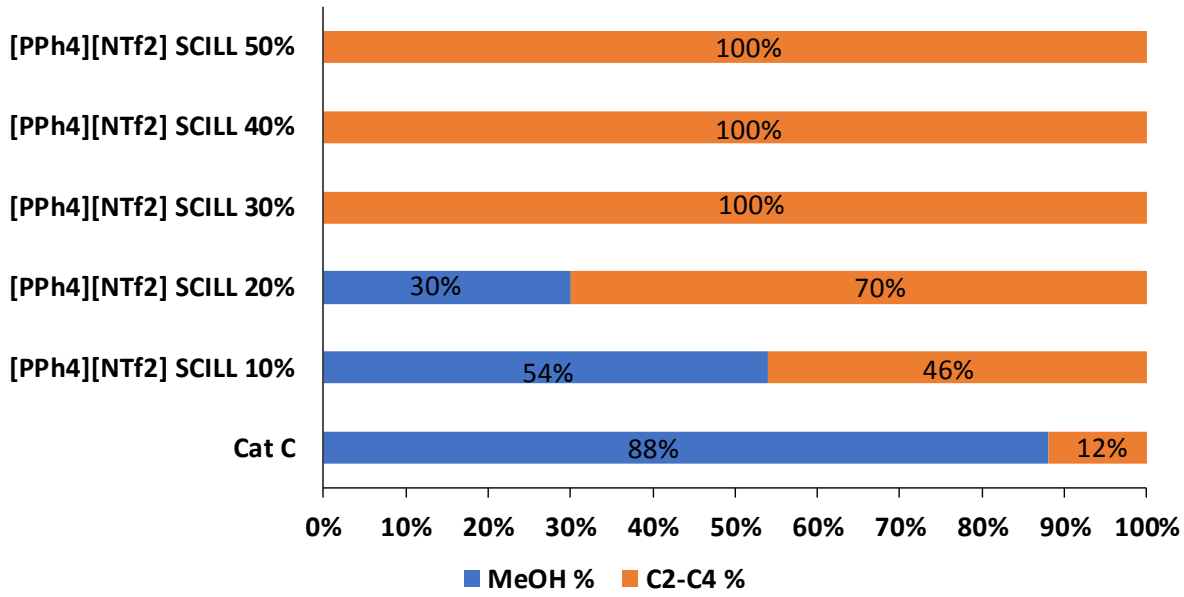

Figure 14 - Selectivity data for commercial catalyst (Cat C) and $[PPh_4][NTf_2]$ SCILL catalysts with increasing ionic liquid loading.

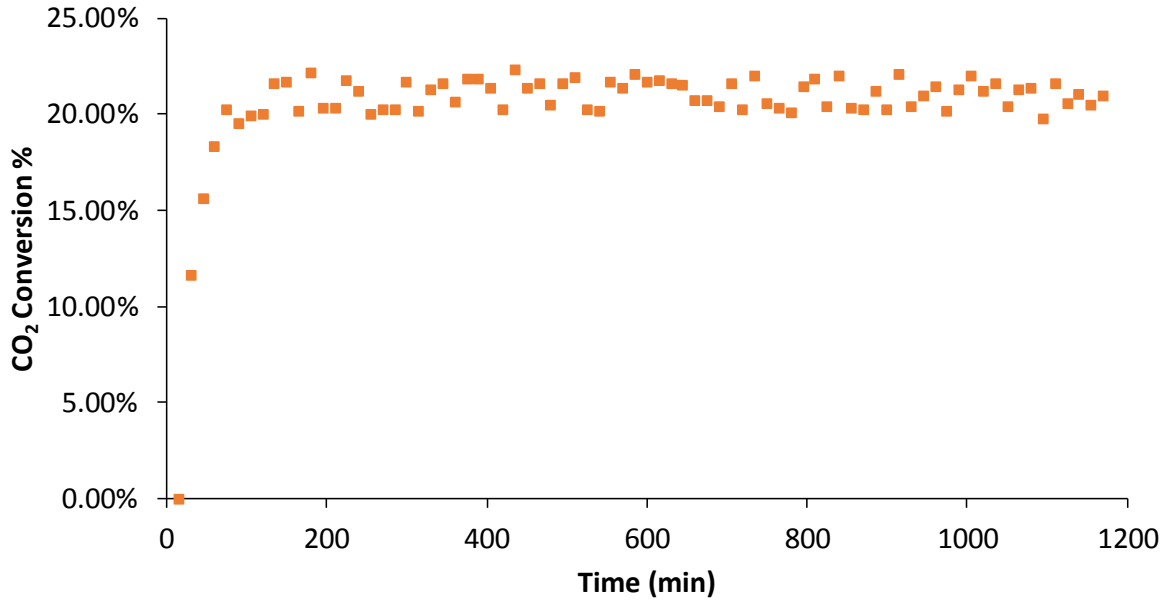

Figure 15 - CO_2 conversion using $[PPh_4][BU^FSO_3]$ SCILL

Table 5 - Conversion

Catalyst	CO_2 conversion
Cat A	15%
Cat C	19%
$[PPh_4][BU^FSO_3]$ SCILL 10%	22%
$[PPh_4][NTf_2]$ SCILL 10%	3%
$[PPh_4][NTf_2]$ SCILL 20%	5%
$[PPh_4][NTf_2]$ SCILL 30%	5%
$[PPh_4][NTf_2]$ SCILL 40%	3%
$[PPh_4][NTf_2]$ SCILL 50%	6%
Mo TMC	4%

Conclusions and future work

10 wt% $[PPh_4][BU^FSO_3]$ SCILL catalyst was found to have the highest conversion (22%) and best selectivity towards the methanol product (94 %). With $[PPh_4][NTf_2]$ SCILL a change in selectivity towards C_2-C_4 hydrocarbons was observed at higher loadings.

In the near future we plan to investigate ionic liquid loading with the $[PPh_4][BU^FSO_3]$ SCILL to see if the selectivity to methanol and the conversion can be further enhanced. The Cu-Zn TMC will also be tested at high temperature and pressure. Once the optimum loading of $[PPh_4][BU^FSO_3]$ ionic liquid has been determined this catalyst will be used to investigate the optimization of the operational conditions in the full CASE application.

QUILL Quarterly Report

February – April 2019

Name:	**Zara Shiels**		
Supervisor(s):	Dr Artioli, Prof Nockemann and Dr Harrison		
Position:	PhD		
Start date:	Feb 2019	Anticipated end date:	2022
Funding body:	Interreg (Renewable Engine Project)		

Developing New Nanocatalysts for the Direct Conversion of Biogenic Carbon Dioxide (CO_2) to Sustainable Fuels

Background

Rising CO_2 emissions, global warming, ocean acidification and a reliance on a diminishing source of fossil fuels are all factors having a detrimental effect on the environment, making our current way of living unsustainable.[1] In recent years, there has been a large emphasis on research that addresses these issues. Global warming is a serious problem and therefore, many governmental protocols and objectives have been put in place to tackle the issue, for example the Kyoto protocol in 1997, the Paris protocol[2] published in 2015 and the Clean Power Plan (CPP)[3] announced by President Obama in 2015. More recently a proposal has been signed to repeal the CPP in 2017, therefore now, more than ever, there needs to be action.[4] One solution that has been proposed as a means of relinquishing our need for fossil fuels, is to use waste CO_2 from processes (such as anaerobic digestion) and convert this to fuels.

Typically, for gas conversion reactions to occur efficiently, a catalyst is required and in the case of CO_2 conversion to hydrocarbon fuels, iron oxide nanoparticles have exhibited high activities. Furthermore, in a drive to reduce the use of toxic solvents in chemical processes, ionic liquids can be used in the preparation of this catalyst, whilst controlling the size of the nanoparticles without the need for additional capping agents and allows for dispersion which can prevent agglomeration of the particles. Several authors have reported that by employing this synthetic method, a multi-action catalyst was obtained, with three different sites for conversion of CO_2 to hydrocarbons in the C_5-C_{11} range.[5,6,7]

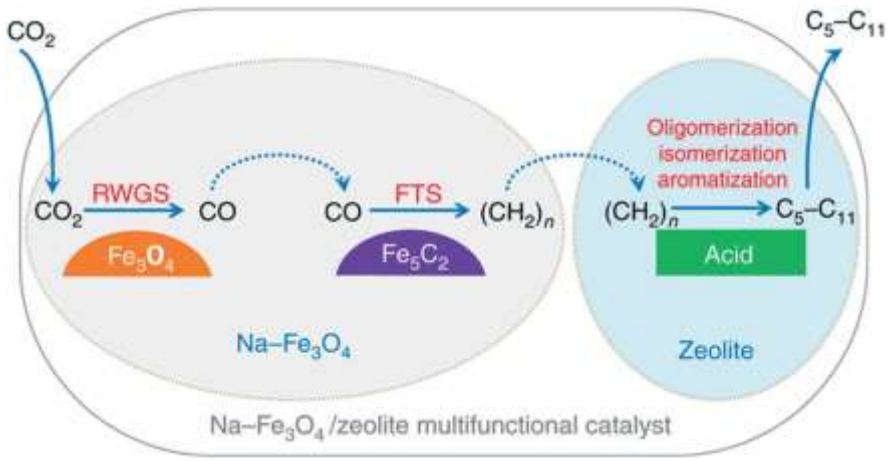

Figure 1 - Depiction of the mulfunctional catalyst required for conversion of CO2 to hydrocarbons

This report proposes two different possible catalyst synthesis routes that utilise these necessary ionic liquids. The first synthesis method involves the thermal decomposition of an iron precursor in a high temperature solution phase reaction. Once the reaction is complete, the produced iron (III) oxide can be separated through decantation and washed with hexane. Once fully separated, the iron (III) oxide will then be embedded within a zeolite structure for pH control and as a solid support for the final catalyst

The second novel method involves use of two iron precursors, already in the desired oxidation states, heated while stirring in the presence of a specifically chosen ionic liquid and requires less energy than previously reported syntheses. Through varying the ionic liquid utilised as the reaction solvent it is hoped we can achieve the capping capabilities of the previous reaction without the need for additional reagents.

Characterisation will be carried out at each stage of the process by a variety of methods: Nuclear Magnetic Resonance (NMR) Spectroscopy, Powder X-Ray Diffraction (PXRD), Temperature Programme Reduction (TPR), Scanning Electron Microscopy (SEM), Transmission Electron Microscopy (TEM), Brunauer-Emmett-Teller (BET) Surface Area analysis and so on.

Objective of this work

The overall aim of this project is to develop a reproducible method of synthesising a nanocatalyst for conversion of CO_2 to sustainable fuels. The initial focus is to synthesise several ionic liquids as the reaction medium to produce iron oxide. This will involve synthesis from 1-methylimidazole and a variety of chloroalkanes to achieve different chain lengths on the IL cation. The next stage will be to perform ion exchange in order to get the required anion, *e.g.* bistriflimide, acetate, *etc.*, allowing for fine-tuning of the catalyst preparation conditions. Once this has been achieved the ILs can be used to synthesise iron oxide nanoparticles (<10 nm). This will be carried out via two different routes, one reported by Wang *et al.*, and a novel method developed within Queen's University Belfast. The new method can then be optimised to produce the catalyst with the best activity, particle size, *etc.* The final part of the catalyst preparation involves mixing the prepared nanoparticles with a zeolite support to provide the acid sites required for the conversion to hydrocarbons. Varying the aluminium to silica ratio allows control of the acidity of the system, which will also be explored. Mixing will typically be carried out by ball milling. The final catalyst will then be tested in a specially designed rig capable of assessing the activity of the catalyst in a modified Fischer-Tropsch method.

Progress to date

<u>Ionic Liquids:</u>

A range of imidazolium ionic liquids were successfully prepared, including 1-butyl-3-methyl imidazolium octanoate, which has not been previously reported in the literature and is not commercially available. ^{1}H NMR spectroscopy was carried out to confirm successful synthesis and where possible, the spectra were compared with those available in the literature, *i.e.* for the synthesis of BmimCl and [Bmim][NTf_2]. In both cases, ^{1}H NMR spectroscopic signals were observed

at the correct chemical shifts and integrated for the correct number of protons confirming synthesis of the ionic liquid (Figures 2 and 3).

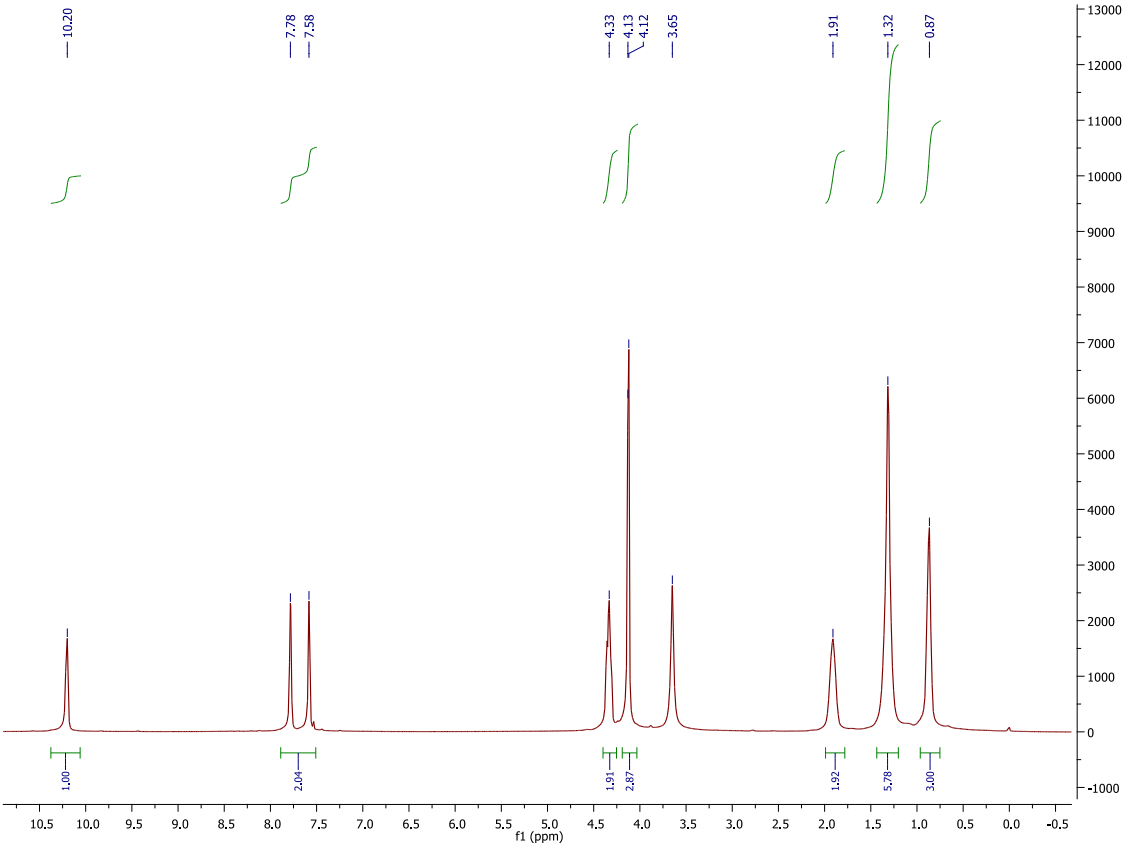

Figure 2 - ^{1}H NMR Spectrum of BmimCl

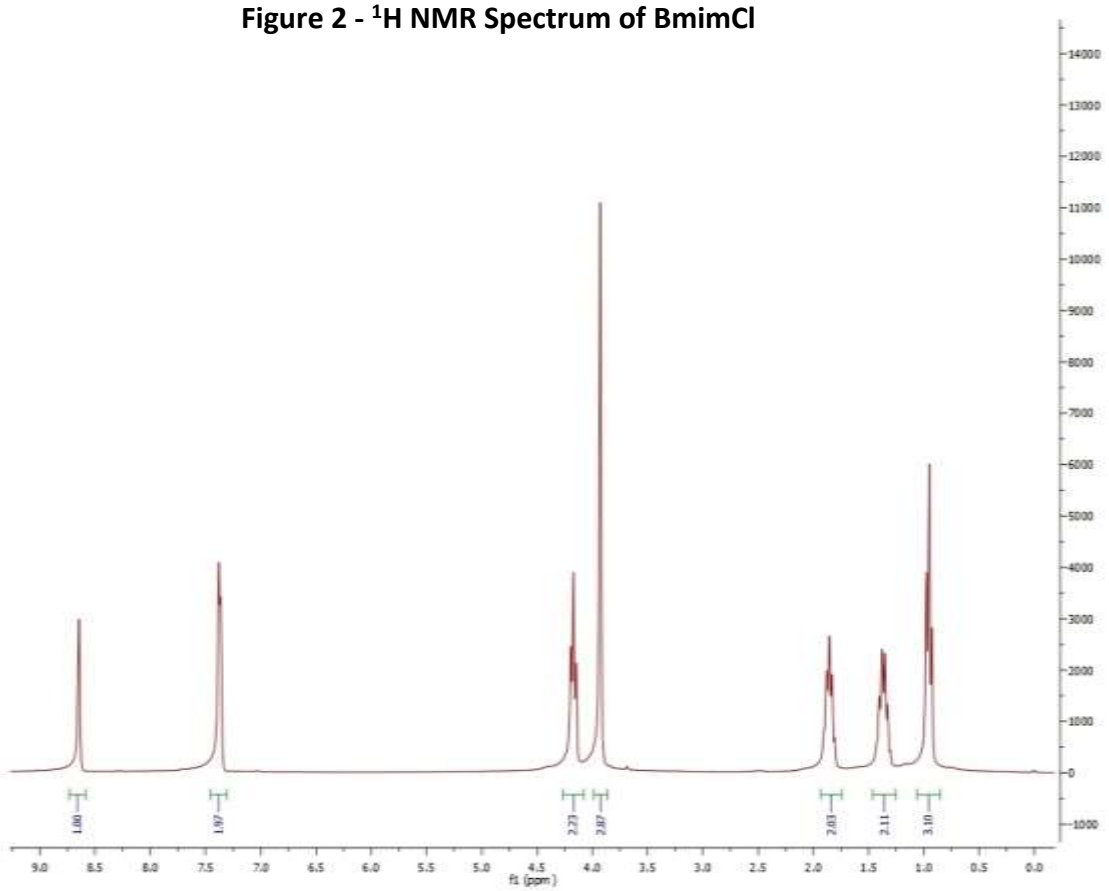

Figure 3 - NMR of 1-butyl-3-methylimidazolium

For the synthesis of [Bmim][Oct], which has not been previously reported, a pale yellow, viscous liquid was obtained with a yield of 113%. The fact that the yield is greater than 100% indicates that solvent may still be present. The appearance of this ionic liquid was noticeably different from the starting BmimCl and octanoic acid. The ionic liquid was soluble in $CDCl_3$ and this was employed to carry out ^1H NMR spectroscopy. Elemental analysis (CHNS), Differential Scanning Calorimetry (DSC) and Thermogravimetric analysis (TGA) are currently being carried out on this novel material.

The ^1H NMR spectrum (Figure 4) showed that the carboxylic acid proton (of octanoic acid) at 11.6 ppm was no longer present in the ^1H NMR spectrum of the newly synthesised [Bmim][Oct], suggesting that the anion exchange had successfully occurred. Furthermore, the imidazolium proton peaks were significantly shifted upfield from 10.20 to 9.45 ppm for the acidic proton of the imidazolium ring and the CH-CH are shifted upfield from 7.78 and 7.58 ppm to 7.60 and 7.45 ppm respectively. The alkyl protons of the butyl and methyl groups were also shifted upfield *ca.* 0.1 ppm. The proton resonances for the octanoic acid had the same chemical shift as that of the starting material.

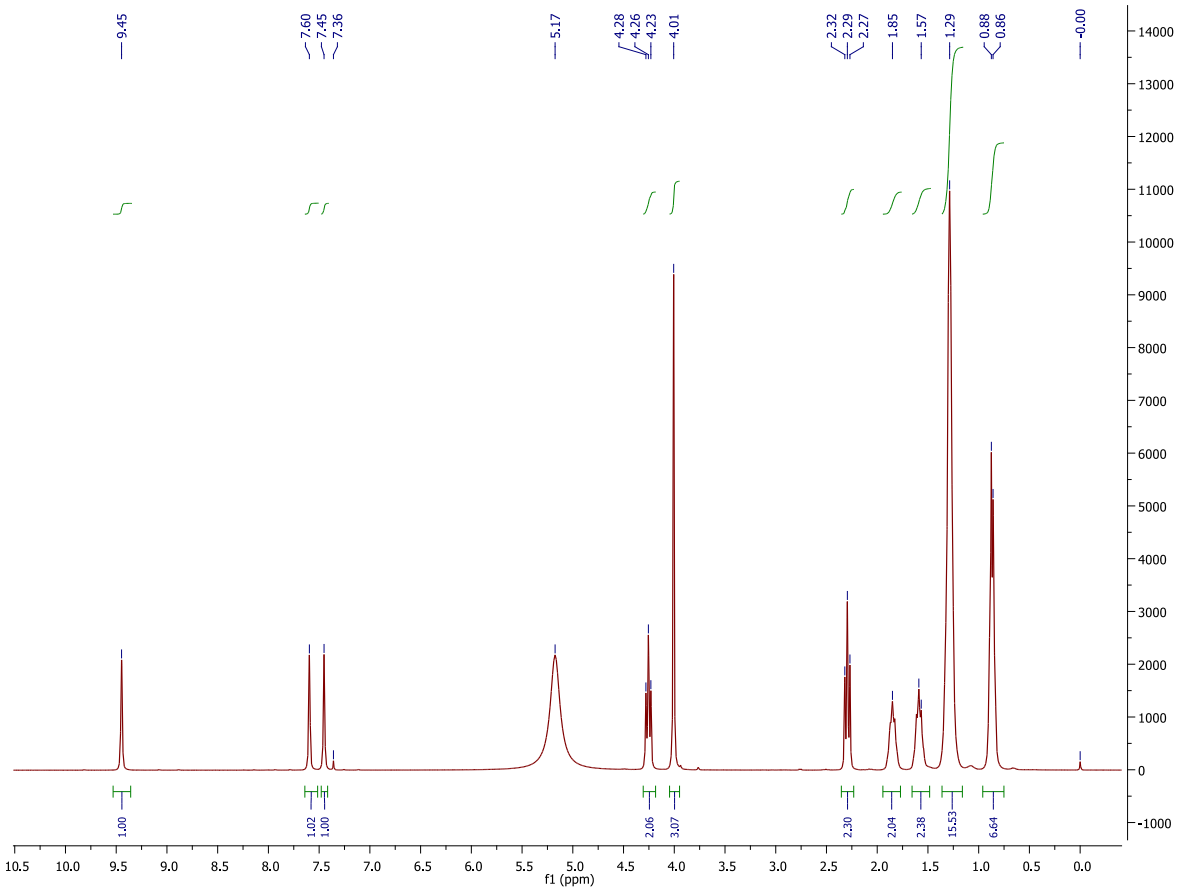

Figure 4 - PXRD Pattern showing material produced using Method 1 with additives

Iron Oxide Particles:

Using two different methods and various parameters, the synthesis of iron oxide nanoparticles was possible. One method previously reported in the literature by Wang *et al.* was attempted, in order to give a control material to compare the activity of the catalyst (prepared using novel methods) against. The second method which has not previously been reported in literature, starts from two iron chloride precursors, in the required oxidations states, employing an IL as the solvent.

Wang's literature method involved refluxing a mixture of iron pentacarbonyl, oleic acid and additives in [Bmim][NTf_2] at 280°C. A crystalline product was expected, however this was not obtained, as confirmed by PXRD (Figure 5 and 6). Amorphous Fe_2O_3 is a known intermediate when forming crystalline Fe_3O_4[16,17] and therefore it is possible that the reaction is being inhibited to some extent. One possible reason for this may be that the internal temperature of the reaction is not reaching the required 280°C, and therefore intermediates only are obtained. This is something that requires further investigation, however preliminary results involving calcination[17] at 420°C of the

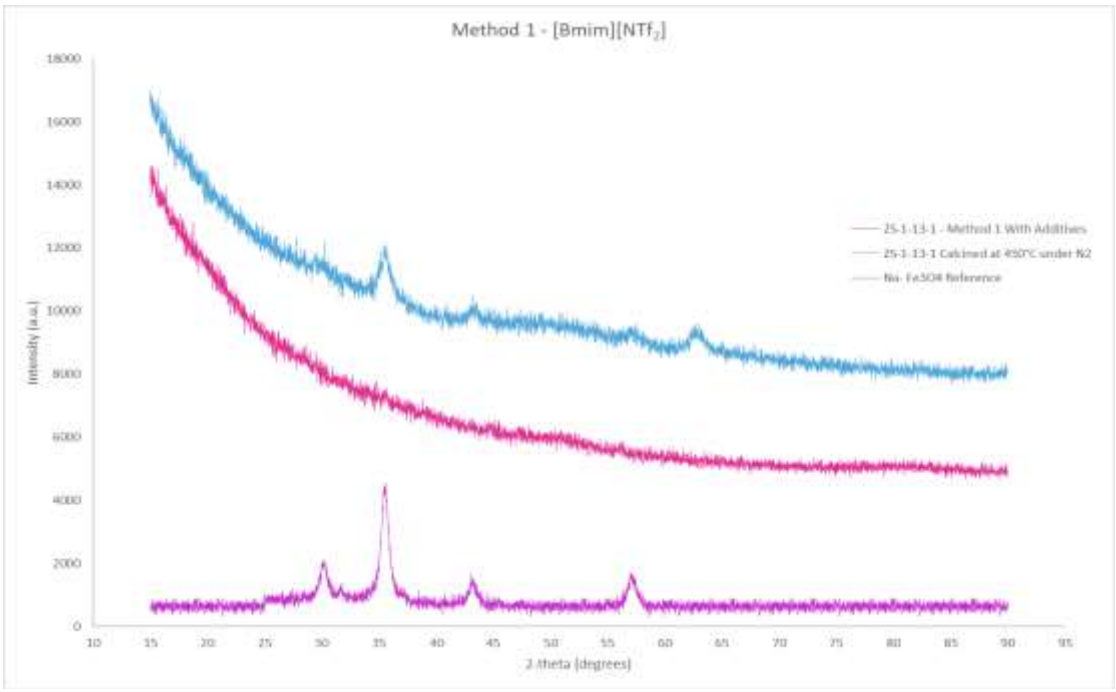

Figure 5 - PXRD Pattern showing material produced using Method 1 with Additives5

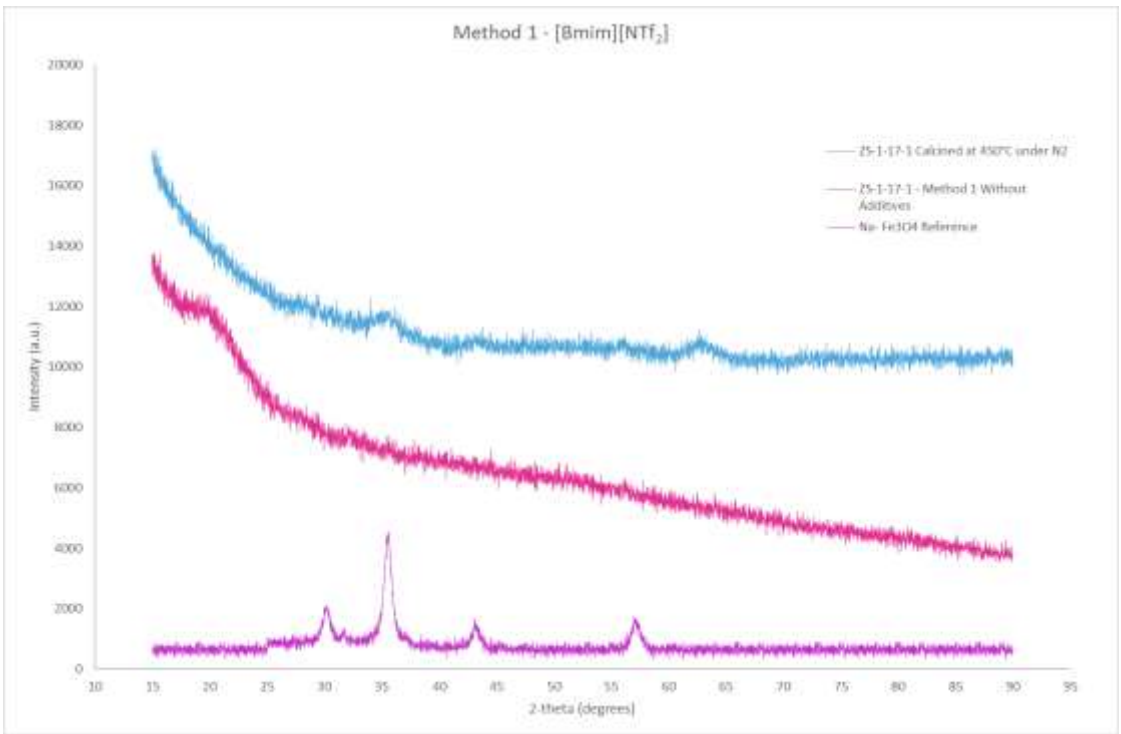

Figure 6 - PXRD Pattern showing material produced using Method 1 without Additives

material produced via Wang's method, has indicated crystallisation giving the desired Fe_3O_4 product.

The novel method, developed within Queen's University Belfast, involved reacting $FeCl_2$ and $FeCl_3$ in the presence of [Bmim][OAc] IL at 50°C. The reaction was carried out both with and without the addition of ammonia. The material produced when ammonia was added, was a black sticky solid with a yield of 61%. Isolation of this solid was quite difficult initially, however this has been optimised by the centrifuging with ethanol and distilled water, filtering and subsequent drying under vacuum pressure at 50°C, the solid was shown to be amorphous by PXRD (Figure 7). After calcination at 420°C under a flow of N_2, a black shiny solid is observed and XRD shows peaks corresponding to Fe_3O_4 (Figure 7). Other characterisation methods that are to be carried out on this material are Scanning Electron Microscopy (SEM), Energy Dispersive X-ray (EDX) mapping and Transmission Electron Microscopy (TEM).

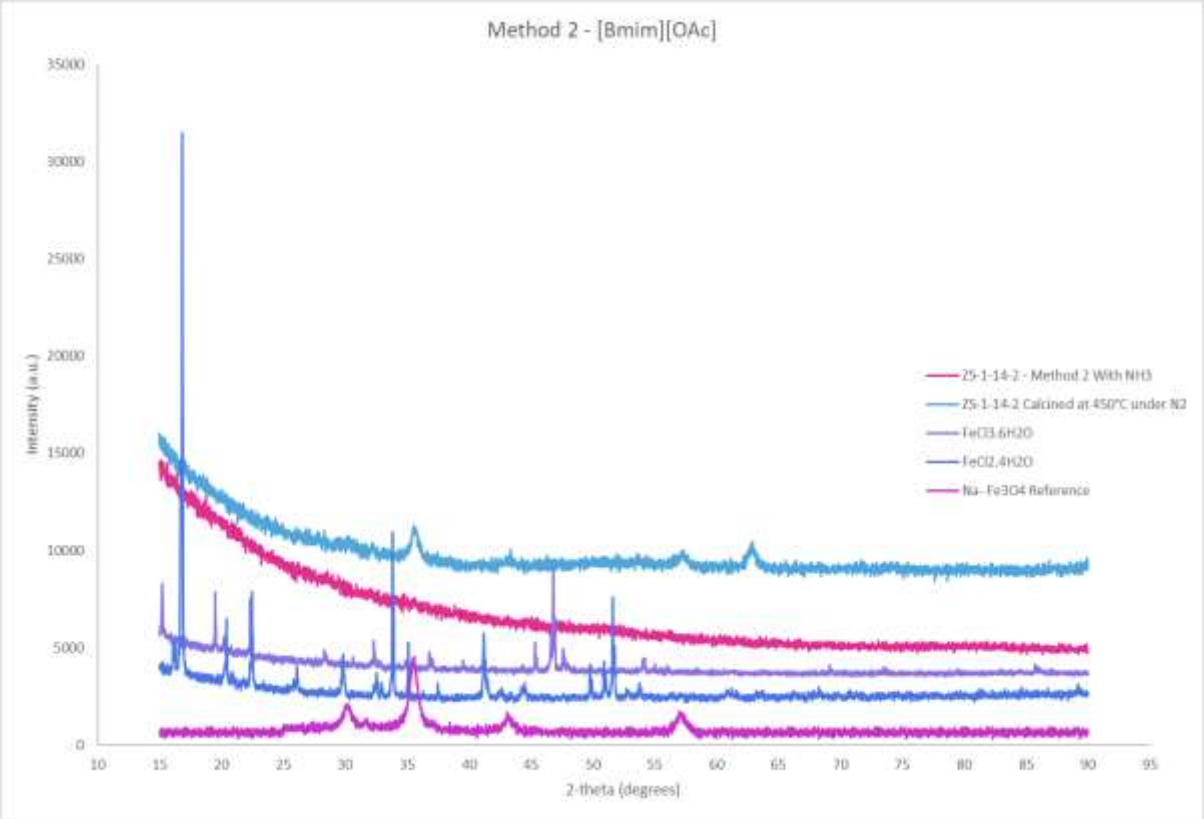

Figure 7 - PXRD Pattern showing material produced using Method 2 with NH_3

The novel method carried out without ammonia again produced a black sticky solid with a yield of 76%, after centrifugation, filtering and drying under vacuum pressure at 50°C. PXRD analysis of this material showed that it was amorphous (Figure 8). After calcination at 420°C under a flow of N_2, a black shiny solid was obtained and PXRD shows peaks corresponding to Fe_3O_4 (Figure 8). Other characterisation methods that are to be carried out on this material are SEM, EDX mapping and TEM.

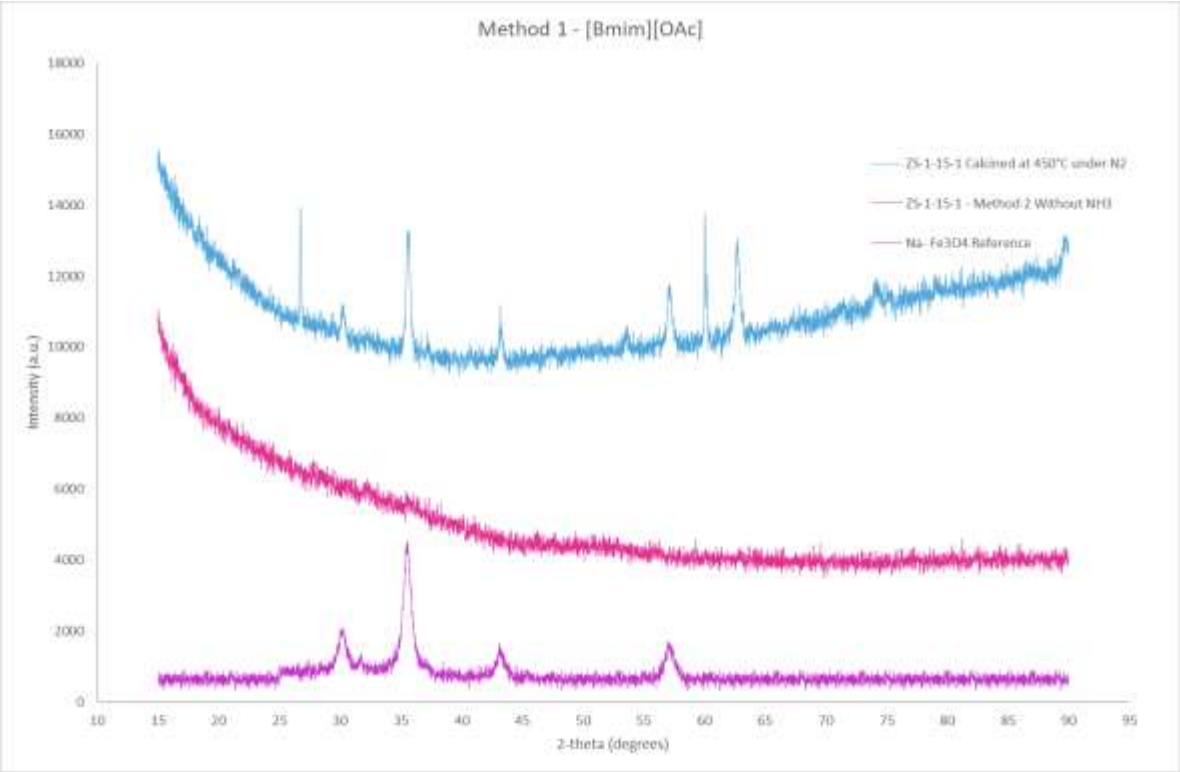

Figure 8 - PXRD Pattern showing material produced using Method 2 without NH_3

Conclusions and future work

In conclusion, it has been determined that crystalline Fe_3O_4 can be obtained using Wang *et al's* method. However, this is only possible after calcination, which was not reported and in addition, this method produced nanoparticles in a poor yield. The novel method developed herein at QUB, produced crystalline Fe_3O_4 using a much less energy intensive route, as the reaction proceeds at 50°C rather than 280°C (required for Wang's method). In addition, this novel method resulted in the preparation of Fe_3O_4 in yields > 60%, an excellent improvement on the methods reported. The iron precursors utilised in this procedure are also much less toxic and hazardous to the user than iron pentacarbonyl (employed in method one). Preparation of the novel ionic liquid, Bmim octanoate, was attempted in order to simplify the separation of the nanoparticles, however preliminary results indicate that this did not aid separation. Of course, a key factor in determining the feasibility of the newly synthesised nanoparticles will involve testing their catalytic activity within the modified Fischer-Tropsch system which will be a major focus in the next stage of the project.

Future work will include optimisation of the novel method of obtained iron oxide nanoparticles. These particles will then be granularly mixed with zeolites of varying silica ratios to vary the acidity of the final catalyst. This will be achieved through utilisation of ball milling apparatus. The final catalyst obtained will require characterisation by XRD, BET surface area, elemental analysis, XPS, SEM, EDX mapping and TEM. The next stage of the project will involve testing the activity of the final catalyst produced. In the first instance, this is conducted by Temperature Programmed Reduction (TPR) to evaluate the hydrogen conversion capability. Finally, the activity of the catalyst in producing hydrocarbons of chain length C_5-C_{11} will be shown by use of a reactor for hydrogenation of CO_2 which is connected to a Gas Chromatograph (GC) with a specific column for detection of olefins in this chain length range.

References

1. J. Wei, Q. Ge, R. Yao, Z. Wen, C. Fang, L. Guo, H. Xu and J. Sun, *Nature Communications*, 2017, **8**, 15174.
2. Ce. Croopmémenittee, 2.
3. The Clean Power Plan, https://www.edf.org/clean-power-plan-resources, (accessed 12 March 2019).
4. 2016, 290.
5. H. Yang, C. Zhang, P. Gao, H. Wang, X. Li, L. Zhong, W. Wei and Y. Sun, *Catal. Sci. Technol.*, 2017, **7**, 4580–4598.
6. I. Dimitriou, P. García-Gutiérrez, R. H. Elder, R. M. Cuéllar-Franca, A. Azapagic and R. W. K. Allen, *Energy & Environmental Science*, 2015, **8**, 1775–1789.
7. M. D. Porosoff, B. Yan and J. G. Chen, *Energy & Environmental Science*, 2016, **9**, 62–73.